



TECHNISCHE
UNIVERSITÄT
WIEN
Vienna University of Technology

DISSERTATION

MAGNETIC RESONANCE MICRO-IMAGING OF THE HUMAN SKIN IN VIVO USING MINIATURE RADIO FREQUENCY COILS

*ausgeführt zum Zwecke der Erlangung des akademischen Grades eines
Doktors der technischen Wissenschaften*

unter der Leitung von
Univ.-Prof. DI Dr. Gerald Badurek
E141, Atominstitut der Österreichischen Universitäten

und von
Univ.-Prof. DI Dr. Ewald Moser
Medizinische Universität Wien
Zentrum für Medizinische Physik und Biomedizinische Technik
Exzellenzzentrum Hochfeld-MR

Univ.-Prof. Dr. Luc Darrasse
Université Paris-Sud XI
IR4M – Imagerie par Résonance Magnétique Médicale et Multi-Modalités

eingereicht an der
Technischen Universität Wien
Fakultät für Physik

von
Dipl.-Ing. Elmar Laistler
Matrikelnummer 995769
Blindengasse 42/9
A-1080 Wien

Wien, am 15. Dezember 2010

ABSTRACT

Magnetic resonance imaging (MRI) has developed to one of the backbones of modern medical diagnostics since its first use in the 1970s. The large number of different image contrasts and the possibility to assess clinically relevant physiological parameters, especially for soft tissues, combined with the non-invasiveness and safety of the technique have been the basis for its great success.

Nevertheless, is a relatively insensitive method, since it can only detect signal from a small fraction of the spins available in the investigated tissues. The higher the spatial resolution of the experiment, the lower the number of spins that effectively contribute to the signal that is acquired. This is especially critical for MR micro-imaging with voxel volumes that are about 1000-fold smaller than for standard imaging techniques.

This intrinsic loss in signal can be partially recovered by operating at higher field strength, using more sensitive radio frequency detectors and optimized hardware and acquisition strategies.

In this work, a combination of all these aspects has been achieved, in order to depict the network of small blood vessels in the human skin of living subjects. The demonstrated techniques allow for acquisition of a volume covering all skin layers in an area of $\approx 2 \text{ cm}^2$ with isotropic voxel sizes of 80-100 μm in about 10 minutes.

Dedicated post-processing algorithms have been developed for higher specificity of vessel detection and visualization and for the extraction of descriptive quantitative parameters of the vessel tree.

The images and vessel parameters could serve as a basis for early diagnostics and classification of systemic inflammatory vascular diseases like vasculitis. Due to the non-invasiveness of the method, longitudinal studies in the course of treatment could be performed to monitor its success.

ZUSAMMENFASSUNG

Die Magnetresonanztomografie (MRT) hat sich seit ihren ersten Einsätzen in den 1970er Jahren zu einer der Säulen der medizinischen Diagnostik mit bildgebenden Verfahren entwickelt. Die große Anzahl von Bildkontrasten und die Möglichkeit, klinisch relevante physiologische Parameter, insbesondere in Weichteilen, zu erfassen, in Kombination mit der Nicht-Invasivität und Sicherheit der Methode, sind die Basis dieses großen Erfolgs.

Nichtsdestotrotz ist die MRT eine relative insensitive Technik, da nur ein kleiner Bruchteil der Spins, die im untersuchten Gewebe zur Verfügung stehen, tatsächlich zum gemessenen Signal beitragen. Dies ist insbesondere in der MR Mikroskopie mit Bildpunktvolumina, die um das 1000-fache kleiner sind als in der Standardbildgebung, ein kritischer Faktor.

Dieser intrinsische Verlust an Signalintensität kann zum Teil durch den Einsatz stärkerer Magnetfelder, durch die Konstruktion von empfindlicheren Hochfrequenz-Empfängerspulen und optimierter Hardware und Aufnahme-strategien kompensiert werden.

In dieser Arbeit wird eine Kombination all dieser Punkte erreicht, mit dem Ziel, das Netzwerk kleiner Blutgefäße in der Haut am lebenden Menschen darzustellen. Die gezeigten Techniken erlauben es, ein Volumen, das alle Hautschichten auf einer Fläche von ca. 2 cm² abdeckt, mit einer isotropen räumlichen Auflösung von 80-100 µm in etwa 10 Minuten abzudecken.

Speziell entwickelte Nachverarbeitungsalgorithmen erhöhen die Spezifität der Detektion von Blutgefäßen und berechnen beschreibende quantitative Parameter des Gefäßbaums.

Diese Bilder und Gefäßparameter könnten als Basis für die Frühdiagnostik und Klassifizierung von entzündlichen systemischen Erkrankungen der Blutgefäße, wie der Vaskulitis, dienen. Aufgrund der Nicht-Invasivität der Methode könnten longitudinale Studien während der Therapie durchgeführt werden, um den Behandlungserfolg zu beobachten.

TABLE OF CONTENTS

1	Introduction.....	1
1.1	Introduction	2
1.2	Thesis Outline	4
2	Theoretical Background.....	5
2.1	Magnetic Resonance	6
2.2	Signal and Noise in MR Experiments	10
2.2.1	Signal.....	10
2.2.1.1	Demonstration of the reciprocity principle	10
2.2.1.1.1	Magnetic field produced by moving charges in a coil ..	10
2.2.1.1.2	Electromotive force induced in the coil by the spins ..	11
2.2.1.2	The signal equation	13
2.2.2	Noise.....	14
2.2.2.1	Noise sources.....	15
2.2.2.1.1	Sample noise	15
2.2.2.1.2	Coil noise	16
2.2.2.2	Noise regimes	18
2.2.2.2.1	Copper coils.....	20
2.2.2.2.2	HTS coils.....	20
2.2.2.2.3	Comparison: HTS vs. copper coil	20
2.2.3	Signal to noise ratio and sensitivity.....	21
2.2.3.1	Scaling rules	22
2.2.3.2	Increasing measurement sensitivity.....	22
2.2.3.2.1	Magnetization enhancement	23
2.2.3.2.2	RF coil miniaturization.....	24
2.2.3.2.3	Cooling of RF coils.....	26
2.3	RF Surface Coil Technology for MR Microimaging.....	28
2.3.1	RF coil materials.....	28
2.3.1.1	Copper.....	28
2.3.1.2	Superconductors	29
2.3.1.2.1	Low temperature superconductors	29
2.3.1.2.2	High temperature superconductors	29
2.3.1.3	Cooling techniques.....	30

2.3.1.3.1	Direct immersion in liquid cryogenic bathes.....	30
2.3.1.3.2	Cold ends.....	30
2.3.1.3.3	Closed-cycle cooling.....	31
2.3.2	Geometry.....	32
2.3.2.1	“Classical” surface coils.....	32
2.3.2.2	Auto-resonant structures.....	33
2.3.2.2.1	Localized elements.....	33
2.3.2.2.2	Distributed elements.....	35
2.3.3	Connection to the receiver.....	37
2.3.3.1	Capacitive coupling.....	37
2.3.3.2	Inductive coupling.....	37
2.4	Skin Imaging.....	38
2.4.1	Anatomy and function of the skin.....	38
2.4.1.1	Epidermis.....	38
2.4.1.2	Dermis.....	38
2.4.1.3	Hypodermis/Subcutis.....	38
2.4.1.4	Skin vasculature.....	39
2.4.2	MR skin imaging.....	40
2.4.3	Other imaging modalities.....	42
2.4.3.1	Biopsy with subsequent histology.....	42
2.4.3.2	Photography.....	42
2.4.3.3	Surface microscopy.....	42
2.4.3.4	Ultrasound.....	43
2.4.3.5	Optical coherence tomography.....	43
2.4.3.6	Confocal reflectance microscopy.....	43
2.4.3.7	Laser Doppler perfusion.....	43
2.5	Cutaneous Vasculitis.....	44
2.5.1	Introduction.....	44
2.5.2	Classification schemes.....	44
2.5.3	Description of different vasculitides.....	46
2.5.4	Need for new diagnostic modalities.....	48
3	Experimental Studies.....	51
3.1	Study I: 12 mm HTS Surface Coil at 1.5 Tesla.....	52
3.1.1	Purpose.....	52
3.1.2	Materials and Methods.....	52
3.1.2.1	MR scanner.....	52

3.1.2.2	Network analyzers.....	52
3.1.2.3	RF coils.....	54
3.1.2.3.1	Coil design	54
3.1.2.3.2	Mask creation	55
3.1.2.3.3	Coil production	55
3.1.2.3.4	Coil characterization	56
3.1.2.4	Experimental setup	60
3.1.2.5	Evaluation of loss contributions	64
3.1.2.6	MR sequences.....	64
3.1.3	Results	68
3.1.3.1	RF coils.....	68
3.1.3.1.1	Design.....	68
3.1.3.1.2	Quality factor	68
3.1.3.2	Images.....	69
3.1.3.3	Vessels.....	72
3.1.3.4	SNR.....	74
3.1.3.5	Loss contributions	76
3.1.3.5.1	Losses in the HTS material.....	76
3.1.3.5.2	Losses due to the tuning copper ring	77
3.2	Study II: 15 mm Surface Coil at 3 Tesla	78
3.2.1	Purpose	78
3.2.2	Materials and Methods.....	78
3.2.2.1	MR scanner.....	78
3.2.2.2	Network analyzer.....	79
3.2.2.3	RF coil.....	79
3.2.2.3.1	Coil characterization	79
3.2.2.4	Resolution phantom.....	81
3.2.2.4.1	Modulation transfer function	81
3.2.2.5	Subjects.....	82
3.2.2.6	MR sequences	83
3.2.2.7	Post-processing.....	84
3.2.3	Results	85
3.2.3.1	RF coil properties.....	85
3.2.3.2	Resolution phantom.....	85
3.2.3.3	Anatomical features	87
3.2.3.3.1	Skin layers and dermal structures.....	87
3.2.3.3.2	Vessels.....	91
3.2.3.4	Image quality	94
3.2.3.4.1	Realignment.....	94
3.2.3.4.2	SNR and CNR.....	94

3.3	Study III: 6 mm Surface Coil at 7 Tesla	96
3.3.1	Purpose	96
3.3.2	Materials and Methods.....	96
3.3.2.1	MR scanner	96
3.3.2.2	Network analyzer	97
3.3.2.3	RF coil.....	97
3.3.2.4	Measurement setup	98
3.3.2.4.1	Inductive coupling to the receiver chain	98
3.3.2.4.2	Fine tuning of the RF coil.....	99
3.3.2.5	Sequence	99
3.3.2.6	Subjects.....	101
3.3.3	Results	101
3.3.3.1	RF coil.....	101
3.3.3.2	Images	101
4	Image Processing.....	103
4.1	Image Enhancement	104
4.1.1	Zero-filling.....	104
4.1.2	Averaging after realignment	104
4.1.3	Chemical shift filter	106
4.2	Vessel Segmentation.....	112
4.2.1	Manual segmentation	112
4.2.2	Calculation of vessel diameter.....	112
4.3	Extraction of Quantitative Vessel Parameters	113
4.3.1	Graph theory.....	113
4.3.2	Skeletonization	115
4.3.2.1	Preservation of connectivity	115
4.3.2.2	Preservation of topology	116
4.3.3	Graph from skeleton	119
4.3.3.1	Node classification schemes.....	119
4.3.3.2	Graph reduction.....	123
4.4	Software.....	124
4.4.1	MATLAB	124
4.4.2	MeVisLab.....	124
4.4.3	ITK/VTK.....	124
4.4.4	MRicro	124

5 Discussion and Conclusions	125
5.1 Discussion	126
5.1.1 Study I: 12 mm HTS surface coil at 1.5 T	126
5.1.2 Study II: 15 mm surface coil at 3 T.....	126
5.1.3 Study III: 6 mm surface coil at 7 T.....	127
5.1.4 Image processing	128
5.2 Conclusions and Perspectives.....	129
6 Annexes	I
6.1 Semi-Analytical Model for Simulation of MTLRs.....	II
6.2 MATLAB Toolbox for Calculation of MTLR Geometries	IV
6.2.1 Frequency calculation	IV
6.2.1.1 Calc_freq.m	IV
6.2.1.1.1 Purpose.....	IV
6.2.1.1.2 Usage	IV
6.2.1.1.3 Input parameters	IV
6.2.1.1.4 Result.....	V
6.2.1.1.5 Examples	V
6.2.1.2 Calc_freq_esp_w.m.....	V
6.2.1.2.1 Purpose.....	V
6.2.1.2.2 Usage	V
6.2.1.2.3 Input parameters	V
6.2.1.2.4 Result.....	VI
6.2.1.2.5 Examples	VI
6.2.1.3 Calc_freq_all.m.....	VI
6.2.1.3.1 Purpose.....	VI
6.2.1.3.2 Usage	VI
6.2.1.3.3 Input parameters	VI
6.2.1.3.4 Result.....	VI
6.2.2 Data collection	VII
6.2.2.1 Collect_all_data.m	VII
6.2.2.1.1 Purpose.....	VII
6.2.2.1.2 Usage	VII
6.2.2.1.3 Input parameters	VII
6.2.2.1.4 Result.....	VII
6.2.3 Data analysis.....	VIII
6.2.3.1 Search_freq.m	VIII

6.2.3.1.1	Purpose.....	VIII
6.2.3.1.2	Usage	VIII
6.2.3.1.3	Input parameters.....	VIII
6.2.3.1.4	Result.....	IX
6.2.3.1.5	Examples	IX
6.2.3.2	F_esp_w.m.....	X
6.2.3.2.1	Purpose.....	X
6.2.3.2.2	Usage	X
6.2.3.2.3	Input parameters.....	X
6.2.3.2.4	Result.....	X
6.2.3.2.5	Examples	XI
7	Bibliography	XIII
8	List of Figures	XXIX
9	List of Tables	XXXIII
10	Publications and Presentations	XXXV

1 INTRODUCTION

1.1 INTRODUCTION

Magnetic resonance imaging (MRI) is one of the most rapidly advancing techniques in the domain of medical imaging. Medical imaging techniques like MRI, computed tomography, X-ray imaging, ultrasound, and optical imaging methods have become a major backbone of modern medical diagnostics in clinical routine.

Among all these imaging modalities, certain characteristics render MRI a unique tool for *in vivo* examinations of various properties of human (and animal) organs and tissues:

- MRI is safe – no ionizing radiation is involved in the procedure
- MRI is a non-invasive method enabling longitudinal studies of the same anatomical region, e.g. for treatment follow-up
- a large variety of physiologically relevant parameters can be assessed
- anatomical structures and chemical properties, especially in soft tissues, can be identified
- whole-body imaging, at least in segments is possible

Since the first clinical use of MRI in the 1970s, image quality has been constantly improved. Despite these developments, MRI still has the drawbacks of long measurement times, relative insensitivity and high costs.

Nowadays, routine clinical applications of MRI typically use image resolution on the order of mm^3 . Improving the spatial resolution from $(1 \text{ mm})^3$ to $(100 \text{ }\mu\text{m})^3$ would correspond to a reduction of signal by a factor of 1.000 because the signal obtained from MRI is directly proportional to the number of contributing spins, i.e. the size of the elementary voxel. In order to obtain the same signal-to-noise ratio, the measurement time would have to be 1.000.000 times longer, which is obviously not a practical option.

Nevertheless, there is a way out of this dilemma. It is characterized by technological advances that have drastically improved the sensitivity of MR measurements. These developments can be summarized as follows:

- higher magnetic field strengths of modern MR scanners produce higher magnetization of the tissues and, therefore, generate stronger signal
- more efficient radio frequency coil design reduces noise in the signal detection process
- stronger gradients and low-noise pre-amplifiers have been developed
- pulse sequences for data acquisition have become more efficient based on growing expertise

High overall detection sensitivity boosts the signal-to-noise ratio, allowing for higher spatial and/or temporal resolution of the acquired images, which renders clinical applications requiring such very high resolution possible.

Employing smaller RF detectors improves sensitivity at the cost of a smaller field of view and penetration depth and, therefore, the most obvious applications for microscopic MR imaging *in vivo* are found in superficial areas of the human body, i.e. the skin.

A variety of dermatological diseases could greatly benefit from imaging techniques that allow investigation of dermal structures non-invasively. In systemic inflammatory vascular diseases like vasculitis, the pathology manifests first in the vessels of the skin before affecting other organs. Depiction and characterization of the cutaneous vessels could improve early diagnosis and, thus, have an impact on treatment and outcome. Also, due to the non-invasiveness of MRI, effects of therapeutic measures can be evaluated on the same anatomical location in longitudinal studies.

In this thesis, a combination of the different strategies to improve measurement sensitivity is applied in order to show images with the highest spatial resolution obtained in the skin of the living human so far.

Specificity of the measurements with respect to the detection of the cutaneous vascular system is achieved by using isotropic spatial resolution enabling segmentation of the vessel tree in three dimensions and by dedicated post-processing algorithms specifically designed to improve the visibility and contrast of vessels in the skin.

1.2 THESIS OUTLINE

The present chapter 1 puts the thesis into the context of biomedical research and explains the structure of this document.

Chapter 2 elucidates the underlying theoretical principles of the thesis, including a description of the magnetic resonance phenomenon, signal and noise in MR experiments, an overview of RF surface coil technology for MR microimaging, and the state of the art in skin imaging with MRI and other imaging modalities.

Chapter 3 describes the experimental studies performed at 1.5, 3, and 7 T, all of them targeting at ultra-high resolution imaging of the human skin in vivo with miniaturized RF coils. Each study is characterized by an explanation of the specific purpose, the materials and methods used, and the results obtained.

Chapter 4 deals with the image post-processing methods developed specifically for the purpose of better visualization and understanding of cutaneous vasculature.

Chapter 5 wraps up the findings of this thesis and discusses benefits and shortcomings of the methods used. Conclusions are drawn and perspectives and recommendations for related future studies are given.

Chapter 6 consists of annexes giving details about the calculation of the resonance frequency for multi-turn transmission line resonators and the MATLAB toolbox developed in the thesis for that purpose.

Chapters 7, 8, and 9 contain the list of references cited in this document, as well as lists of figures and tables.

Chapter 10 is a collection of publications and presentation abstracts for scientific conferences, based on work from this thesis.

2 THEORETICAL BACKGROUND

2.1 MAGNETIC RESONANCE

Nuclear magnetic resonance is based on the fact that every nucleus with a nuclear spin \vec{I} possesses a nuclear momentum $\vec{\mu}$, as in the classical model every spinning electric charge produces a magnetic field.

$$[\text{Eq. 1}] \quad \vec{\mu} = \underset{=1}{\frac{q}{e}} \cdot \underset{=\gamma}{\frac{g\mu_B}{\hbar}} \vec{I} = \gamma \vec{I}$$

The gyromagnetic ratio γ has a value of $2.68 \cdot 10^8 \text{ T}^{-1}\text{s}^{-1}$ for the most important nucleus in biological applications, the proton (^1H).

A magnetic dipole $\vec{\mu}$ in an external magnetic field \vec{B}_0 is subject to a torque

$$[\text{Eq. 2}] \quad \vec{N} = \frac{d\vec{I}}{dt} = \vec{\mu} \times \vec{B}_0$$

Together with [Eq. 1] and summation over an ensemble of spins

$$[\text{Eq. 3}] \quad \vec{M} = \sum_j \vec{\mu}_j$$

one obtains the equation of motion

$$[\text{Eq. 4}] \quad \frac{d\vec{M}}{dt} = \vec{M} \times \gamma \vec{B}_0$$

This describes a precessive motion of \vec{M} around $-\vec{B}_0$ at the Larmor frequency ω_0 .

$$[\text{Eq. 5}] \quad \vec{\omega}_0 = -\gamma \vec{B}_0$$

Without an external magnetic field, spins in a sample are randomly oriented resulting in a zero net magnetization of the ensemble. If an external magnetic

field \vec{B}_0 is applied, the z-component and magnitude of the spins are quantized into $2I+1$ distinct states. This phenomenon is called the Nuclear Zeeman Effect. For a spin of $\frac{1}{2}$, as is the case for 1H , spins are forced into two different energy levels, either parallel or anti-parallel to \vec{B}_0 . Their energy difference is

$$[\text{Eq. 6}] \quad \Delta E = \gamma \hbar B_0$$

In thermal equilibrium, the population of these two energy states follows Boltzmann statistics resulting in a small excess of spins in the lower energy state, i.e. with spin $+1/2$, aligned with the external magnetic field. This net magnetization represents the signal accessible in MR experiments and depends on temperature and the static magnetic field strength $B_0 = |\vec{B}_0|$. The population ratio between the two states is given by the Boltzmann equation

$$[\text{Eq. 7}] \quad \frac{n_{+1/2}}{n_{-1/2}} = \frac{e^{-\frac{E_{+1/2}}{k_B T}}}{e^{-\frac{E_{-1/2}}{k_B T}}} = e^{\frac{E_{-1/2} - E_{+1/2}}{k_B T}} = e^{\frac{\Delta E}{k_B T}} = e^{\frac{\gamma \hbar B_0}{k_B T}}$$

As can be seen from Figure 1, the deviation of this expression from 1 is in the ppm range, explaining the relative insensitivity of magnetic resonance, since only 1 – 5 in 100.000 spins are actually contributing to the measured signal.

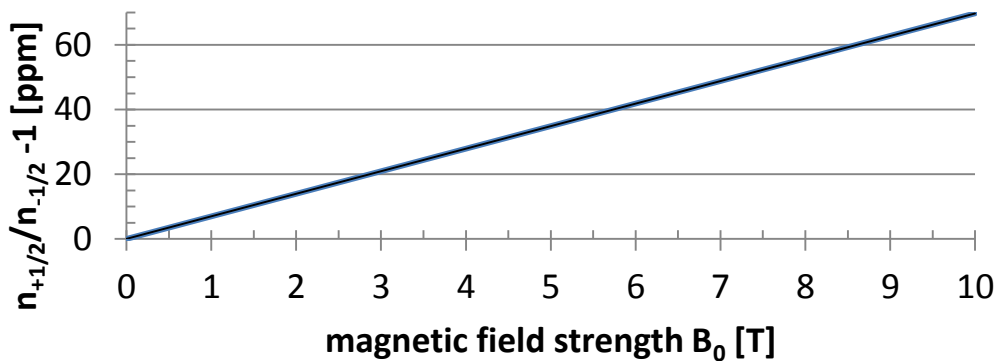


Figure 1: Spin excess in direction of \vec{B}_0
The curve is shown for protons at room temperature (293K).

The reason why we still detect a signal is by the sheer number of spins available in the human body.

The macroscopic magnetization M , as given by Boltzmann equilibrium law, is

$$[\text{Eq. 8}] \quad M = N \cdot \frac{\gamma^2 I(I+1)\hbar}{3k_B T} \cdot B_0$$

with N the number of nuclei present in the sample and T the spin temperature which is the sample temperature at thermal equilibrium between spins and the lattice.

Transition between Zeeman levels can be obtained by irradiation of the sample with an additional rotating magnetic field \vec{B}_1 if its photon energy equals the respective energy difference

$$[\text{Eq. 9}] \quad h\nu_0 = \Delta E, \quad \nu_0 = \frac{\omega_0}{2\pi}$$

Together with [Eq. 6] it follows that the sample has to be exposed to a radio-frequency (RF) field oscillating at the Larmor frequency for excitation of the spins from their equilibrium state, giving rise to the term “nuclear magnetic resonance” (NMR).

The magnetization vector can be tilted from the original direction parallel to the main magnetic field by a flip angle α in the rotating frame, i.e. the coordinate system rotating with the precessing spins at the Larmor frequency.

$$[\text{Eq. 10}] \quad \alpha(t) = -\gamma \int_0^t B_1(\tau) d\tau$$

where B_1 is the magnitude of the RF-field applied for excitation of the spins. After excitation, the magnetization will precess around the \vec{B}_0 axis and the spin system will return to the equilibrium state with characteristic relaxation times T_1 (spin-lattice relaxation) and T_2 (spin-spin relaxation), with $T_1 > T_2$.

The behavior of magnetization is described by the phenomenological Bloch equation [1] and illustrated in Figure 2

$$[\text{Eq. 11}] \quad \frac{d\vec{M}}{dt} = \underbrace{\vec{M} \times \gamma \vec{B}_0}_{\text{precession}} - \underbrace{\frac{M_x \vec{u}_x + M_y \vec{u}_y}{T_2}}_{\text{transverse relaxation}} - \underbrace{\frac{M_z - M_0}{T_1} \vec{u}_z}_{\text{longitudinal relaxation}}$$

The first term describes precessive motion of the magnetization around \vec{B}_0 and the two latter terms describe longitudinal and transversal relaxation processes. In matrix form the Bloch equation becomes

$$[\text{Eq. 12}] \quad \frac{d\vec{M}}{dt} = \begin{pmatrix} -1/T_2 & \gamma B_0 & 0 \\ -\gamma B_0 & -1/T_2 & 0 \\ 0 & 0 & -1/T_1 \end{pmatrix} \cdot \vec{M} + \begin{pmatrix} 0 \\ 0 \\ -M_0/T_1 \end{pmatrix}$$

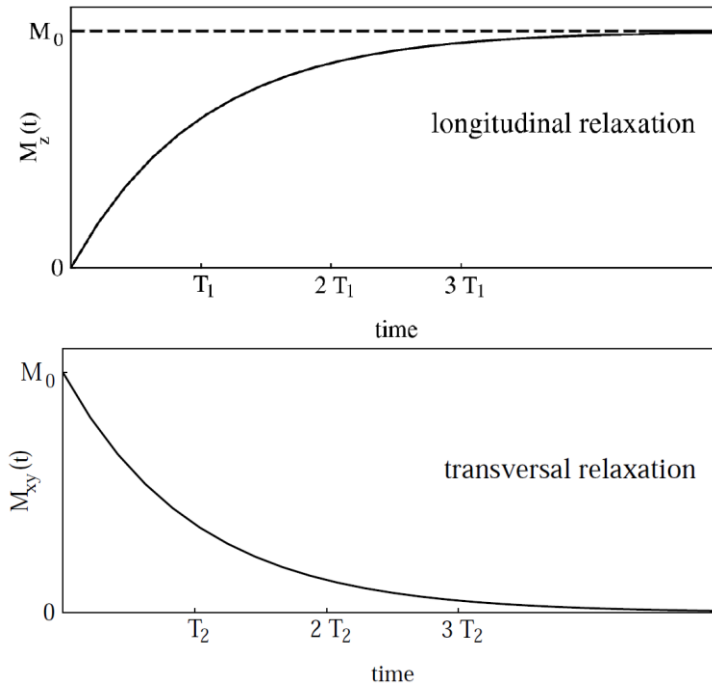


Figure 2: Relaxation mechanisms

Left: The magnetization component in direction of the main magnetic field returns to its equilibrium value with time constant T_1 due to spin-lattice interactions
 Right: The transversal magnetization component decays with time constant T_2 due to spin-spin relaxation.

2.2 SIGNAL AND NOISE IN MR EXPERIMENTS

2.2.1 Signal

2.2.1.1 Demonstration of the reciprocity principle

The reciprocity principle is one of the fundamental theorems in the theory of electromagnetics [2-6]. In antenna theory, it states that the receive sensitivity of an antenna is identical to its transmit field [7]. In other words, the magnetic field produced at a point in space by an RF coil run by a unit current is proportional to the electromagnetic force induced in the coil windings by a magnetic dipole at the same point [8-10]. This has been shown for the near, intermediate and far field zone of a magnetic dipole [11] and for arbitrary probe geometry [12]. The sensitivity of reception can, therefore, be calibrated by measuring the local B -field distribution of the receive coil used as a transmitter, a widely used technique for reconstruction in parallel imaging [13] or quantification of MR spectra [14].

In the following, we will derive an expression for the electromotive force generated by change of magnetic flux through a coil by the magnetization of the spins in a sample and show the relationship to the magnetic field created by the coil [15, 16].

2.2.1.1.1 Magnetic field produced by moving charges in a coil

Let us first calculate the magnetic field produced by the coil. The vector potential \vec{A} is defined, so that

$$[\text{Eq. 13}] \quad \vec{B} = \vec{\nabla} \times \vec{A}$$

From Ampère's law and the material equation for magnetic flux density \vec{B} and the magnetizing field \vec{H}

$$[\text{Eq. 14}] \quad \vec{\nabla} \times \vec{H} = \vec{J} \quad \text{and} \quad \vec{B} = \mu_0 \vec{H}$$

we get to the Poisson equation for the vector potential \vec{A}

$$\begin{aligned}
 \text{[Eq. 15]} \quad \Delta \vec{A} = \vec{\nabla}^2 \vec{A} = -\vec{\nabla} \underbrace{\left(\underbrace{\vec{\nabla} \cdot \vec{A}}_{=0} \right)}_{\text{(Coulomb gauge)}} + \vec{\nabla}^2 \vec{A} = -\vec{\nabla} \times \underbrace{\left(\vec{\nabla} \times \vec{A} \right)}_{=\vec{B}} = \underbrace{-\vec{\nabla} \times \vec{B}}_{\text{Ampère's law}} = -\mu_0 \vec{J}
 \end{aligned}$$

$\vec{a} \times \vec{b} \times \vec{c} = (\vec{a} \cdot \vec{c})\vec{b} - (\vec{a} \cdot \vec{b})\vec{c} \Rightarrow \vec{\nabla} \times (\vec{\nabla} \times \vec{A}) = \vec{\nabla}(\vec{\nabla} \cdot \vec{A}) - \vec{\nabla}^2 \vec{A}$

Its solution using Green's function is

$$\text{[Eq. 16]} \quad \vec{A}(\vec{x}) = \frac{\mu_0}{4\pi} \int_V d^3x' \frac{\vec{J}(\vec{x}')}{|\vec{x} - \vec{x}'|}$$

and therefore with [Eq. 13] we get Biot-Savart's law

$$\begin{aligned}
 \vec{B}_{coil}(\vec{x}) &= \vec{\nabla} \times \vec{A} = \frac{\mu_0}{4\pi} \int_V dV' \vec{\nabla}_{\vec{x}} \times \left(\frac{\vec{J}(\vec{x}')}{|\vec{x} - \vec{x}'|} \right) = \\
 &\vec{\nabla}_{\vec{x}} \times [\varphi(\vec{x}) \cdot \vec{J}(\vec{x}')] = \varphi(\vec{x}) \cdot \underbrace{[\vec{\nabla}_{\vec{x}} \times \vec{J}(\vec{x}')]_{=0}}_{\text{(curl operates on } \vec{x}, \text{ not } \vec{x}')} - \vec{J}(\vec{x}') \times [\vec{\nabla}_{\vec{x}} \varphi(\vec{x})] \\
 \text{[Eq. 17]} \quad &= -\frac{\mu_0}{4\pi} \int_V dV' \vec{J}(\vec{x}') \times \vec{\nabla}_{\vec{x}} \left(\frac{1}{|\vec{x} - \vec{x}'|} \right) = \\
 &\stackrel{\vec{J}(\vec{x}') \cdot dV' = I \cdot d\vec{l}}{=} -\frac{\mu_0 I}{4\pi} \oint_C d\vec{l} \times \vec{\nabla}_{\vec{x}} \left(\frac{1}{|\vec{x} - \vec{x}'|} \right)
 \end{aligned}$$

Note that integration over the current density in the whole volume has been replaced by integration over the current I in the coil windings.

2.2.1.1.2 Electromotive force induced in the coil by the spins

In the second step we calculate the electromotive force induced in the coil by the spins in the sample. The magnetic flux can be expressed as a function of the vector potential \vec{A}

$$\text{[Eq. 18]} \quad \phi(t) = \int_S \vec{B}_{spins} \cdot d\vec{S} \stackrel{\text{Stoke's theorem}}{=} \oint_C (\vec{\nabla} \times \vec{B}_{spins}) \cdot d\vec{l}$$

The contribution of the magnetization to the current density \vec{J} is given by

$$[\text{Eq. 19}] \quad \vec{J} = \vec{\nabla} \times \vec{M}$$

We use [Eq. 16] to calculate the vector potential at position \vec{x} in the coil wire from the sample's magnetization \vec{M}

$$[\text{Eq. 20}] \quad \vec{A}_{spins}(\vec{x}, t) = -\frac{\mu_0}{4\pi} \int_V \vec{M}(\vec{x}', t) \times \vec{\nabla}_{\vec{x}'} \left(\frac{1}{|\vec{x} - \vec{x}'|} \right) dV'$$

According to Faraday's law of induction, the electromotive force *emf* is given by

$$[\text{Eq. 21}] \quad emf(t) = -\frac{\partial \phi(t)}{\partial t}$$

If we now combine [Eq. 18], [Eq. 20], and [Eq. 21] the electromotive force created by the sample in the coil becomes

$$[\text{Eq. 22}] \quad emf(t) = -\frac{\partial}{\partial t} \oint_C \left(-\frac{\mu_0}{4\pi} \int_V \vec{M}(\vec{x}', t) \times \vec{\nabla}_{\vec{x}'} \left(\frac{1}{|\vec{x} - \vec{x}'|} \right) dV' \right) \cdot d\vec{l}$$

Using

$$[\text{Eq. 23}] \quad (\vec{M} \times \vec{\nabla}) \cdot d\vec{l} = -\vec{M} \cdot \left(d\vec{l} \times \vec{\nabla} \left(\frac{1}{|\vec{x} - \vec{x}'|} \right) \right)$$

and by reversal of integration order we obtain

$$[\text{Eq. 24}] \quad emf(t) = -\frac{\partial}{\partial t} \int_V \left(\vec{M}(\vec{x}', t) \cdot \underbrace{\frac{\mu_0}{4\pi} \oint_C d\vec{l} \times \vec{\nabla}_{\vec{x}'} \left(\frac{1}{|\vec{x} - \vec{x}'|} \right)}_{=\vec{B}_{coil}(\vec{x}') \text{ with } I=1} \right) \cdot dV'$$

The expression marked with the curly bracket corresponds to the magnetic field of a coil with unit current $I = 1$ [Eq. 17]. We therefore conclude

$$[\text{Eq. 25}] \quad \text{emf}(t) = -\frac{\partial}{\partial t} \int_V \vec{M}(\vec{x}', t) \cdot \vec{B}_{\text{coil}}(\vec{x}') \cdot dV'$$

This shows that the voltage induced in the receive coil by the spins is proportional to the magnetic field that would be produced by the coil per unit current when used as a transmitter, which demonstrates the reciprocity principle [17].

2.2.1.2 The signal equation

If we consider a time-varying gradient $G(x,y,z,t)$ with its components G_ξ ($\xi = x, y, z$) as used in MR imaging sequences for signal localization, the transverse component of the magnetization

$$[\text{Eq. 26}] \quad M_{xy} = M_x + i \cdot M_y$$

can be calculated from the solution of the Bloch equation [Eq. 11]:

$$[\text{Eq. 27}] \quad M_{xy}(x, y, z, t) = M_0(x, y, z) \cdot e^{-\frac{t}{T_2(x,y,z)}} \cdot e^{-i\omega_0 t} \cdot e^{-i\gamma \int_0^t d\tau \sum_{\xi=x,y,z} G_\xi(\tau) \cdot \xi}$$

Using the above reciprocity theorem [Eq. 25], the signal measured in an MR experiment can be described as the electromotive force of the transversal component of the magnetization \vec{M} precessing around the static magnetic field \vec{B}_0 induced in the windings of an RF coil [18]. The signal that is received in the RF coil is the sum of signals of all spins within the sensitive area of that coil. After demodulation by ω_0 we can, therefore, write the signal as

$$[\text{Eq. 28}] \quad S(t) \propto \int_V M_0(x, y, z) \cdot e^{-\frac{t}{T_2(x,y,z)}} \cdot e^{-i\gamma \int_0^t d\tau \sum_{\xi=x,y,z} G_\xi(\tau) \cdot \xi} dx dy dz$$

With the spatial frequencies k_ξ defined as

$$[\text{Eq. 29}] \quad k_\xi(t) = \frac{\gamma}{2\pi} \int_0^t G_\xi(\tau) \cdot d\tau, \quad \xi = x, y, z$$

and, ignoring, T_2 relaxation we obtain

$$[\text{Eq. 30}] \quad S(t) = \int_V M_0(x, y, z) \cdot e^{-i2\pi \sum_{\xi=x,y,z} k_\xi(t) \cdot \xi} dx dy dz = FT[M_0(x, y, z)]$$

This is called the signal equation. FT is the Fourier transform taken at the spatial frequencies k_ξ . This formula states that during acquisition, data is read in Fourier domain, usually called *k-space* in MR. The image can then be reconstructed by taking the Fourier transform of the acquired k-space data.

2.2.2 Noise

In MR experiments, data quality is mainly restricted by different types of noise superimposed on the MR signal. In the following sections the main influences on the signal to noise ratio (SNR) are outlined, noise sources are identified and their respective importance is evaluated.

The SNR available at the coil output is limited by dissipation in the coil media, the sample and all other involved media such as receiver electronics.

Following the fluctuation dissipation theorem [19], noise sources are powered by thermal agitation in dissipating media resulting in a fluctuating electromotive force in series with the equivalent resistance [20]. The noise standard deviation is

$$[\text{Eq. 31}] \quad v = \sqrt{4k_B R_{eq} T_{eq} BW}$$

with k_B being Boltzmann's constant, $R_{eq} T_{eq}$ the temperature-weighted sum of equivalent resistances of all noise sources, and BW the receiver bandwidth.

The main factors contributing to noise in MR experiments are detailed in the following section.

2.2.2.1 Noise sources

The different origins of noise contributing to the total noise superimposed on the MR signal are discussed below.

2.2.2.1.1 Sample noise

The most constraining, but inevitable, source of noise in an MR experiment is the sample itself. Sample conductivity and temperature govern its contribution to noise induced in the RF coil circuit. There are three different mechanisms that make up the total sample noise: magnetically coupled noise, capacitively coupled noise, and spin noise.

2.2.2.1.1.1 Magnetic coupling

Magnetically coupled noise originates from thermally agitated electric charges within conductive samples, such as biological tissues. Circular components of the Brownian motion of these charges induce a voltage in the RF receiver circuit and are, therefore, detected in the same way as the nuclear magnetization and result in random fluctuation of the measured signal.

Sample losses also occur due to eddy currents induced by \vec{B}_1 in conductive samples. Part of the RF power is absorbed in the tissue resulting in tissue heating. It depends on electric charge mobility and tissue conductivity σ , which has an average value of about 0.7 S/m for biological tissues at 300 MHz and is frequency dependent. In the case of a homogeneous spherical sample of radius a , the equivalent resistance of the sample R_s becomes [21]

$$[\text{Eq. 32}] \quad R_s = \frac{2\pi}{15} \sigma \omega^2 \left(\frac{B_1}{I} \right)^2 a^5$$

2.2.2.1.1.2 Capacitive coupling

RF currents applied to the coil windings create electric potential differences which evoke alternating electric field lines that reach the sample surface and induce dielectric losses there. Inversely, thermally fluctuating dipoles on the sample's surface induce noise in the RF coil. This coupling does not use the magnetic induction pathway and can therefore be separated from the MR signal by means of coil design. The most efficient coils use distributed series capacitors (see section 2.3.2.2.2) reducing coil impedance, as well as inductive coupling transformers (see section 2.3.3.2) that equilibrate the electric potential with respect to the sample [22].

2.2.2.1.1.3 Spin noise

Spin noise is produced by the nuclear spin system itself and is caused by fluctuating transverse magnetic moments. The equivalent loss resistance by reciprocity R_{spin} [10, 23] is only considerable within close on-resonance conditions.

$$[\text{Eq. 33}] \quad R_{spin} = \gamma \left(\frac{B_1}{I} \right)^2 \left(\frac{\omega}{\delta\omega} \right) M_L V_S$$

with γ being the gyromagnetic ratio, $\delta\omega$ the effective NMR linewidth and M_L the longitudinal magnetization component. In MRI, spin noise has no great influence on the experiment because readout gradients spread the resonance over several kHz, while high-resolution spectroscopy with linewidths of about 1 Hz suffers heavily from spin noise mechanisms.

2.2.2.1.2 Coil noise

2.2.2.1.2.1 Normal conductors

In normal conductors, internal losses result from power dissipation by scattering of free electrons. Inversely temperature evokes random motion of the charge carriers, inducing voltage fluctuations at the coil ends. The losses

due to these effects can be described by the equivalent internal coil resistance R_C , described by [24] as follows:

$$[\text{Eq. 34}] \quad R_C = \sqrt{\frac{\rho_C \mu_0 \omega}{2}} n^2 \xi \frac{a}{r}$$

where ρ_C is the material resistivity, μ_0 the vacuum permeability, n the number of coil windings, a the average coil radius and r the wire radius. The factor ξ expresses the influence of the proximity effect. Please note that R_C depends on $\omega^{1/2}$, as opposed to the ω^2 dependence of the magnetically coupled sample noise.

2.2.2.1.2.2 Superconductors

Due to the very low surface resistance of superconductors, their respective coil noise will be far below the value of normal conductors. Type-I superconductors, which show ideal superconducting properties throughout the sample below the critical temperature T_C , will show no dissipation and no thermal noise when conducting. Unfortunately, this type of superconductor is only available with very low T_C which is technically incompatible with a clinical environment.

A breakthrough for superconductivity applications was achieved when Bednorz and Mueller found type-II high temperature superconductors in 1986 [25]. At higher transition temperatures high temperature superconductors (HTS), allow quantum flux vortices containing “normal” free electrons to penetrate the material resulting in non-zero dissipation. Phenomenological superconductor theory based on London’s equations yields a RF surface resistance dependence on ω^2 [26, 27].

2.2.2.1.2.3 Electrical quality factor Q

Classically, power losses in the RF-coil can be described by the electrical quality factor of the coil, defined by

[Eq. 35]
$$Q = \frac{L_{eq}\omega}{R_{eq}}$$

where L_{eq} represents the equivalent self-inductance, i.e. the magnetic energy stored by unit current in the coil windings, R_{eq} is the equivalent resistance brought in by the loss mechanisms in the coil.

2.2.2.2 Noise regimes

For the amelioration of MR sensitivity it is of great importance to know which noise source is dominant and thus limits the achievable sensitivity.

Since sample noise is intrinsic to the examined object or tissue, it is desirable to carry out measurements under such circumstances where the SNR is only limited by the sample and not by coil noise mechanisms. Therefore, a semi-empiric log-log plot of the borders of sample-noise-dominated and coil-noise-dominated regimes [28] is given in Figure 3, comparing different coil materials with varying coil diameters for a vast range of RF frequencies.

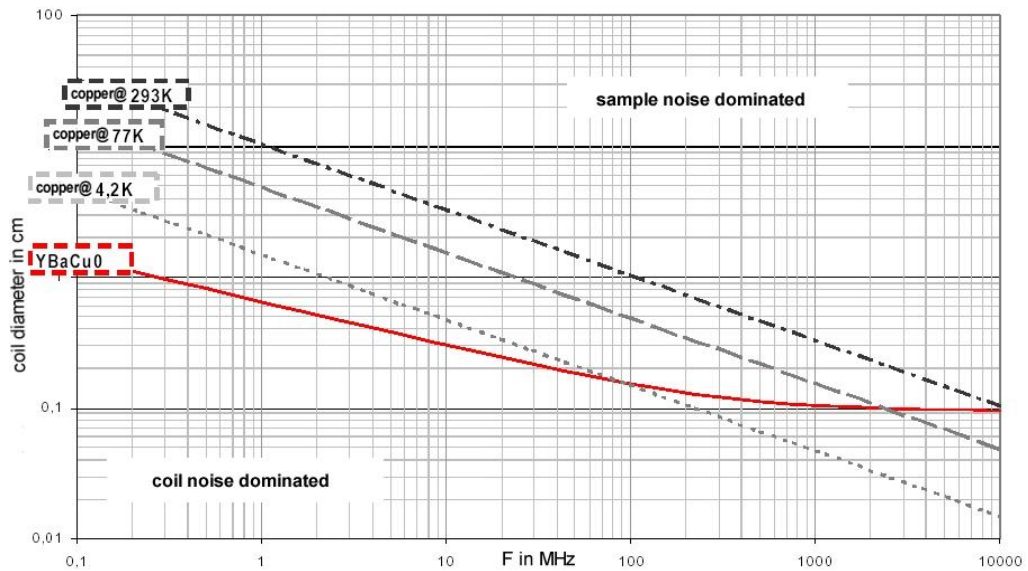


Figure 3: Noise regimes

Noise regime limits for copper coils at room temperature, liquid nitrogen temperature (77 K) and liquid helium temperature (4.2 K) are drawn in black and gray. The noise regime limit for superconducting coils is given in red. Both axes are on a logarithmic scale. (Modified from [28])

The boundaries are defined by $R_C T_C = R_S T_S$ with R being equivalent resistance and T being temperature, for the coil and the sample, respectively. For a given frequency and a given coil diameter, the dominant noise mechanism is, therefore, determined by the characteristics of the coil material and temperature used.

As can be seen from Figure 3, smaller coil diameters resulting in higher sensitivity (on a smaller field of view) can be achieved by cooling.

The area above the border between the two noise regimes is where the induced noise in the sample is dominant. It is desirable to conduct measurements in this regime. For a given frequency, the size of the coil has to be greater than a certain value in order to stay in the domain of sample dominated noise, restricting miniaturization of the coil.

Contrary to the sample noise predominance regime, in the coil noise dominated regime the losses due to internal coil noise are the limiting factors for the sensibility of the imaging process. It is, therefore, recommended to use a cooled coil or increase the size of the coil in order to shift back to the sample-noise dominated regime.

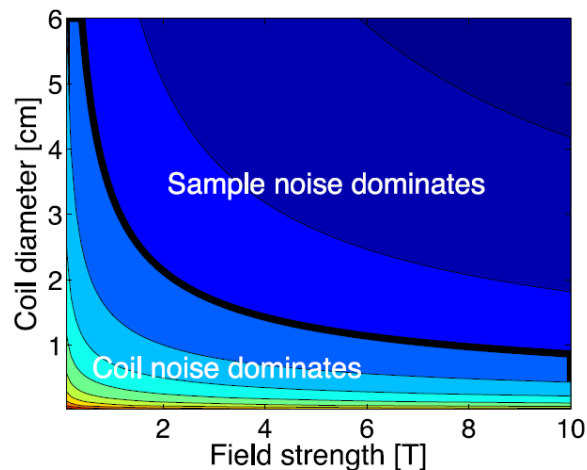


Figure 4: Alternative representation of noise regimes

Another representation of the noise regime limit for a copper loop at room temperature. Axes are on a linear scale (from [29]).

2.2.2.2.1 Copper coils

For high main magnetic field strengths the limitation for copper coils is not so stringent, because normal conductor resistance depends on $\omega^{1/2}$ and sample noise on ω^2 , explaining the decline of the curves for copper coils in Figure 3.

2.2.2.2.2 HTS coils

Because magnetically coupled sample noise and internal superconducting coil noise both depend on ω^2 , the boundary between coil- and sample-dominated noise regimes becomes frequency independent [30-32]. In Figure 3, for a HTS superconductor made of YBaCuO, this would yield a horizontal line at a coil diameter of about 1 mm. When exposed to an external magnetic field, however, type-II materials show degradation in electrical properties due to an increasing number of flux vortices penetrating the coil, an effect that is highly anisotropic and non-linear.

The anisotropy results from the crystalline structure of HTS, where superconductivity occurs along the Cu-O planes. In Figure 3 this is expressed by a frequency dependence of the YBaCuO line. This degradation effect is minimized when the external magnetic field is aligned parallel to the orientation of these planes.

Assuming a maximal misalignment of the coil in respect to the main magnetic field B_0 of 5° , the shape of the YBaCuO boundary has been extrapolated from surface resistance data for different field strengths and orientations [33].

2.2.2.2.3 Comparison: HTS vs. copper coil

Superconducting coils show considerable advantages as compared to copper coils especially at low and moderate field strengths. As an example, for proton MR at 1.5 T, i.e. at a resonance frequency of 63.87 MHz, using a standard copper coil at room temperature limits the minimum coil diameter to about 1.2 cm, in order to rest in the sample-noise dominated regime. Under the same circumstances, when using a YBaCuO HTS coil, the diameter could be reduced

to approximately 0.2 cm theoretically, without introducing a sensitivity limitation by internal coil noise mechanisms.

At 7 T the minimum size for a copper coil at room temperature is about 5 mm; a YBaCuO coil could be of 1 mm in diameter. For practical and technological reasons, the smallest HTS coils developed so far are of 6 mm in diameter. More about the actual coil design can be found in chapter 2.3.

2.2.3 Signal to noise ratio and sensitivity

SNR is defined as

$$[\text{Eq. 36}] \quad \text{SNR} = \frac{\text{signal intensity}}{\text{standard deviation of gaussian noise}}$$

An expression for SNR can, therefore, be derived from the quotient of [Eq. 25] and [Eq. 31]

$$[\text{Eq. 37}] \quad \text{SNR} \approx F^{-1/2} \frac{\omega \cdot (B_1 / I)}{\sqrt{4k_B R_{eq} T_{eq} BW}} V_0 M_T \sqrt{t_{acq}}$$

where F is a noise factor introduced by the acquisition electronics, ω is Larmor's frequency, B_1 the magnetic field created by the coil, I the current in the coil, V_0 is the volume of the encoded voxel, carrying a transversal magnetization M_T , BW is the read-out bandwidth and t_{acq} the total acquisition time [34].

The sensitivity factor S_{RF} of the RF coil is included in this formula and represents the SNR contribution of the coil in time-domain at given imaging parameters:

$$[\text{Eq. 38}] \quad S_{RF} = \frac{\omega \cdot (B_1 / I)}{\sqrt{4k_B R_{eq} T_{eq}}}$$

where $R_{eq} T_{eq}$ represents again the temperature-weighted sum of equivalent resistances of all noise sources. The factor

$$[Eq. 39] \quad M_T \sqrt{\frac{dt}{t_R}}$$

can be interpreted as the transverse magnetization effectively collected over the scan duration. If this factor and S_{RF} are considered constant for a given experiment, the trade-off between SNR, acquisition time t_{acq} and voxel volume V_0 is expressed via

$$[Eq. 40] \quad SNR \propto V_0 \cdot \sqrt{t_{acq}}$$

Decreasing V_0 by a factor of 1000, i.e. the spatial resolution by a factor of 10 in all 3 dimensions, the acquisition time has to be increased 10^6 -fold in order to maintain the same SNR. This shows that enhancing sensitivity is of utmost importance to improve image resolution significantly.

2.2.3.1 Scaling rules

A summary of scaling rules for Q, SRF and SNR in the extreme cases of a perfect, non-conducting sample and a perfect, lossless coil is displayed in Table 1. This means that in the first case, all noise comes from the coil, i.e. $R_{eq}T_{eq} = R_C T_C$ and in the latter all noise comes from the sample, i.e. $R_{eq}T_{eq} = R_S T_S$.

2.2.3.2 Increasing measurement sensitivity

This chapter describes three complementary methods to further increase MR sensitivity. Each of these methods has its benefits and drawbacks and it has to be examined carefully which method is applicable in any specific case. Important factors for these decisions are the size of the sample to be examined, the desired spatial resolution, the field strength available, costs and applicability in clinical environments, e.g. measurement time or patient access.

	Only coil losses Non-conducting sample	Only sample losses lossless coil
Quality factor Q	$d\sqrt{\omega}$	$\frac{1}{d^2\omega}$
RF sensitivity S_{RF}	$\frac{\omega^{3/4}}{d}$ *	$d^{-5/2}$
SNR	$d^2\omega^{7/4}$ **,*	$\sqrt{d} \cdot \omega$ **

Table 1: Scaling rules for Q, coil sensitivity and SNR

The table shows how the electric quality factor Q, the RF sensitivity S_{RF} and the signal-to-noise ratio SNR scale with field strength and coil size in two different regimes. (from [29, 34])

* ...with constant filling factor η (see section 2.2.2.1)

** ...with linear increase of effective M_T with ω and $V_0/V_S=\text{const.}$

2.2.3.2.1 Magnetization enhancement

2.2.3.2.1.1 Higher static magnetic fields

Increasing the main static field B_0 increases the Larmor frequency ω and the transversal magnetization M_T , and thus improves SNR when leaving the other parameters unchanged in [Eq. 37]. There are, however, intrinsic changes to relaxation mechanisms, chemical shifts and local field gradients caused by susceptibility differences of different tissues and air within the sample when higher field strengths are used [35].

According to [Eq. 38], the sensitivity S_{RF} of an MR experiment increases linearly with the Larmor frequency ω , and, thus with B_0 . In addition, Figure 3 reveals that at higher frequencies, smaller coils can be used, reducing the effective size of the sample covered by the coil, again enhancing the SNR by increasing the quality factor Q .

When using superconducting coils, higher static fields can be restricting because of the orientation dependent deterioration of electrical properties of the coil when exposed to high field strengths (see section 2.2.2.1.2.3).

2.2.3.2.1.2 Contrast agents

Magnetization can also be dynamically increased by injection of paramagnetic substances such as Gadolinium-DTPA. These paramagnetic complexes influence relaxation times and produce larger image contrasts [36]. However, dynamical magnetization enhancement is not part of the investigated field in this report, and will therefore not be dealt with in more detail.

2.2.3.2.2 RF coil miniaturization

According to Table 1, under the condition of sample-noise predominance, the RF coil sensitivity S_{RF} scales with $d^{-5/2}$. Thus, using smaller coils provides considerable improvement, because the limitation of the field-of-view results in an effective sample-size reduction. For MR microscopy, surface coils are used because of their limited field of view, reducing the volume that has to be encoded.

From [Eq. 38] we see that coil sensitivity is linearly dependent on the amplitude of the magnetic field produced by the coil per unit current B/I . This can be easily demonstrated using Biot-Savart's Law. Let us consider a current I running on a circular lossless loop with radius r . The magnetic field created in the center of the loop is given by Biot-Savart's Law

$$[\text{Eq. 41}] \quad B = \frac{\mu_0 I}{2r}$$

A coil that is smaller by a factor F and driven by the same current I will, therefore, produce a magnetic field that is F times higher than that of the larger coil. This is illustrated in Figure 5.

The question of optimal positioning of RF coils with respect to the target area of the subject can be roughly approximated by simplified analytical models.

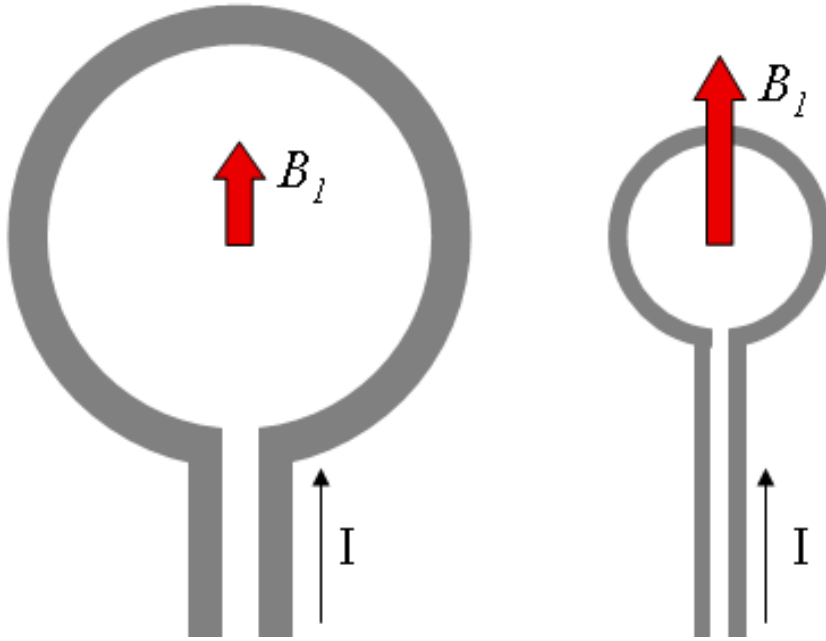


Figure 5: Influence of coil size on sensitivity

Two coils with identical current I only differing in size by a factor of F . According to Biot-Savart's Law, the B_1 -field created by the smaller coil is F times higher.

In the case of a circular lossless loop of radius a at the surface of a semi-infinite sample (distance $d=0$), the highest SNR can be achieved at the depth p from the coil inside the sample, when the following condition is met [37]:

$$[\text{Eq. 42}] \quad a = \frac{p}{\sqrt{5}}$$

With $\sqrt{5} \approx 2$ this could roughly be interpreted as: "Optimal SNR for a given depth p is achieved with a coil diameter of p ".

For coil positions further away from the sample, i.e. at a distance d from the sample surface, the right hand side of Figure 6 shows the degradation of the SNR in percent of the optimal value at $d=0$ and $a=p/5^{1/2}$ [38]. This is important, because superconducting coils, which have to be thermally insulated from the sample, cannot be placed closer to the sample surface than the thickness of the thermal insulation used, which is currently around 1-2 mm (see section 2.3.1.3).

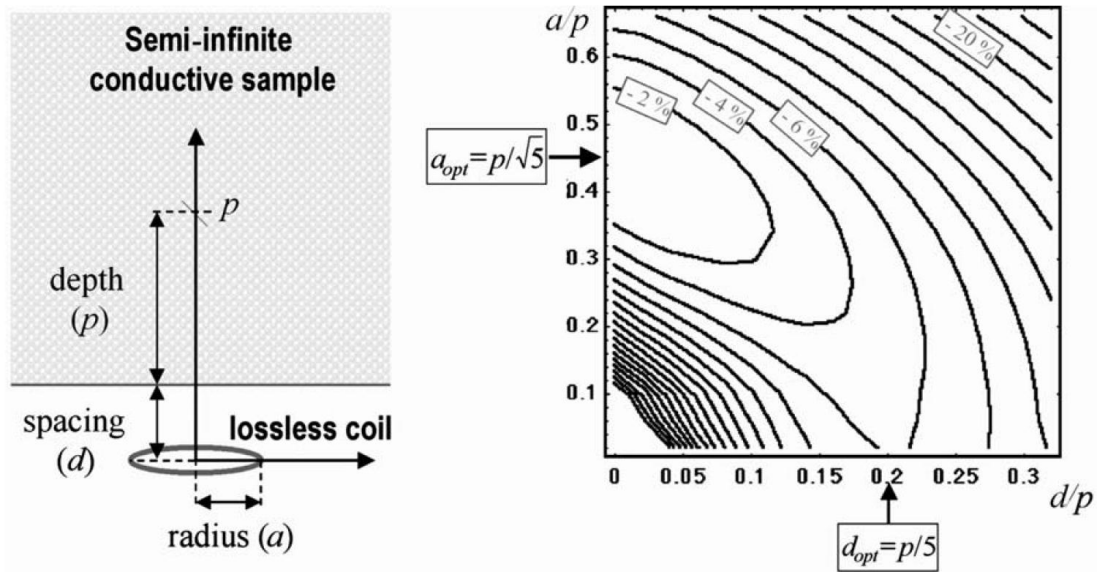


Figure 6: Optimization of size and position for a lossless circular coil

The SNR in the desired depth p in the sample depends on the radius a of the coil and its distance d from the sample. (Reproduced from [34])

2.2.3.2.1 Coil arrays

The price to be paid when using smaller surface coils is that only very local exploration of the sample can be performed at high spatial resolution. If greater areas are to be examined this problem can be overcome by using multiple coils in parallel, i.e. a coil array. The “NMR phased array” was first described in [39]. Arrays offer the possibility to detect the NMR signal (and the respective noise) under optimal SNR conditions for different areas of the field of view simultaneously.

2.2.3.2.3 Cooling of RF coils

Another possibility to decrease coil losses is to cool the RF coil. Cooling the coil material has actually two positive consequences: on the one hand the temperature in $R_c T_c$ is reduced directly and on the other hand, the coil’s conductivity increases at lower temperatures (e.g. copper), decreasing the coil resistance R_c .

For superconducting coils it is a prerequisite that the coil is cooled, because otherwise it would not be superconducting. When this state is reached, the equivalent resistance of the coil is some orders of magnitude lower than with normal conducting coils.

The main disadvantage of the cooling approach is its technical difficulty, because conventional cryo-systems are not suitable for an MR environment due to metallic and ferromagnetic parts involved. An effort has been made to develop dedicated cooling systems, which will be described in chapter 2.3.1.3.

2.3 RF SURFACE COIL TECHNOLOGY FOR MR MICROIMAGING

This chapter deals with the theoretical and technical aspects of RF coils, and particularly RF coils dedicated to high resolution imaging [40, 41]. These aspects include coil design (material, geometry, connection to the receiver) and several examples of cooling techniques for RF coils in MR environments. Different types of surface coils for MR microscopy and their connection to the receiver unit will be discussed.

2.3.1 RF coil materials

2.3.1.1 Copper

The most commonly used material for normal conducting RF coils is copper because of its high conductivity of 58.0 MS/m at room temperature (293.15 K=20°C), its malleability and ductility. Silver has an even higher conductivity of 61.4 MS/m at room temperature with the disadvantage of a slightly lower ductility and higher costs.

Since a higher conductivity represents reduced resistivity to the movement of the charge carriers, the electrical quality factor of a coil Q will be higher for materials with high conductivity.

Normal conductors show a typical behavior with temperature expressed by the empirical formula

$$\text{[Eq. 43]} \quad \rho = \rho_0 + \alpha T$$

where ρ is the specific resistivity at a given temperature T in Ωm , ρ_0 the specific resistivity at 0 K and α the linear temperature coefficient denoting the assumed linear change of resistivity per Kelvin. ρ_0 is due to impurities in the conductor material, expressing that the resistivity of a normal conductor will

not approach 0 when the temperature is lowered to 0K. Nevertheless, conductivity increases when the material is cooled (with positive values for α).

2.3.1.2 Superconductors

Unlike normal conductors, superconductors show a spontaneous drop in resistivity to a negligible level below a material-dependent critical temperature T_c .

2.3.1.2.1 Low temperature superconductors

Low temperature superconductors are usually type I superconductors, this means they have only two states – entirely superconducting (Meißner phase) or not. Such materials are commonly used as the coil material for large coils manufactured to provide the main magnetic field B_0 of an NMR scanner. Most commonly used materials are Niobium-3-Tin or Niobium-Titane. Their critical temperatures are far below the boiling point of nitrogen, which renders them not suitable for RF coils.

2.3.1.2.2 High temperature superconductors

High temperature superconductors (HTS) have only been discovered about 25 years ago [25]. They usually consist of ceramics with Copper-oxygen layers that are responsible for superconductivity. The most commonly used and also best investigated material is $YBa_2Cu_3O_{7-\delta}$, also called YBCO. Its critical temperature is around 90 K, easily achievable with liquid nitrogen.

HTS typically are type II superconductors, which means that at field strengths above the lower critical field H_{c1} flux vortices containing normal conducting electrons penetrate the superconductor until, at the upper critical field H_{c2} , the probe is entirely in normal conduction state. Both, H_{c1} and H_{c2} , are depending on temperature and current running through the coil. Movement of the flux vortices due to electromotive forces causes dissipation.

2.3.1.3 Cooling techniques

There are different methods to cool RF coils, all of them aim at providing a cryogenic device which fits into a medical environment and at minimizing the distance between coil and sample. This requires devices that can sustain a high temperature difference of about 200° within a few millimeters. Furthermore, the whole cryogenic system must be made of NMR-compatible, i.e. non-magnetic materials.

2.3.1.3.1 Direct immersion in liquid cryogenic bathes

Liquid bathes offer a rather simple method to cool the coil. In this case the coil is immersed directly inside a cryogenic liquid, such as liquid nitrogen (LN2). The LN2 can be contained in polystyrene foam vessels, non-conductive Dewars made of e.g. PVC or fiberglass composites. The autonomy of these cooling devices is restricted by the amount of cryogenic liquid contained and the quality of the thermal insulation of the system. The autonomy time could be extended by supplying a LN2 stream through flexible pipes connected to a remote Dewar.

Unfortunately, problems with mechanical vibrations, thermal instabilities and RF fluctuations, caused by boil-off and bubbling may arise. Also mechanical stress caused by very fast cooling may deteriorate the properties of the coil material.

2.3.1.3.2 Cold ends

In order to overcome some of the difficulties encountered with direct immersion in liquid bathes, the coil could either be encapsulated in an inner vessel inside the liquid bath [42, 43] or at the end of a so-called cold finger [31, 44-46]. Cold fingers are made of solids with high thermal conductivity and low dielectric losses, such as sapphire or alumina. One end of the finger is immersed in a cryogenic bath, while the coil is attached to the other end, in an evacuated vessel ensuring high temperature gradients from the coil to the

sample. The coil is therefore no longer in direct contact with the bath, resolving most of the problems mentioned in section 2.3.1.3.1.

Problems are the time of autonomy of the system and ensuring sufficient thermal contact between the cold finger and the coil. Ideally the coil itself is integrated onto a dielectric substrate also serving as a cold finger [47, 48] (as it is the case for the coils described in 2.3.2.2.2).

Gaseous cold ends, i.e. a liquid bath in thermal contact with a gaseous vessel containing the coil, have also been tested, achieving temperatures down to 150K with a LN2 bath [49] and 15K with liquid He bathes [50]. With the lower-cost LN2 this technique does not seem to be a feasible way to cool superconducting coils below their critical temperature, however.

2.3.1.3.3 Closed-cycle cooling

Reservoirs with enclosed cryogenic fluids as described in the sections above are not suited for use in routine medical applications. Such closed-cycle cryocoolers are needed to solve the problem of autonomy and provide simple push-button operation. No more handling with cryogenic fluids is required.

Closed-cycle coolers rely on compression and expansion principles, thus, requiring a compressor and a heat exchanger. Different types of machines could be used, i.e. Stirling, Gifford-McMahon or pulsed tubes. Stirling machines are based on isochoric cycles and have a major disadvantage in this context: they only achieve high performances if the compressor is close to the cold end. Gifford-McMahon machines use a rotating valve and work on isobaric cycles and have already been used to cool commercially available RF coils for high-resolution MR-spectroscopy [48]. The drawback of both of these techniques is that mechanical vibrations and electromagnetic interferences with the NMR system are produced.

A promising alternative are pulsed tube techniques [30, 51], which do not have any moving parts near the cold end. Their working principle is very similar to that of Stirling or Gifford-McMahon machines, but the displacer is replaced by laminar pressure waves. This reduces mechanical and

electromagnetic perturbations by several orders of magnitude, i.e. to a negligible level.

Other closed-cycle coolers are based on the isenthalpic expansion of high-pressure gases in the Joule-Thomson process, as used in conventional refrigerators. They have already been employed in MR microscopy [52].

2.3.2 Geometry

Surface coils are dedicated to localized imaging or spectroscopy of the sample. They produce an inhomogeneous RF field, diminishing with distance to the coil. Close to the coil, they achieve higher SNR than volume coils because of the higher filling factor η and also have the advantage of lower intrinsic losses.

Surface coils are usually made of one or more planar circular loops and must have a resonance frequency equal to the Larmor frequency of the investigated nuclei. Different types of surface coils have been developed in order to achieve this goal and will be detailed in the following sections.

2.3.2.1 “Classical” surface coils

The easiest and most commonly used way to adapt a coil’s frequency ω is to fix its inductance L by choice of the coil geometry and then add an appropriate capacitor C by soldering it to the line, according to the formula

$$[\text{Eq. 44}] \quad \omega = \frac{1}{\sqrt{L \cdot C}}$$

The shape of the surface coil can be almost arbitrary; the geometry should be adapted to the desired anatomical region to be measured. The inductance of the coil depends strongly on the coil shape.

For small coils, the inductance will be much lower as compared to larger ones. Therefore, the capacitance in the resonant circuit has to be increased in order to maintain the desired resonance frequency. The inductance can be increased by adding more turns to the spiral, which will lead to technological, i.e. geometrical, restrictions sooner or later.

Additionally, as the size of the coil is drastically reduced, susceptibility differences introduced by the capacitor element(s) become a limitation to the homogeneity of signal received with the coil. Soldering joints create additional losses in the coil and are, therefore, not suitable for superconducting coils in particular.

2.3.2.2 Auto-resonant structures

2.3.2.2.1 Localized elements

An improvement for surface coils with discrete elements consists in manufacturing monolithic auto-resonant (see section 2.3.3.2) coils, i.e. from one material without soldering and discrete electronic elements such as capacitors. The appropriate resonance frequency is achieved by careful choice of the coil geometry.

Coils with localized elements do not contain discrete electric elements, but areas dedicated to inductance and capacity can still be identified.

Two different approaches will be described here, the first being a “spiral” geometry published by [42]. It consists of two spirals attached to both sides of a thin dielectric plate, using the outermost and innermost windings of each spiral to produce a capacity (see Figure 7). This configuration makes analytical estimation of the resonance frequency extremely difficult and its adjustment cannot be done other than empirically – a fact that explains why this configuration has not been used frequently.

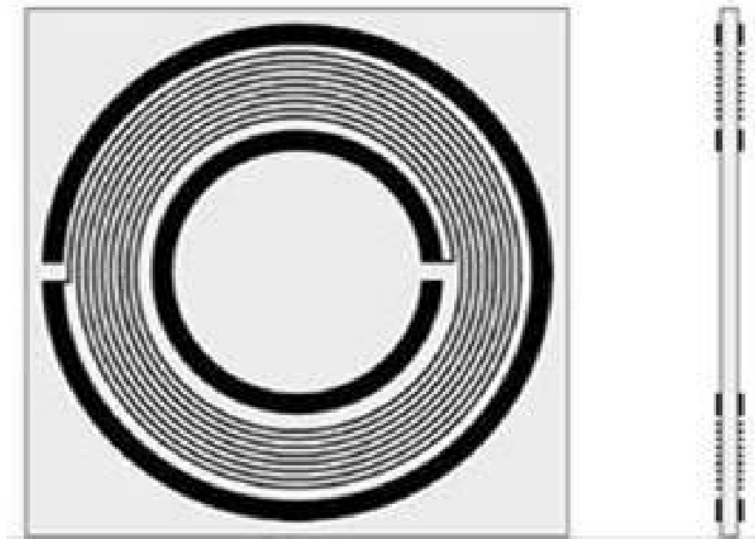


Figure 7: Coil with localized elements (spiral)
Left: view from top
Right: View from the side. (reproduced from [34])

The second approach uses so-called “interdigitated capacities” and has been studied, among others, by [53]. This geometry features two concentric circles with interleaved fingers (capacitive digits) as shown in Figure 8.

The inductance is mainly produced by the circular components and the capacity is achieved through the capacitive digits perpendicular to the circles. A major drawback of this design is that the number of turns cannot be increased. Also the estimation of the resonance frequency is generally not possible because of the very complex capacitive and inductive coupling phenomena.

Usually the matching of this coil is done by cutting off capacitive fingers, which lowers the resonance frequency by about $100/N$ %, with N being the number of fingers. Hence, for very exact matching, a large number of fingers has to be used, soon limited by technological restraints.

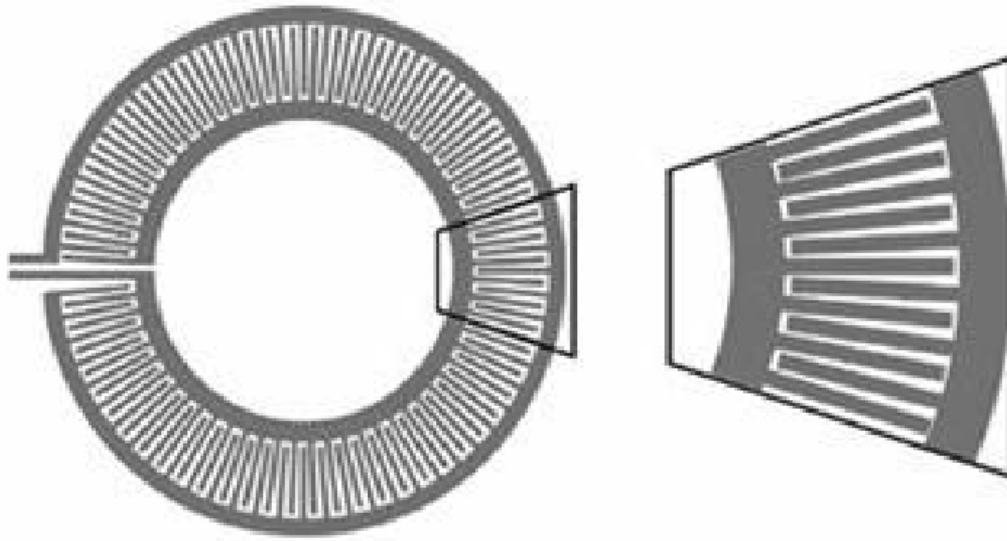


Figure 8: Coil with localized elements (interdigitated capacities)

Left: view of the entire coil from top.

Right: zoomed coil detail. (reproduced from [34])

2.3.2.2.2 Distributed elements

Coils with distributed elements show the same local values of capacity and inductance along the windings. Resonators of this type are based on the principle of split-conductor transmission lines [54] (see Figure 9). Such coils are made of two concentric windings separated by a dielectric plate, with their openings diametrically opposed in order to produce a non-zero magnetic field outside the spiral. These two windings constitute an equivalent inductance and the substrate in between the coils plays the role of a distributed capacity.



Figure 9: Split-Conductor Transmission-Line (STR)

This design has been proposed in [55].

In order to increase the inductance of these coils, so-called multi-turn split-conductor transmission-line resonators (MTLR) were described in [54]. A number of quasi-circular concentric windings, connected to each other by small steps (the effect of which is considered negligible for the calculation of the resonance frequency) constitute each coil. For this type of resonator, analytical expressions for the inductance and the impedance can be determined. The inductance is calculated as the sum of inductances of the circular loops plus the mutual inductances between parallel-plate and coplanar loops. By numerically solving the resonance condition given by

$$[\text{Eq. 45}] \quad \frac{\Lambda \omega}{4NZ_C} \tan\left(\frac{\beta L}{4N}\right) = 1$$

for ω , the resonance frequency can be predicted for a given configuration. In this equation Λ denotes the total inductance, N is the number of turns, Z_C the characteristic impedance of the circuit, β is the propagation constant of the conductor line and L is the total length of the windings. Λ and Z_C are functions of the geometric and electric properties of the coil assembly, detailed equations can be found in annex 6.1.

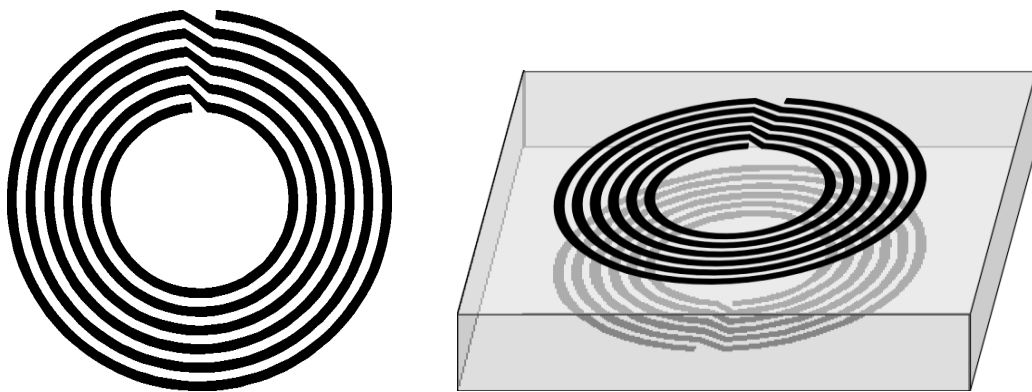


Figure 10: Multi-turn Split-Conductor Transmission-Line Resonator (MTLR)

The design was suggested by [54], here an example with 6 turns.

Left: One side of the resonator seen from the top.

Right: Both coils mounted on the (transparent) dielectric plate.

2.3.3 Connection to the receiver

The signal acquired in the RF coil has to be transmitted to the preamplifier and then to the rest of the signal detection and treatment units. There exist two different ways to achieve this, i.e. capacitive and inductive coupling.

2.3.3.1 Capacitive coupling

The conventional method to connect a coil to the receiving unit is done via a capacitive matching network. Additional capacitors have to be inserted in order to match the impedance of the resonant circuit that the coil represents to the impedance of the receiver (usually 50 Ω).

The quality factor of the coil is lowered by a factor 2 when connected and matched compared to the coil alone; this also means a doubled bandwidth. In order to keep dielectric losses small, the capacitively coupled coil has to be electrically equilibrated or “balanced”. This is achieved by symmetrical design of the matching network, such that the mass-point is situated in the middle of the coil.

Matching and tuning of the coil are usually not independent, so the final settings can only be found after several iterations of adjustment.

2.3.3.2 Inductive coupling

Another way to connect the coil to the receiver is by adding an inductively coupled coil, tuned at the same resonance frequency as the actual RF coil with a variable capacitor in series and wired directly to the receiver.

The advantage of this method is that it is intrinsically electrically equilibrated and matching and tuning of the coil can be adjusted independently. It is also possible to change the resonance frequency of the RF coil with the coupling coil, which is advantageous if the coil is e.g. implanted inside the tissue under investigation. Moreover, as the coupling coil can be placed under the patient table, and the wiring can be hidden, the use of the RF coil is much less limited because wireless. The MTLRs described in chapter 2.3.2.2 are connected in this configuration.

2.4 SKIN IMAGING

2.4.1 Anatomy and function of the skin

The skin surface sets the boundary between the body and the environment and serves three main functions. It protects against outside damage through physical, chemical and/or infection-related stress and regulates body temperature and fluid balance. To fulfill these diverse functions, the skin has three anatomic layers: the epidermis, the dermis and the subcutis, which serve independent and joint functions. Figure 12 shows a cross-section of the skin with its main layers indicated.

2.4.1.1 Epidermis

The epidermis, the outmost coating of the skin, is formed by a multilayer of keratinocytes. The epidermis is non-vascularized and separated by a basement membrane from the dermis.

2.4.1.2 Dermis

The next underlying zone, the dermis, is a highly vascularized connective tissue. The dermo-epithelial zone is not linear, but rather represents an interdigitated interface. Keratinocytes from the epidermis form the rete ridges, which protrude into the dermis. Concurrently, between these rete ridges, the dermis extends upwards and forms the papillae. Morphologically and functionally distinct from this so-called papillary dermis is the deeper portion of the dermis, the reticular dermis, which harbors eccrine and apocrine glands.

2.4.1.3 Hypodermis/Subcutis

The subcutaneous fat layer further below resides on the muscle fascia. Terminal hairs root in the fat layer; the sebaceous glands pertinent to the hair follicle reside within the dermis.

2.4.1.4 Skin vasculature

The vasculature of the skin (see Figures 11 and 12) itself has many different functions as for example thermoregulation, inflammatory responses and nutrition. Therefore, the skin vasculature is organized in a complex manner.

The largest vessels of the skin (arteries and veins) lie within the subcutis and at the dermal/subcutaneous border. They can vary in size from 0.2 mm up to several millimeters. Smaller vessels arising from the deep vascular plexus are called arterioles. The largest arterioles in the skin have an outer diameter of 50 μm and lie within the deep dermis. The thickness of their wall is between 10-16 μm . Arterioles of the superficial dermal plexus, also called terminal arterioles, have an outer diameter of 17-22 μm .

Capillaries, which can be divided into arterial and venous capillaries, have a diameter of 10-12 μm with no surrounding smooth muscle cells, their vessel wall is about 2-3 μm thick. Post-capillary venules range between 18-23 μm with a wall thickness of 3-5 μm . Venules and veins descend to the large subcutaneous veins and continuously increase in diameter and vessel size [56].

One has to bear in mind that the assessment of vessel diameters has been performed mainly by histology and that the measured vessel sizes reflect a postmortem picture of the skin vasculature, which is influenced by shrinking artifacts due to fixation and dehydration. Therefore, vessel diameters may be significantly larger if assessed by in vivo methods as, e.g., MRI microscopy.

2.4.2 MR skin imaging

Magnetic resonance offers the possibility to non-invasively produce volumetric images of the human body without using ionizing radiation. It is, therefore, an interesting choice for imaging of many anatomical regions. The skin is only a few millimeters thick and, hence, extremely high spatial resolution is required to sufficiently resolve its pertinent structures. Since such high spatial resolution is dependent on high measurement sensitivity, only small RF coils can be used for micro-imaging. For most applications, these have the disadvantage of a small field of view and penetration depth. For skin imaging this is not a restriction, however, as the skin is superficially located. Imaging of the skin, being the body's largest organ, is consequently one of the most evident applications of in vivo MR microscopy. MRI offers a variety of soft tissue contrasts and can be used to study physiological parameters of the tissues such as water content, perfusion and flow. MR imaging of the skin started to develop in the 1990s and was since then pursued by small research community, but has not yet been widely used in dermatology.

MR resolution of 1–5 μm has been reported at extremely high fields (>10 T) with microscopic samples, micro-coils (<500 μm) and long acquisition times (approximately one day) [57-61]. For in vivo imaging, the highest reported spatial resolutions so far were obtained using cryogenic probes [62] at 1.5 T and range from 60 μm isotropic in small animals [63] to 80 μm isotropic in humans [64].

Using normal conducting copper coils, several skin imaging investigations have been reported in the literature. The layered structure of the skin and anatomical features such as pilosebaceous units have been shown [65-67]. Recently a comparison of skin imaging at 1.5 T and 3 T using fat/water separation techniques was published [68]. Other studies investigated relaxation times of the different skin layers [69], hydration and ageing of the skin [70-72], and the role of MRI in melanin-containing skin tumors [73]. In addition, spectroscopic imaging of the skin [74] and a comparison of MRI to

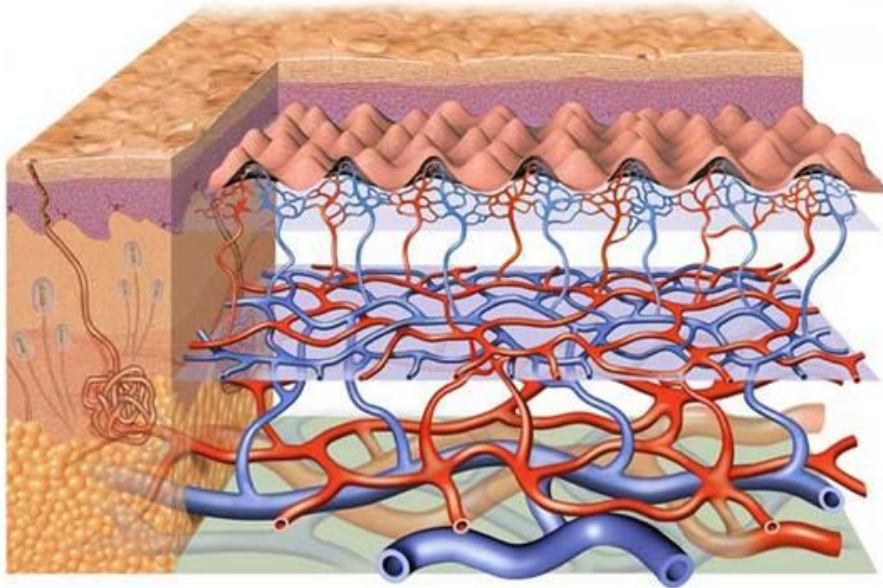


Figure 11: Schematic of skin vasculature

Venous vessels (blue) and arterial vessels (red). The superficial vascular plexus is located underneath the epidermis/dermis border, the deep vascular plexus is situated at the border of dermis and hypodermis. Larger vessels are found in the hypodermis. (from [75])

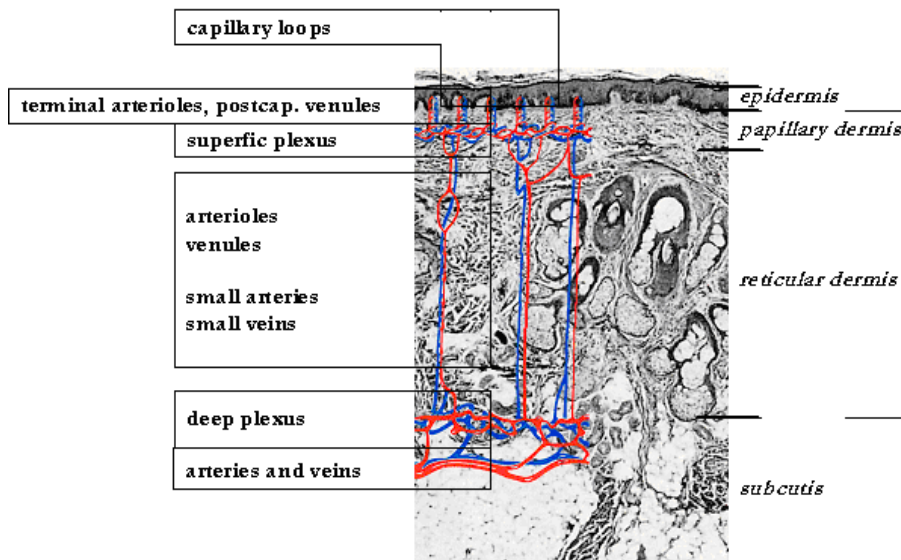


Figure 12: Organization of skin layers

Skin layers and the position of different cutaneous vessels are shown. (Figure modified from [76])

high frequency ultrasound [77] have been reported. Previous studies from our own group investigated the blood flow distribution in small arterial vessels in the human finger using a dedicated micro-imaging gradient insert at 3 T [78] as well as micro-structures in the human toe [79].

All of these studies used high in-plane resolution with much larger slice thickness (>500 μm , typically 1-2 mm), highest spatial resolution was usually applied perpendicular to the skin surface.

2.4.3 Other imaging modalities

2.4.3.1 Biopsy with subsequent histology

Cutting samples from the skin and preparation for histological assessment is the gold standard for obtaining images of the skin. Typically, samples of a few millimeters to centimeters are cut out of the patient's skin, either using a scalpel or a punch. Specimen are fixed in paraformaldehyde and paraffin-embedded. These samples are serial sectioned with slices of several μm thickness and usually stained with hematoxylin and eosin. The sections can be histologically examined under a microscope, however, no full 3 D coverage is feasible.

2.4.3.2 Photography

The simplest form of producing images of the skin is photography. This technique is widely used for monitoring of nevi.

2.4.3.3 Surface microscopy

Surface microscopy is employed to get more detailed images of the skin surface. It can be performed without or with application of oil onto the skin, which improves the image quality. This technique is also widely used for monitoring of nevi and better differentiation of malignant lesions [80].

2.4.3.4 Ultrasound

Ultrasound at a frequency of 20 MHz is used to measure skin thickness or assess skin disorders with a penetration depth of about 20 mm [81]. Resolution in axial direction is typically around 100 μm and a few hundred μm in lateral direction [82]. Ultrasound with higher frequency can achieve even higher resolution, at the cost of a reduced penetration depth, e.g. 100 MHz ultrasound has been shown down to 3.2 mm [83].

2.4.3.5 Optical coherence tomography

OCT provides axial resolution of 2-15 μm and can assess structures down to a depth of 1-2 mm. The morphology of the tissues can be imaged [84], the technique has been used for imaging of both healthy and pathologic skin [85-87].

2.4.3.6 Confocal reflectance microscopy

The resolution obtained with confocal reflectance microscopy in vivo is comparable to histology. The field of view and the penetration depth are however very limited (a few hundred μm) [88, 89].

2.4.3.7 Laser Doppler perfusion

Blood flow measurements in skin lesions have been performed [82] with this technique, providing a penetration depth of about 200 μm .

In conclusion, the higher the spatial resolution, the lower the volume coverage. Also, sensitivity and contrast is rather different among these techniques, due to different underlying physical principles. The method to be chosen for a particular application strongly depends on availability, location, target structure and function.

2.5 CUTANEOUS VASCULITIS

2.5.1 Introduction

There are only few diseases in clinical medicine that cause as much diagnostic and also therapeutic difficulties as vasculitis. Vasculitis means, per definition, inflammation and necrosis of blood vessels. Inflammation of the vessel wall may lead to the obstruction of the vascular lumen and finally to destruction of preexistent vascular structures. This cascade of events may cause ischemia and infarction.

Vasculitis is either a primary process (without any known cause or trigger) or a secondary phenomenon. As a symptom, vasculitis can be associated with infections, systemic diseases, drug uptake or can be caused by local factors. Reflecting these various causative mechanisms, also the clinical appearance of cutaneous vasculitis may be manifold. Clinical signs include purpura, palpable purpuric papules, erythema, ulcer, infarction and so-called livedo reticularis (Figure 13).

Histological confirmation is required for all of the vasculitic diseases, because clinical, laboratory or other diagnostic features are usually not sufficient to put a diagnosis reliably. On the other hand, the diagnosis made by histology must always be correlated with other diagnostic findings (clinical, laboratory, angiographic, etc.) since the same histological features may be present in different disorders [56].

2.5.2 Classification schemes

Many efforts have been undertaken to find a satisfactory classification for vasculitis but every classification harbors diagnostic difficulties and pitfalls. There are many different criteria for classifying vasculitis, regardless of the organs involved, according to

- pathogenesis (although the cause often remains unknown)
- anatomy, i.e. the localization of the symptoms; whether the disease is restricted to the skin or whether it is a systemic disease; vessel size and whether arterial or venous vessels are involved
- histological pattern (leucocytoclastic necrotizing, lymphocytic, granulomatous)
- clinical appearance (necrotizing, urticarial, purpuric,...).

The commonly used classification systems for vasculitides, the Chapel Hill Consensus Conference Criteria and the American College of Rheumatology Criteria (ACR), both use a mixture of these criteria, but both classification systems show major drawbacks. For example, disorders can be classified into different categories, depending on the classification used. More importantly, due to the criteria applied, both classifications may fail to identify patients with potentially life threatening vasculitic diseases.

These classification models fail even more in classifying cutaneous vasculitis (either vasculitis restricted to the skin or skin involvement as part of systemic vasculitis. One general criterion for classification of vasculitis is the size of the affected vessels; both classification models divide vasculitis into small and large vessel vasculitis. Although, in principal, both types of vasculitis may be found in the skin, the situation in cutaneous vessels is even more complicated since skin vessels involved can be

- the post-capillary venules of the superficial dermis
- the medium sized arterioles vessels of the deep dermis/subcutis
- the large sized arteries of the deep dermis/subcutis
- the medium sized venules vessels of the deep dermis/subcutis
- the large sized veins vessels of the deep dermis/subcutis

Additionally, the composition and distribution of the inflammatory infiltrate is also very important in the classification of cutaneous involvement in vasculitic diseases.

2.5.3 Description of different vasculitides

While small vessel vasculitis usually affects post-capillary venules in the papillary dermis, large vessel vasculitis affects the larger parts of the vasculature [90]. Since the very small venules and arterioles involved in small vessel vasculitis seem too small for MR microscopy, we will focus on large vessel vasculitis in the following. Members of this group are polyarteriitis nodosa (PAN), Wegener's granulomatosis (WG), Churg-Strauss syndrome (C-SS) and Kawasaki disease (KD). Figure 13 shows some images of characteristic clinical appearance of cutaneous vasculitis.

Although almost all of these disorders represent systemic diseases, skin involvement is a hallmark of these diseases. Therefore, the diagnosis can usually be made from a skin biopsy, if this biopsy accomplishes the diagnostic criteria. Interestingly, within these disorders, the distribution of the affected vessels varies among anatomical sites (papillary and/or reticular dermis, subcutis) and especially the affection of arteries and veins varies significantly.

The classical form of PAN represents a multisystem disease and manifests usually with uncharacteristic symptoms. It has a bad prognosis with high mortality due to involvement of the kidneys, gastro-intestinal tract, heart as well as central and peripheral nervous tissue (5 years survival < 50%). WG, C-SS and KD are less frequent. They are all characterized by leucocytoclastic or granulomatous vasculitis affecting vessels in different organs [91].

These conditions usually have to be treated very aggressively to reduce or prevent permanent damage to internal organs such as the coronary arteries, the lungs or the kidneys. Therefore, reliable early diagnosis is mandatory.

Histologically, large-vessel vasculitis takes the form of either phlebitis or arteriitis. Phlebitis shows the same histo-pathological pattern, regardless of its cause, while arteriitis may manifest in at least two different ways: in one, the infiltrate of inflammatory cells is confined to large vessels only (PAN); in the other, the cellular infiltrate is not restricted to the region of large vessels but is also distributed in patchy fashion throughout fat lobules (nodular vasculitis).

Granulomatous vasculitis is seen in vessels positioned deep in the reticular dermis and the subcutaneous fat of WG or C-SS [76]. By now, there is the observation that the involvement of arteries or veins depends on the particular disorder. Also, the involvement of vessels with different sizes varies according to the underlying disorder. Therefore, it is tempting to speculate that the affection of arteries or veins and the involvement of vessels with different sizes do not occur by chance.

Identifying the correct diagnosis for cutaneous vasculitic diseases may even more complicated by the existence of another group of vascular disorders, the so called micro-vascular occlusion syndromes, that often mimic real vasculitic disease. Among this group, especially the so called livedo-syndromes (antiphospholipid syndrome, Sneddon's syndrome, livedo-vasculitis, thrombangiitis obliterans), characterized by a specific perfusion pattern of the skin surface, are common simulators of cutaneous vasculitis.

Antiphospholipid syndrome is a systemic disease caused by the presence of circulating antiphospholipid antibodies. It is characterized by thrombosis in arteries and veins throughout the whole body, therefore potentially life threatening. Also, diagnosis of Sneddon's syndrome, a rare condition of an association of cutaneous thrombotic lesions, circulating antiphospholipid, hypertension and cerebrovascular disease is very difficult, even by histology. The sensitivity of an average 1-2 cm single biopsy is 27%, 53% with two and only 80% with three consecutive biopsies [92, 93]. Also, septic vasculitis (usually bacterial or fungal), a life threatening disease, and characterized by infectious thrombi within lumina of post-capillary venules and larger venules belongs into the group of micro-vascular occlusion syndromes. Septic vasculitis clearly shows how important it is to find a diagnosis as soon as possible.

2.5.4 Need for new diagnostic modalities

As mentioned above, diagnosis of cutaneous vasculitis (regardless of the underlying cause) may be difficult and often requires different, often time consuming diagnostic procedures. By now, the gold standard for diagnosis is histology. Histology for the diagnosis of vasculitis consists of a deep biopsy with subsequent serial-sectioning and histological examination. The reasons why it is often difficult to quickly find a diagnosis are multiple. An inadequate biopsy technique (too small, not deep enough) is a frequent but not the most common reason. Often, multiple skin biopsies are required because

- the histo-pathological findings in the biopsy specimens do not match the criteria required for exact diagnosis,
- diagnostic criteria are hard to find in a given biopsy specimen because of a discontinuous involvement of vessels,
- lesions may look distinctly different depending on their age [76].

It is especially important in vascular conditions where danger to life and limb makes timely decisions critical, to find a reliable diagnosis within appropriate time. Patients may suffer from serious systemic complications involving brain, heart, bowel, or kidneys, if it takes too long to find the correct diagnosis which is needed for starting a specific therapy. Therefore, establishment of a novel examination method that accelerates diagnostic procedures and improves the reliability of a given diagnosis by adding additional information is urgently needed and is one of the main goals of this work.



Figure 13: Clinical appearance of cutaneous vasculitis

- A) livedo reticularis
- B) panarteriitis nodosa (PAN)
- C) necrotizing vasculitis
- D) Wegener's granulomatosis (WG)

3 **EXPERIMENTAL STUDIES**

3.1 STUDY I: 12 MM HTS SURFACE COIL AT 1.5 TESLA

3.1.1 Purpose

The aim of this study was to exploit the high sensitivity of a miniaturized 12 mm surface coil even at the clinical standard field strength of 1.5 T for imaging of the skin and its vasculature in vivo. For such small coils, if made of copper, intrinsic coil noise would severely degrade image SNR. Therefore the limits of in vivo resolution in a whole-body 1.5 T scanner were explored by employing a superconducting surface coil providing ultra-low intrinsic noise.

3.1.2 Materials and Methods

3.1.2.1 MR scanner

Measurements were performed on a Philips Achieva whole-body scanner (Philips, Best, The Netherlands) with a main magnetic field strength of 1.5 T, located at the CIERM (Centre Inter-Etablissements de Résonance Magnétique) at the Hospital of Le Kremlin-Bicêtre, Paris, France.

It is equipped with a gradient hardware upgrade providing a maximum gradient strength of 66 mT/m. A home-made interface connector was used to connect custom coils via a BNC plug to the manufacturer's standard coil plug next to the magnet bore.

3.1.2.2 Network analyzers

An HP 4195A network analyzer (Hewlett-Packard Company, Palo Alto, CA, U.S.A.) at the CIERM in Le Kremlin-Bicêtre, France was used for verification of tuning and matching of the superconducting surface coil immediately before measurements in the 1.5 T Philips scanner.



Figure 14: Philips Achieva 1.5 T Scanner
The scanner at CIERM is equipped with a gradient system with maximum gradient strength of 66 mT/m.

An Agilent E5061A network analyzer (Agilent Technologies, Palo Alto, CA, U.S.A.) at U2R2M in Orsay, France was mainly used for pre-tuning and testing of the superconducting surface coils on table before transferring the coil to the measurement site at Le Kremlin-Bicêtre. Also it served for tuning and matching of the 6 mm surface coil for the first 7 T imaging tests (see chapter 3.3).

3.1.2.3 RF coils

3.1.2.3.1 Coil design

The geometry of the superconducting coil is based on the MTLR principle (multi-turn transmission line resonator, cf. section 2.3.2.2.2). The actual coil dimensions were calculated using a semi-empirical analytical model, which takes into account the following parameters (illustrated in Figure 15):

- Number of turns of the spiral N
- Outer diameter of the coil d_{ext}
- Opening angle α of the gap
- Width of the conductor line w
- Spacing between to neighboring turns sp
- Dielectric constant of the support material ϵ
- Thickness of the support material h

Since the mathematical model only predicts the resonance frequency for a given choice of geometrical parameters (see annex 6.1), a set of calculations for various parameter configurations has been performed in MATLAB. A dedicated toolbox has been developed, the software documentation is given in annex 6.2.

For each parameter, a wide range of values was calculated and the corresponding resonance frequency result was stored in a database. Once the values were computed, geometries for a given resonance frequency of interest could be filtered from the database. The parameter sets best suiting the desired coil size and resonance frequency were then chosen from result files. Results from previously manufactured coils of this design were used to correct for systematic bias of the measured resonance frequency to the calculated value in order to achieve the correct frequency after fabrication.

3.1.2.3.2 Mask creation

The simulation results were used to automatically draw a mask of the desired coil using CorelDraw 7.373 (Corel Corporation, Ottawa, Canada) using Corel SCRIPT. The mask was used for the fabrication process.

3.1.2.3.3 Coil production

The superconducting MTLRs were manufactured by THEVA Dünnschicht-Technik GmbH, Ismaning, Germany.

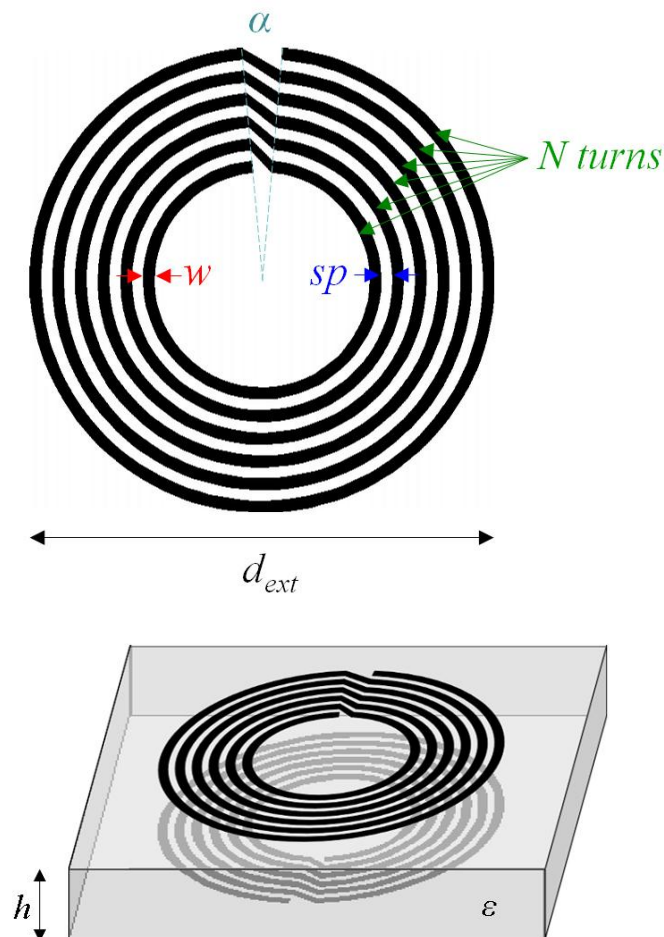


Figure 15: Parameters in the semi-empirical analytical calculation
The parameters indicated are required for the calculation of the coil's resonance frequency.

3.1.2.3.4 Coil characterization

An RF analyzer, a directional coupler and a probe are used for on-table measurements. Figure 16 shows a schematic of the measurement setup following the method suggested in [94] using an inductively coupled probe to pick up the signal from the RF coil. The equivalent circuits as seen from the probe coil and the RF coil are represented in the center and bottom images.

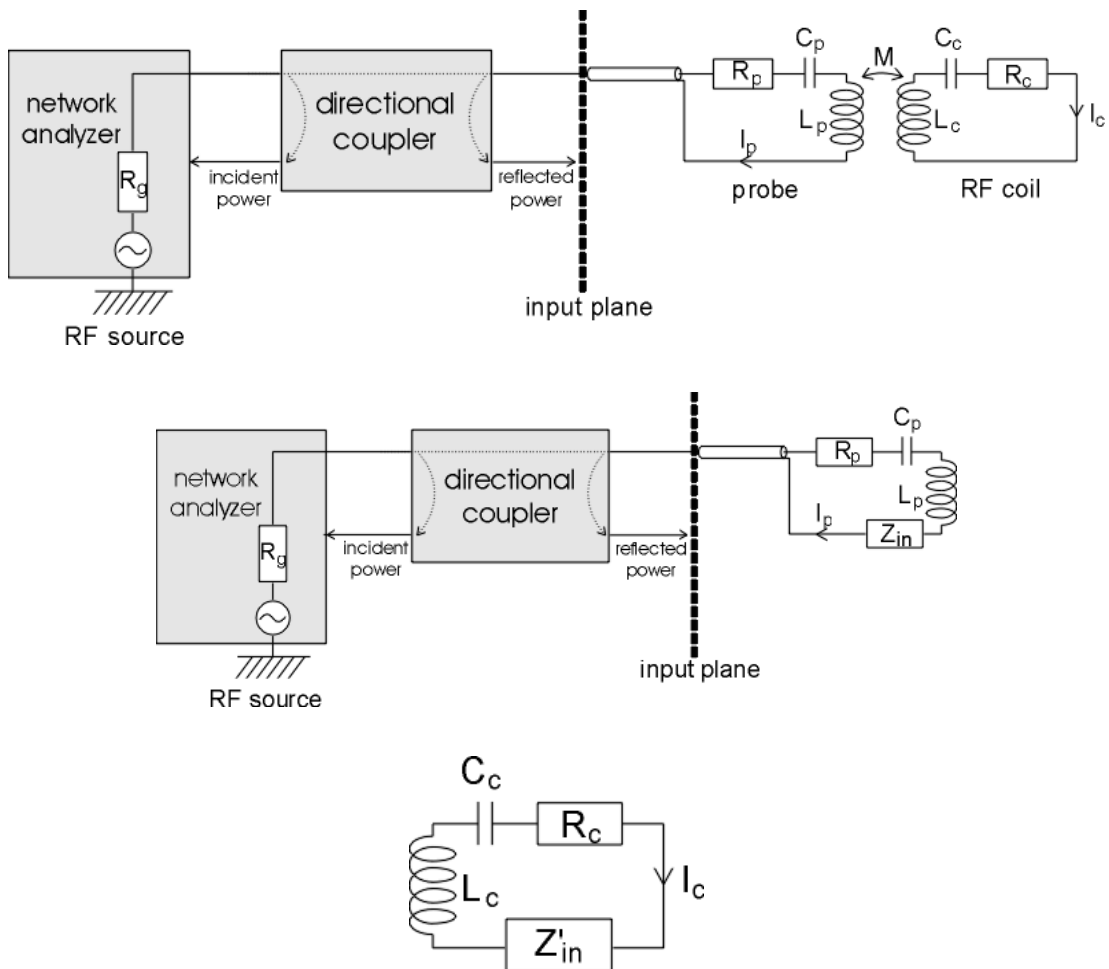


Figure 16: Measurement setup using a directional coupler

Top: The RF coil is related to the rest of the setup via a mutual inductance M with the probe.

Center: Equivalent circuit as seen from the probe. Z_{in} represents the induced impedance of the RF coil in probe.

Bottom: Equivalent circuit as seen from the RF coil. Z'_{in} represents the induced impedance of the remaining circuit in the RF coil.

3.1.2.3.4.1 Electrical quality factor Q

From the ratio of the square roots of the reflected and incident power the reflection coefficient ρ can be defined as follows

$$[\text{Eq. 46}] \quad \rho = \sqrt{\frac{P_{refl}}{P_{inc}}} = \frac{(Z_p + Z_{in}) - Z_g}{(Z_p + Z_{in}) + Z_g}$$

where Z_p and Z_g represent the impedance of the probe and the output of RF source, respectively, Z_{in} is the induced impedance of the RF coil in the probe (see Figure 16). Z_{in} can be deduced from a measurement of ρ without the RF coil present, i.e. the mutual inductance M between probe and RF coil and consequently Z_{in} equal zero, which gives the reference reflection coefficient ρ_0 . The compensated reflection coefficient ρ_{comp} is calculated by complex subtraction

$$[\text{Eq. 47}] \quad \rho_{comp} = \rho - \rho_0$$

In the measurement $\rho_{comp}(\omega_0) = \rho_{comp0}$ is given by

$$[\text{Eq. 48}] \quad \rho_{comp}(\omega_0) = \rho_{comp0} = 10^{\frac{T/R_{comp}(\omega_0) + 2A}{20}}$$

where A is the attenuation in dB between the input plane of the measurement and the probe and T/R_{comp} is the ratio of the transmitted to reflected signal measured by the network analyzer.

Typical curves for the real and imaginary parts of T/R_{comp} in dB over a frequency range around the resonance frequency are shown in Figure 17. For copper coils in general, and superconducting coils at low incident power levels, the quality factor is measured with the so-called bandwidth method. At first a frequency sweep without the RF coil is performed to obtain ρ_0 . Another measurement with the RF coil positioned next to the probe is done for a measurement of ρ . The electrical quality factor Q_c is then obtained by

measuring the frequency interval $\Delta\omega$ for which $T/R_{comp} = T/R_{comp,max} - 3dB$ holds. The measured quality factor Q_{meas} is then derived from equation

$$[\text{Eq. 49}] \quad Q_{meas} = \frac{\omega_0}{\Delta\omega}$$

The intrinsic quality factor Q_c of the RF coil without the influence of the probe is extracted with

$$[\text{Eq. 50}] \quad Q_c = \frac{Q_{meas}}{1 - \rho_{comp}}$$

This method is only applicable if a linear relationship between RF power and coil response exists. This is achieved for copper coils, while superconducting coils show strong non-linearity effects in the domain of high RF powers. Therefore, a slightly modified technique has to be applied [95, 96].

The first step of the modified measurement for superconducting RF coils at high power level is the same as for copper coils. The measurement of Q_c at low power level according to equations [Eq. 49] and [Eq. 50] is performed and R_{in0} is derived from eq. [Eq. 47] as follows: for a matched coil ($R_g = R_p = R$) at resonance ($Z_p \rightarrow R_p, Z_{in} \rightarrow R_{in0}$), the induced resistance of the RF coil in the probe $R_{in}(\omega_0) = R_{in0}$ becomes

$$[\text{Eq. 51}] \quad R_{in0} = 2R \cdot \frac{\rho_{comp}}{1 - \rho_{comp}}$$

The pair of parameters Q_c and R_{in0} will be used as reference values Q_{cREF} and R_{in0REF} in the second step of the measurement. The set-up of the measurement stays the same, only that this time a power sweep at the resonance frequency is performed instead of a frequency sweep. Again, the values of ρ_{comp0} and R_{in0} are calculated from the same equations as previously. As the distance of the RF coil to the probe has not been changed, the mutual inductance M and hence the

coupling coefficient k do not change, and so the quality factor of the coil at a given power level can be written as

$$[\text{Eq. 52}] \quad Q_c = Q_{cREF} \cdot \frac{R_{in0}}{R_{in0REF}}$$

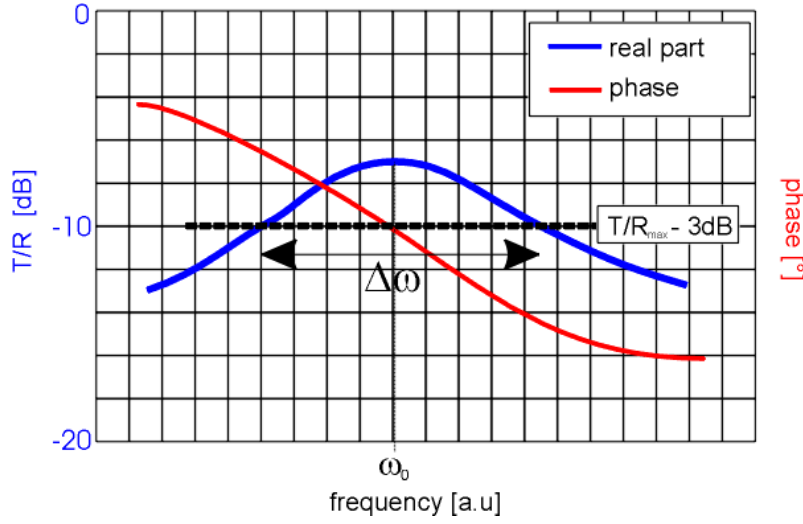


Figure 17: Typical curves for compensated T/R over frequency

The real part of the curve exhibits a maximum at the position of the resonance frequency. At that frequency, the phase is zero. The full width at half maximum, i.e. T/R at 3dB below maximum is used for the calculation of the quality factor Q .

3.1.2.3.4.2 Resonance frequency ω_0

The resonance frequency is directly obtained from the measurement of the quality factor during the frequency sweep from the position of the maximum of T/R_{comp} .

If the measured resonance frequency is higher than the desired value (the theoretical value of the resonance frequency of the nuclei at the given field strength), additional small pieces of dielectric material will be placed on the coil, thus, decreasing the frequency. As in the numerical calculation of the coil dimensions prior to the fabrication, a slightly higher value of ω_0 is yielded; corrections will only have to be done in the sense of lowering the frequency. If

the frequency is too low however, positioning of a small copper ring near the RF coil increases it by weak inductive coupling between the two structures. This is not desirable because if the frequency has to be increased a lot, the tuning coil has to be placed very near to the RF coil, decreasing its quality factor essentially.

3.1.2.4 Experimental setup

Before MR measurements can be performed, the HTS coil has to be positioned in the cryostat and the correct resonance frequency has to be adjusted. When using a new HTS coil in the cryostat, this is a time-consuming iterative process. Figure 18 shows how the HTS coil is positioned in the cryostat.

To place an HTS coil in the cryostat, the vacuum chamber, i.e. the head compartment of the cryostat containing the coil end of the cold finger has to be demounted. Then the HTS coil is placed on the circular end of the cold finger. This cold finger made of sapphire thermally connects the HTS coil to the liquid nitrogen reservoir.

Dielectric pads made of Teflon® are placed in the center on top of the coil. Then a strip of Kapton® is wrapped vertically around the coil and the cold finger. The dielectric pads in the coil's center increase the pressure of the Kapton® stripes onto the coil and ensure sufficient thermal contact between the coil substrate and the cold finger. The pressure is further increased by tightly wrapping more Kapton® strips horizontally around the vertically aligned stripes.

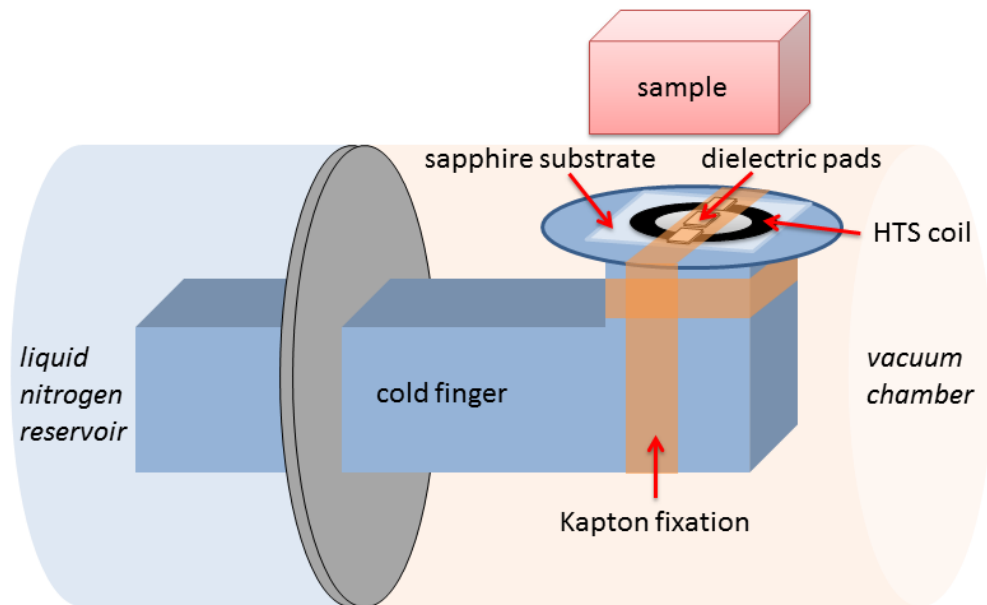


Figure 18: HTS coil mounting in the cryostat

The drawing illustrates the positioning of the HTS coil on the cold finger within the vacuum chamber of the cryostat. For detailed explanation see the text.

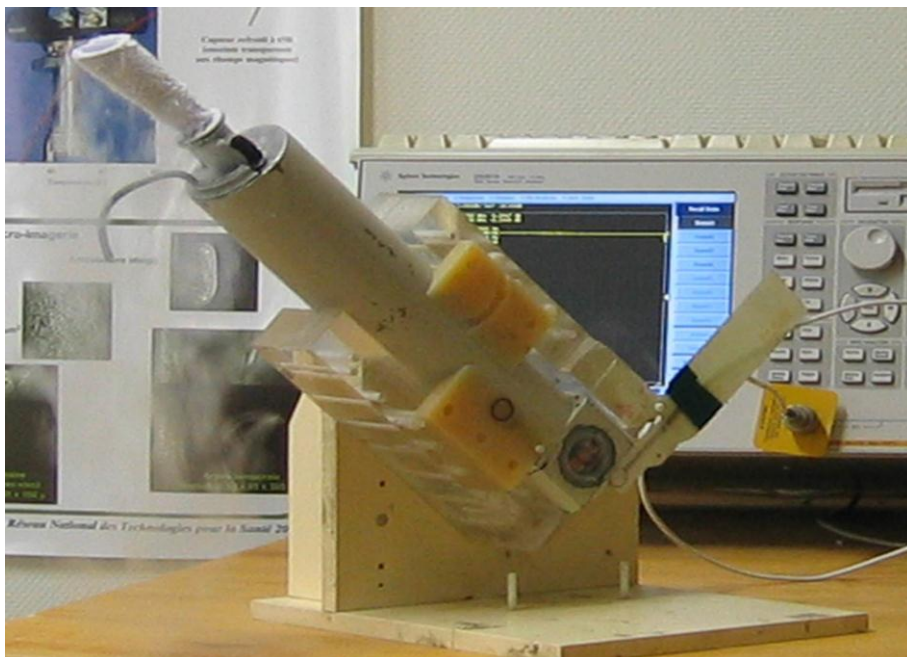


Figure 19: The cryostat for the HTS coil

The cryostat is the cylinder mounted on a PVC rack. It is cooled by filling liquid nitrogen through a paper cone in the opening on top after the chamber containing the HTS coil has been evacuated using a vacuum pump.

The vacuum chamber is subsequently closed and tightened with plastic screws. The position of the rubber fitting has to be checked to ensure tightness. The cryostat is now connected to a vacuum pump until the pressure within the vacuum chamber reaches a stable value, this step usually takes about 1-2 hours. A paper cone is formed to fit into the opening of the liquid nitrogen reservoir and liquid nitrogen is slowly poured (see Figure 19), which takes about 45 min. By using the network analyzer, the moment of the transition to the superconducting state of the coil can be seen, as the resonance only develops when the HTS coil is superconducting.

Now the resonance frequency of the coil is determined. If it is higher than the desired Larmor frequency, the reservoir is emptied, and the assembly is set aside to warm up back to room temperature. The vacuum is broken and the vacuum chamber is demounted again. Additional dielectric Teflon® pads can be placed on the coil windings under the Kapton® strips. This has the effect of lowering the resonance frequency by increasing the capacitance of the coil. The whole procedure is repeated, until the resonance frequency is only a few kHz away from (below) the Larmor frequency.

The remaining frequency mismatch can be taken care of by approaching a ring of copper, which increases the resonance frequency by weak inductive coupling. It contributes noise to the circuit, therefore careful pre-tuning with dielectric pads should be performed to minimize the need for tuning with the copper ring.

The photograph in Figure 20 shows the arrangement used for imaging at 1.5 T. The white cylindrical tube is the cryostat filled with liquid nitrogen. The HTS coil (dark circle) is visible in its evacuated housing behind a sapphire window. The dielectric plates for pre-tuning of the coil are visible on top of the coil (white patches). They are attached to the coil and the cold finger using Kapton® film (orange stripe).

The HTS coil is inductively coupled to a pick-up coil (probe coil); matching to 50Ω is achieved by varying the relative distance of the pick-up coil to the HTS coil. The copper ring on the left is used for fine tuning of the resonance frequency by adjustment of the distance to the HTS coil.

The pick-up coil is connected to the Philips scanner by a hand-made adapter to the manufacturer's coil plug.

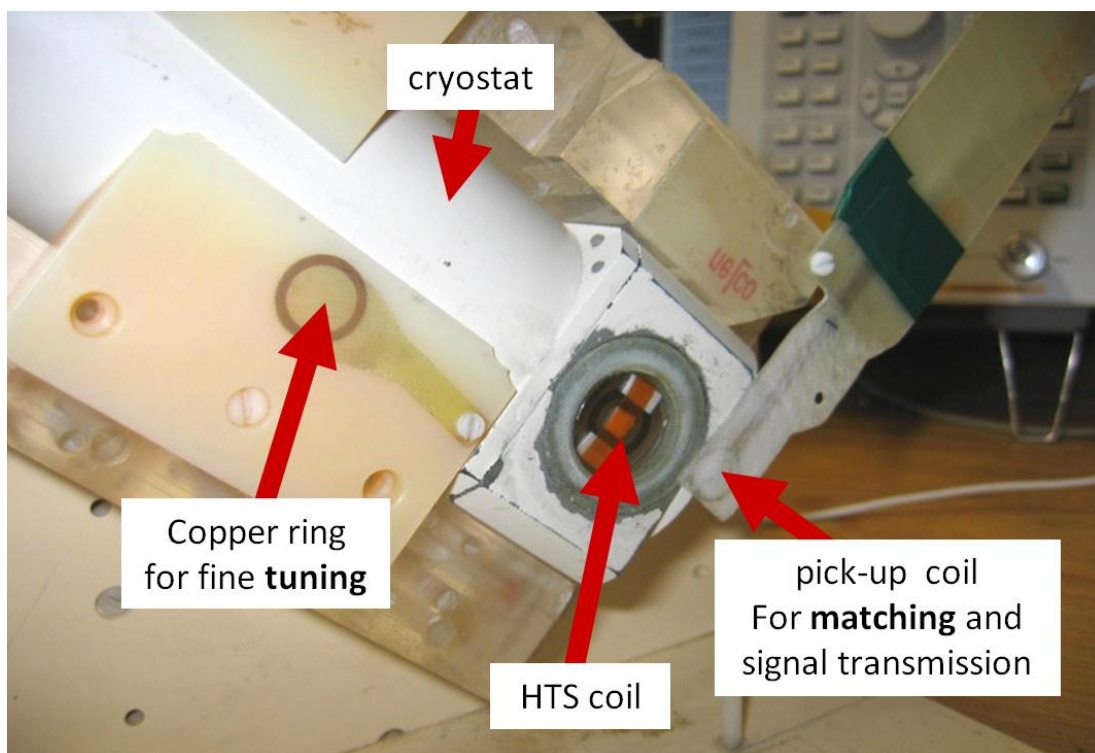


Figure 20: Experimental setup with superconducting surface coil at 1.5 T
The HTS coil is visible through a sapphire window and can be placed at less than 2 mm distance from the sample. A copper ring for fine tuning of the resonance frequency and a pick-up coil for matching and signal transmission to the receiver are mounted on the cryostat. Their respective positions to the HTS coil can be adjusted manually by rotation.

3.1.2.5 Evaluation of loss contributions

The quality factor Q of the superconducting coil was measured in different situations, i.e. unloaded and loaded by the sample, outside and inside of the magnetic field, in order to quantify the individual contributions of the following entities to total losses:

- imperfections in the superconducting material itself,
- additional losses introduced by normal-conducting flux vortices in the superconductor when exposed to a magnetic field,
- and the copper ring used for fine-tuning of the HTS coil.

With known inductivity L from the semi-analytical expressions used for calculation of the coil geometry (see annex 6.1), the losses can be calculated from [Eq. 35] by measuring the quality factor.

For the contributions of the fine-tuning copper ring, the Q values of the HTS coil for a range of detuning values from 0 to 76 kHz achieved by varying the distance of the ring to the HTS coil have been assessed. The impact of these losses on SNR can be estimated using [Eq. 37] by taking the reciprocal value of the square root of temperature-weighted losses.

3.1.2.6 MR sequences

Three different types of imaging experiments were performed within the study. The first experiment aimed at very high in-plane resolution perpendicular to the skin surface to clearly depict the layered structure of the skin. In the second and third experiment, isotropic resolution was chosen in order to obtain three-dimensional information about the architecture of the vascular tree in the skin.

All experiments have in common, that a 3D gradient echo sequence was used. Figure 21 shows the orientation of the read-out and phase encoding directions for the second and third experiment.

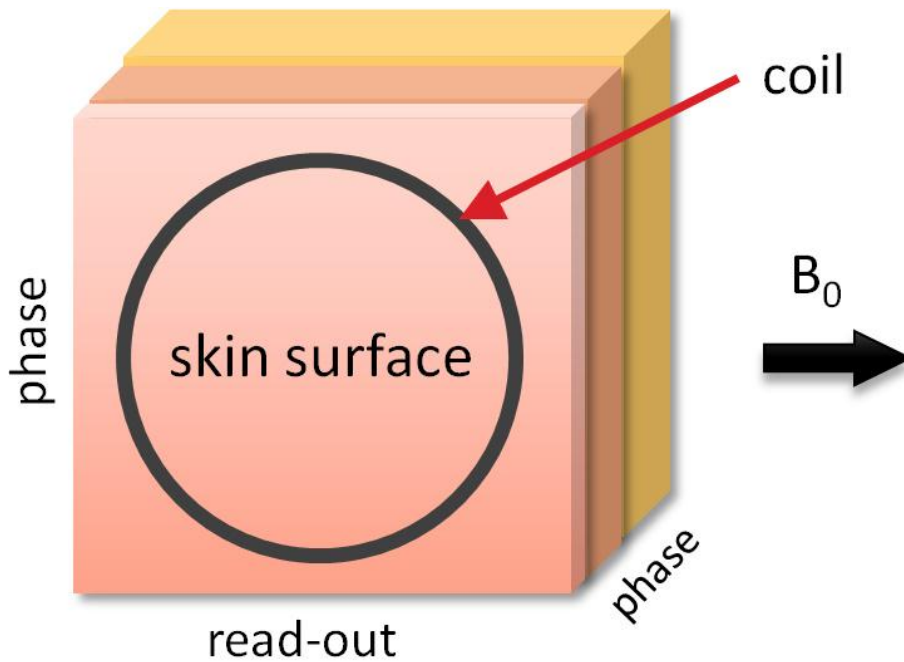


Figure 21: Positioning of the coil and read/phase directions

The coil was placed adjacent to the calf in vertical position. See the text for a detailed reasoning for this configuration.

In the anisotropic case of experiment 1, read-out direction was perpendicular to the skin surface, because the highest spatial resolution was also chosen in that direction. The field of view was chosen such that the sensitive area of the coil was fully covered to avoid fold-over artifacts. For the isotropic acquisitions, the direction “entering” the skin perpendicularly was chosen as one of the two phase encoding directions, because due to the rapid decrease in signal intensity with distance to the coil, the field of view could be reduced in that direction, reducing the number of phase encoding steps and, thus, measurement time.

The coil was vertically positioned in the cryostat and the plane of its windings was parallel to the static main magnetic field, since only the component perpendicular to \vec{B}_0 of the RF field created by the coil contributes to excitation of the spins.

The choice of sequence parameters, summarized in Table 2, was a compromise to best achieve the following goals:

- highest possible spatial resolution
- measurement time \approx 10 min
- shortest possible echo time

Experiment 3 has voxel volumes half as big as those of the other two experiments, therefore the scan was repeated three times in order to regain SNR by averaging after realignment (see section 4.1.2).

	Experiment 1	Experiment 2	Experiment 3
TR [ms]	146	32	38
TE [ms]	16	8.4	9.9
FOV [mm ³]	20.5 x 20.5 x 10.5	25.6 x 12.8 x 15	10 x 10 x 10
Matrix	1024 x 326 x 14	256 x 128 x 150	124 x 124 x 125
Res [μ m ³]	20 x 60 x 750	100 x 100 x 100	80 x 80 x 80
Vol [nL]	0.9	1	0.51
BW [Hz/Px]	35	35	72
WF-shift [Px]	6	6	3
Time [min]	11:06	13:07	9:52

Table 2: Sequence parameters for the 1.5 T experiments

TR = repetition time, TE = echo time, FOV = field of view, Res = spatial resolution, Vol = voxel volume, BW = read-out bandwidth per pixel, WF-shift = shift between water and fat.

For imaging, the Ernst angle was used, which was estimated by measuring a series of images with different flip angles and searching the image with maximum SNR, with all other imaging parameters kept constant.

The excitation pulse is transmitted by inductive coupling of the HTS coil with the body coil, concentrating the B_1 -field near the HTS coil in consequence. This has to be accounted for in the choice of the flip angle on the console. A

software patch was created in order to emit excitation pulses with flip angles below 1° .

For reception, because of the weak coupling to the body coil which would lead to an unfavorable noise factor [97], the HTS coil is inductively coupled to the previously described pick-up coil.

Because of the coil's high sensitivity, even small noise contributions of the reception chain affect image SNR, so the standard preamplifier was replaced by a special low-noise preamplifier with a noise figure of 0.6 dB.

3.1.3 Results

Results from experiments 1 and 2 were presented in [98], experiment 3 was presented in [64]. In a related study of our group, the same superconducting coil has been used to demonstrate even higher isotropic resolution in a phantom [99].

3.1.3.1 RF coils

3.1.3.1.1 Design

Using the MATLAB Toolbox described in annex 6.2, the following geometry for an MTLR resonating at the Larmor frequency for protons at 1.5 T was obtained: The substrate used was sapphire with a thickness h of 330 μm and a dielectric constant ε of 10.0556. The outer diameter of the coil d_{ext} was 14.6 mm. The coil had $N = 6$ turns, with a width of the conductor line w of 240 μm and a spacing between to neighboring turns sp of 180 μm . The mean diameter of the coil was therefore ≈ 12 mm.

3.1.3.1.2 Quality factor

The coil quality factor was evaluated in unloaded and loaded condition, outside and inside the magnetic field. Table 3 summarizes the results.

Condition	Q (mean \pm SD)
Unloaded, outside magnetic field	100.000 \pm 12.000
Unloaded, in magnetic field	8.600 \pm 900
Loaded by calf, in magnetic field	1.500 - 2.500, depending on subject

Table 3: Quality factor of the HTS coil under different conditions
Loaded quality factors are given for a typical load in the imaging experiment, i.e. a human calf positioned at the sapphire window next to the HTS coil.

3.1.3.2 Images

All three experiments showed very satisfactory results in terms of good image SNR and contrast between the different cutaneous layers.

Figure 22 shows the result of experiment 1, the part of the image containing no signal was cropped for display reasons. A clear distinction can be made between the skin layers. The epidermis appears as a hyper-intense thin horizontal line on top. The dermis underneath is slightly hypo-intense, mainly due to the short $T2^*$ of the connective tissue and shows a heterogeneous pattern. In the hypodermis, the fat lobules can be identified. Apart from the septae, the appearance of the subcutaneous fat is more homogeneous and shows higher signal than the dermis.

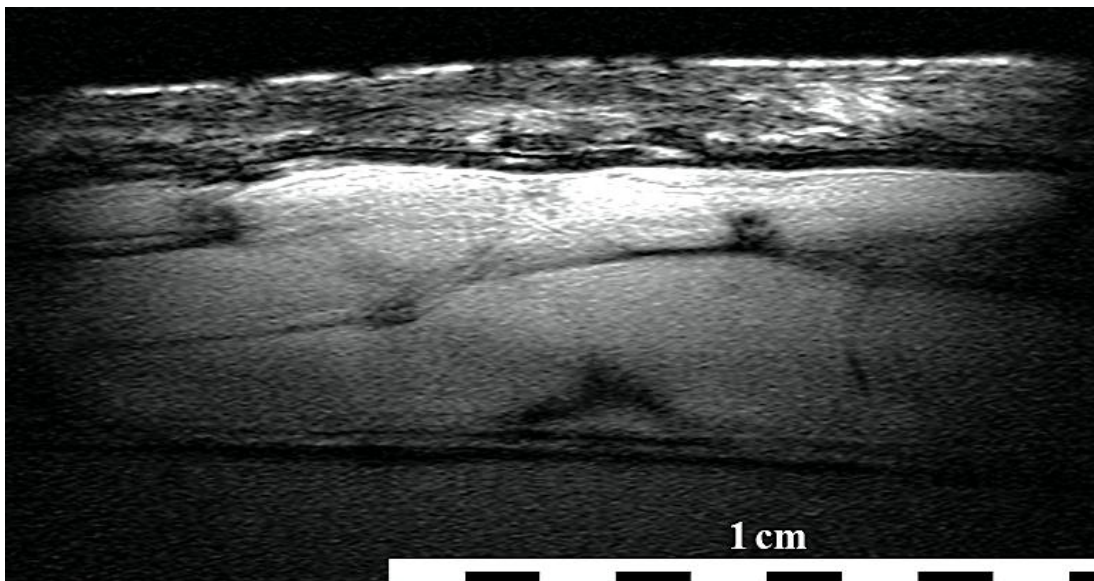


Figure 22: Skin image with HTS coil, 20 x 60 μm in-plane resolution

Result of experiment 1 with anisotropic resolution. The highest spatial resolution is perpendicular to the skin's surface (here: vertical). The slice thickness is 750 μm .

The three skin layers epidermis (top, hyper-intense), dermis (middle, hypo-intense), and hypodermis (bottom) are very well distinguished, fat lobules in the hypodermis can be seen. Due to the chemical shift between water and fat in read-out direction, the hypodermis is shifted away from the dermis.

Figure 23 shows exemplary images from experiment 2 using 100 μm isotropic resolution. The top image displaying an axial slice perpendicular to the skin surface features an axial cut through a larger vessel embedded in the adipose tissue of the hypodermis. Its diameter is approximately 2 mm.

Interestingly, the vessel wall of this large vessel can be differentiated from its lumen. A smaller vessel of about 400 μm in diameter connecting the large vessel to the deep vascular plexus is also seen in the image. Because of the horizontal read-out direction and the low read-out bandwidth, the vasculature (containing mostly water) is shifted with respect to the surrounding fatty tissue. This fact must be known to the observer, because the 3D-like appearance or shadow might be easily misinterpreted by the radiologist.

The bottom image of Figure 23 shows a sagittal slice containing some of the vessels within the deep vascular plexus at the border of dermis and hypodermis. To the right side of the image, an oblique cut through dermis and epidermis is observed; this is due to the curved surface of the calf, as seen in the top image.

Figure 25 shows four slices with exquisite detail in different depths of the skin as measured with the protocol of experiment 3 at an isotropic spatial resolution of 80 μm .

The first slice on the top left of the figure is located at the surface of the skin. It displays the well-known rhombic structure of the *areolae cutaneae* of hairy skin (as opposed to hair-less skin on hand palms, foot soles etc.). Some hypo-intense spots corresponding to the positions where hair penetrates through the skin surface can also be seen.

The top right slice shows pilosebaceous units, i.e. hair follicles appearing as hyper-intense round shapes at a depth of ≈ 700 μm below the skin surface. The hypo-intense linear structures inside the hair follicles are hairs. Comparing this slice to the first one, it can be seen that the position of the holes where hairs penetrate the skin surface correspond very well to the positions of the hair follicles underneath.

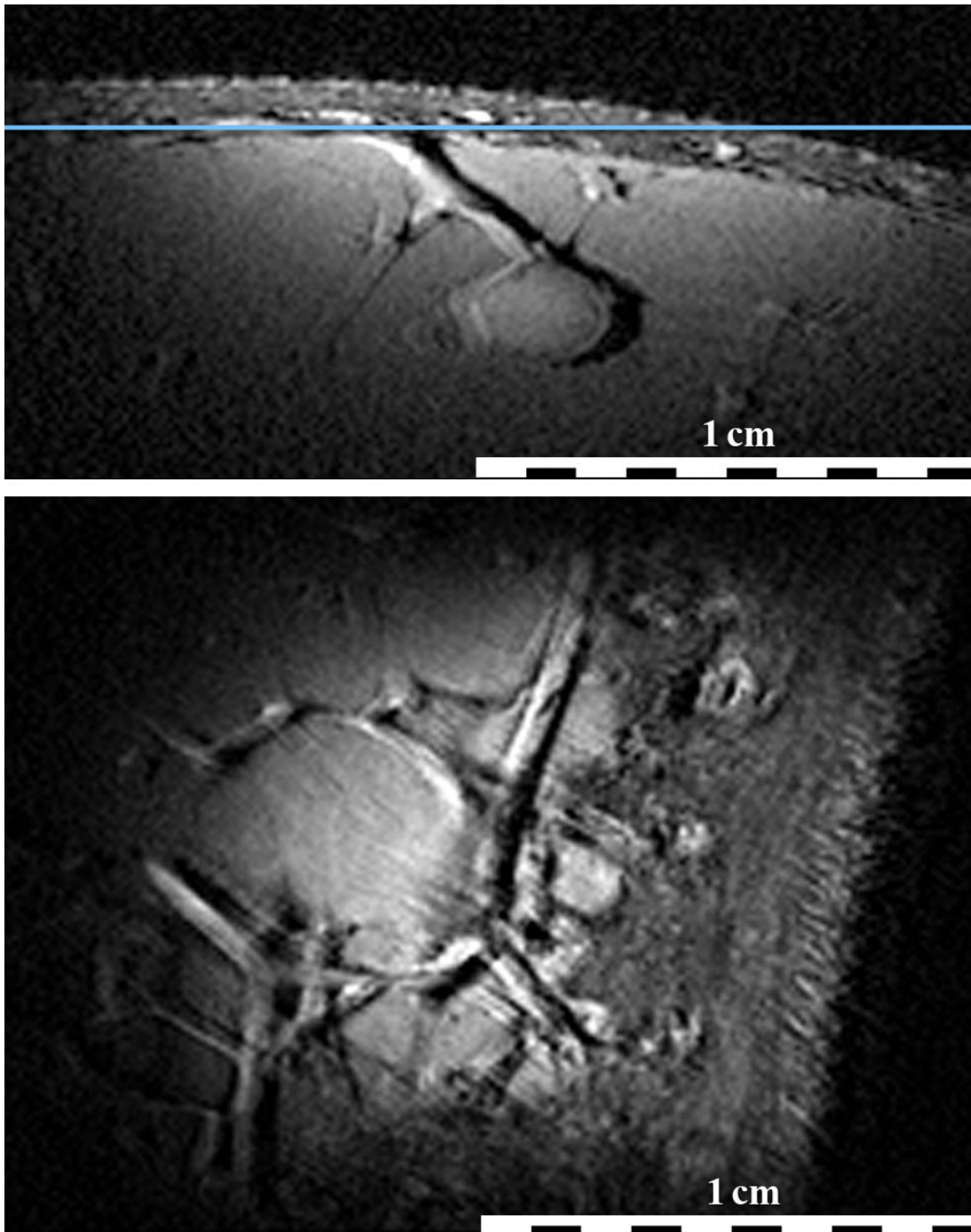


Figure 23: Skin images with HTS coil, 100 μm isotropic resolution
Top: Axial slice of the skin of the calf. A large (≈ 2 mm diameter) vessel is seen, connected to the deep vascular plexus by a smaller vessel (≈ 400 μm diameter). The blue line indicates the position of the bottom image.
Bottom: Sagittal slice; vessels of the deep vascular plexus are clearly seen.

The bottom left image is located in the deep dermal plexus at approximately 1.1 mm from the surface, where a large number of thin vessels can be seen. The chemical shift artifact is present in vertical direction, as this was the read-out direction in the acquisition.

The bottom right slice is located at a depth of ≈ 3.4 mm, a larger vessel in the hypodermis is displayed. Interestingly, the lumen and the vessel wall can be distinctly observed. The lumen has a diameter of 1 mm, the vessel walls are about 250 μm thick.

3.1.3.3 Vessels

3.1.3.3.1 Chemical shift filtered maximum intensity projections

Chemical shift filtering as described in section 4.1.3 was performed on the data to improve contrast and, thus, visibility of the vascular system. Figure 24 shows the result for experiment 3.

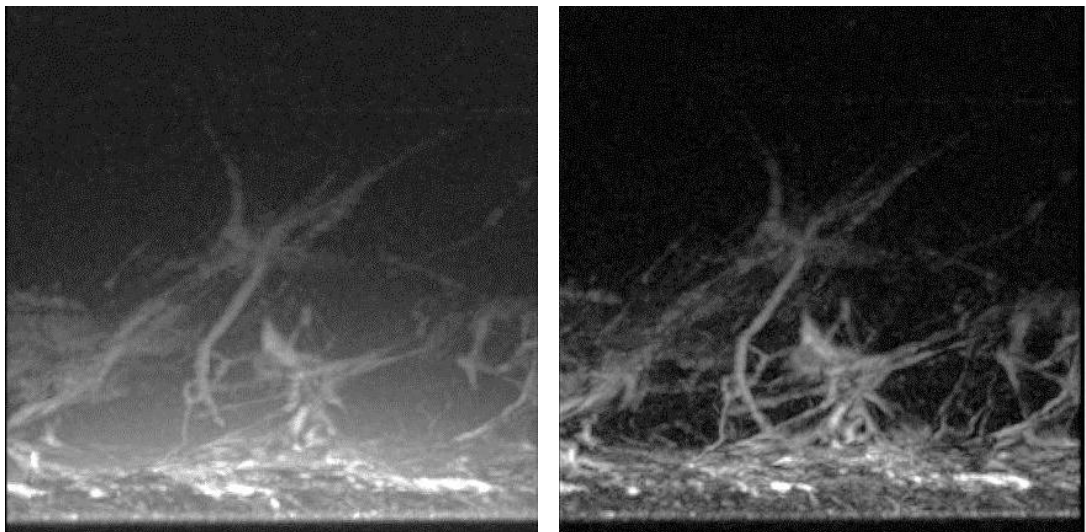


Figure 24: MIPs before and after chemical shift filtering

Left: Maximum intensity projection of the 80 μm isotropic data set from experiment 3 before filtering.

Right: MIP of the same data set after chemical shift filtering. The enhanced contrast of water-containing structures, i.e. mainly vessels, is obvious.

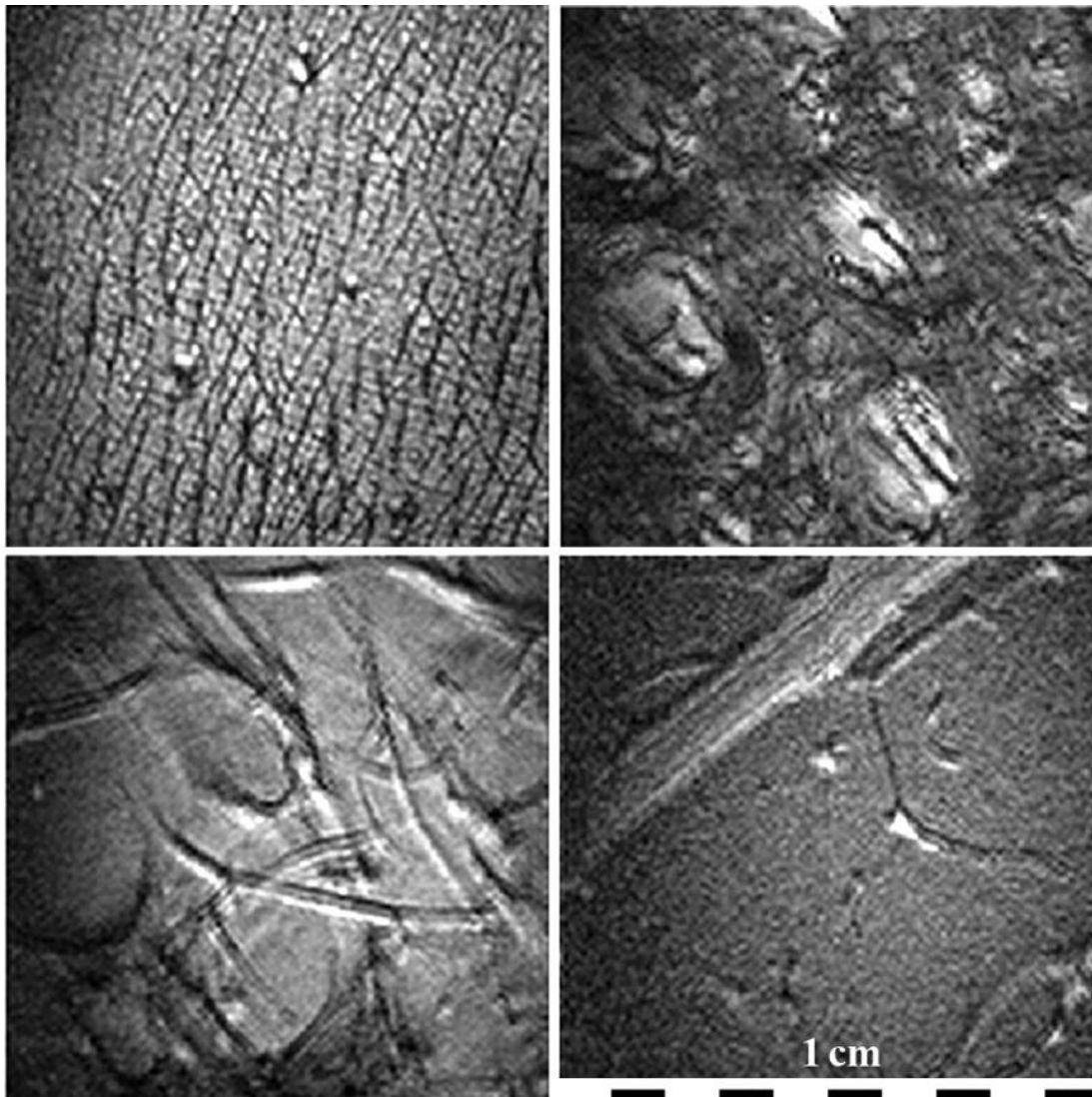


Figure 25: Skin images with HTS coil, 80 μm isotropic resolution

Top left: Cut through the epidermis. As the calf is covered by hairy skin, *areolae cutaneae*, rhombic fields of skin delimited by thin grooves, are observed. The circular spots are hairs passing through the epidermis.

Top right: Pilosebaceous units, i.e. hair follicles (round hyper-intense structures) and hair (dark stripes in the follicles) at a depth of $\approx 700 \mu\text{m}$ from the skin surface.

Bottom left: Vessels of the deep vascular plexus at the border of dermis and hypodermis at a depth of $\approx 1.1 \text{ mm}$.

Bottom right: Larger vessel in the hypodermis at a depth of $\approx 3.4 \text{ mm}$. The vessel wall can be distinguished from its lumen. The lumen diameter is 1 mm, vessel wall thickness $\approx 250 \mu\text{m}$.

3.1.3.3.1.2 Three-dimensional reconstructions of vascular trees

The cutaneous vasculature was segmented from the 3D data sets as described in section 4.2. Examples of the obtained vessel trees are displayed in Figure 26.

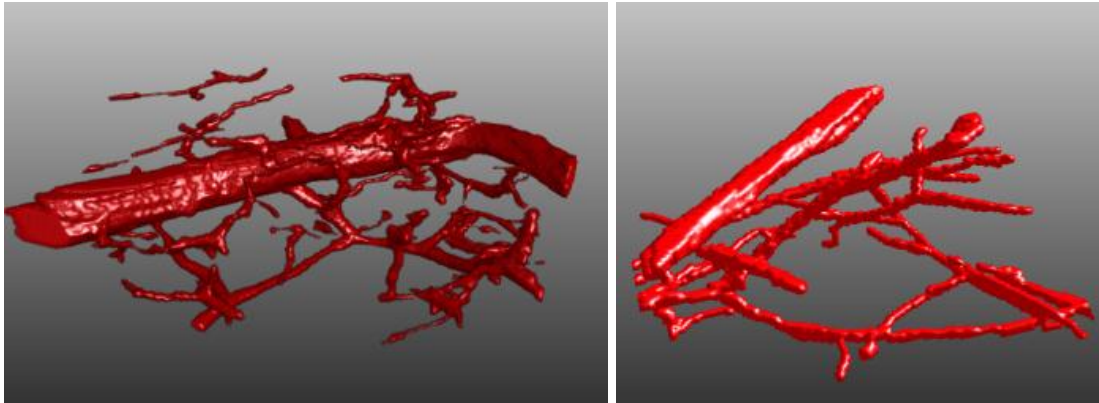


Figure 26: Segmented vessel trees from HTS coil data
Left: 3D reconstruction of the vascular tree in the dataset with isotropic spatial resolution of 100 μm (experiment 2).
Right: 3D reconstruction from the 80 μm isotropic dataset (experiment 3).

3.1.3.4 SNR

Table 4 summarizes the SNR values obtained for the different skin layers in all three experiments before averaging. For dermis and hypodermis a good correlation of the voxel volume and the measured SNR can be seen.

In the epidermis, SNR is best for the measurement with highest resolution in the direction perpendicular to the skin layers. This can be attributed to partial volume effects in the lower resolution case, averaging the strong signal from the epidermis with the hypo-intense dermis and air. It is approximately 70% higher than the epidermal SNR in experiment 2, despite a 10% lower voxel volume, i.e. an SNR gain of 84% taking into account the voxel size. Epidermal SNR per unit volume is 19% higher for experiment 3 than for experiment 2, which can also be explained by lower partial volume effects due to the higher resolution.

In Figure 27, the SNR profile for experiment 3 is plotted as a mean curve orthogonal to the skin surface. A strong peak for epidermis, followed by a lower SNR for the dermis and again stronger signal for the hypodermis is observed. As expected, the hypodermal signal decays with distance to the coil. The averaged signal over three scans (blue line) shows that SNR is increased by a factor of approximately $\sqrt{3}$, as predicted theoretically.

Experiment (voxel volume)	Epidermis (mean)	Dermis (mean)	Hypodermis (peak)
1 (0.9 nL)	38	18	33
2 (1 nL)	23	18	29
3 (0.51 nL)	14	9	12

Table 4: SNR values for different skin structures in the 1.5 T measurements

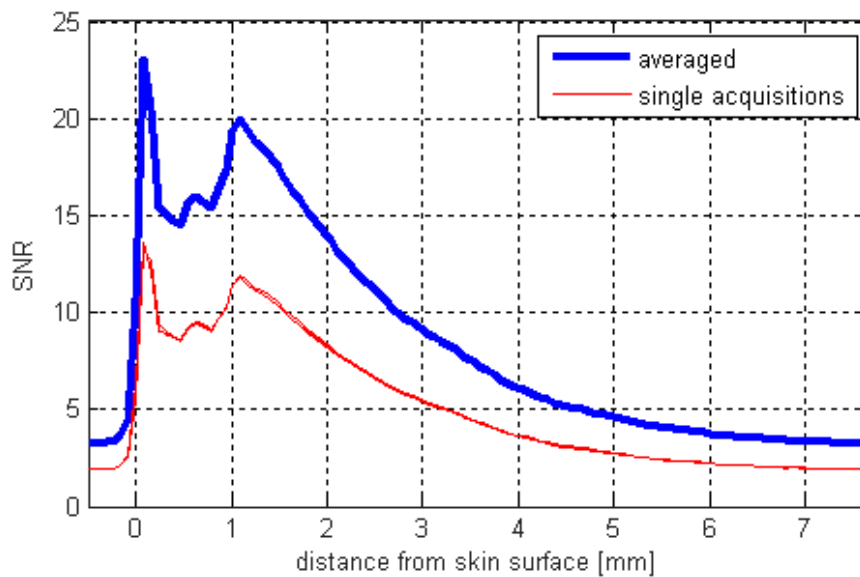


Figure 27: SNR profile for 80 μm isotropic resolution skin images

The average SNR in all slices parallel to the skin surface is plotted over the distance to the surface. A first peak at the skin surface is observed in the epidermis appearing hyper-intense in the images. The dermis (from 0.2-1.1 mm) appears hypo-intense, while the hypodermis starting at 1.1 mm is again hyper-intense. The signal decays with distance to the coil. The three red lines of the single acquisitions almost coincide and the SNR curve of the averaged data is a factor of $\sqrt{3}$ higher, as expected.

3.1.3.5 Loss contributions

3.1.3.5.1 Losses in the HTS material

The intrinsic losses in the HTS coil, probably due to imperfections in the material deposition were calculated to be $6 \pm 0.8 \text{ m}\Omega$. The losses in the HTS material due to the normal conducting flux vortices present in type II superconductors in the magnetic field were $62.5 \pm 2.1 \text{ m}\Omega$. Since the losses are weighted by the respective temperature, these low-temperature losses contribute little to imaging performance.

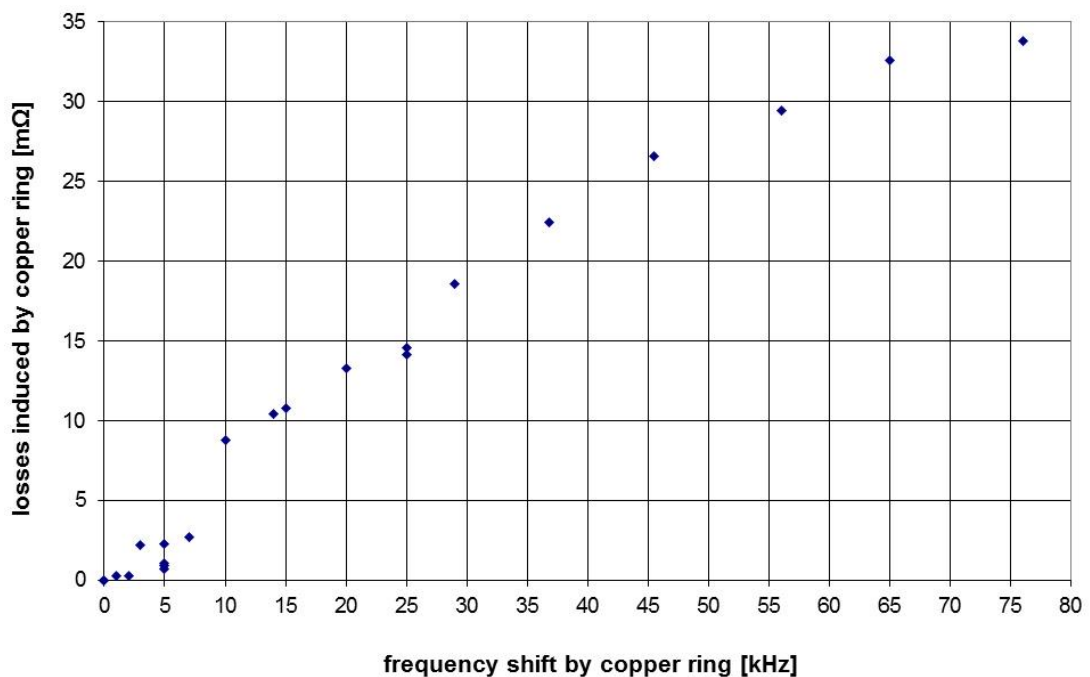


Figure 28: Noise contribution of the tuning copper ring
 Dependence of induced losses of the the copper ring in the HTS coil on the frequency shift it creates. As the copper ring approaches the HTS coil, the frequency shift and the corresponding losses increase.

3.1.3.5.2 Losses due to the tuning copper ring

Figure 29 shows the contribution of the copper ring used for fine-tuning of the resonance frequency to total losses in dependence of the shift in frequency it creates in the HTS coil. Figure 29 displays the influence of these losses on SNR.

For an assumed light load, i.e. a sample loss of $5 \text{ m}\Omega$, a frequency shift by the copper ring up to $\approx 10 \text{ kHz}$ can be tolerated. For heavier loads, even higher frequency shifts can be realized without degrading SNR by more than a few percent.

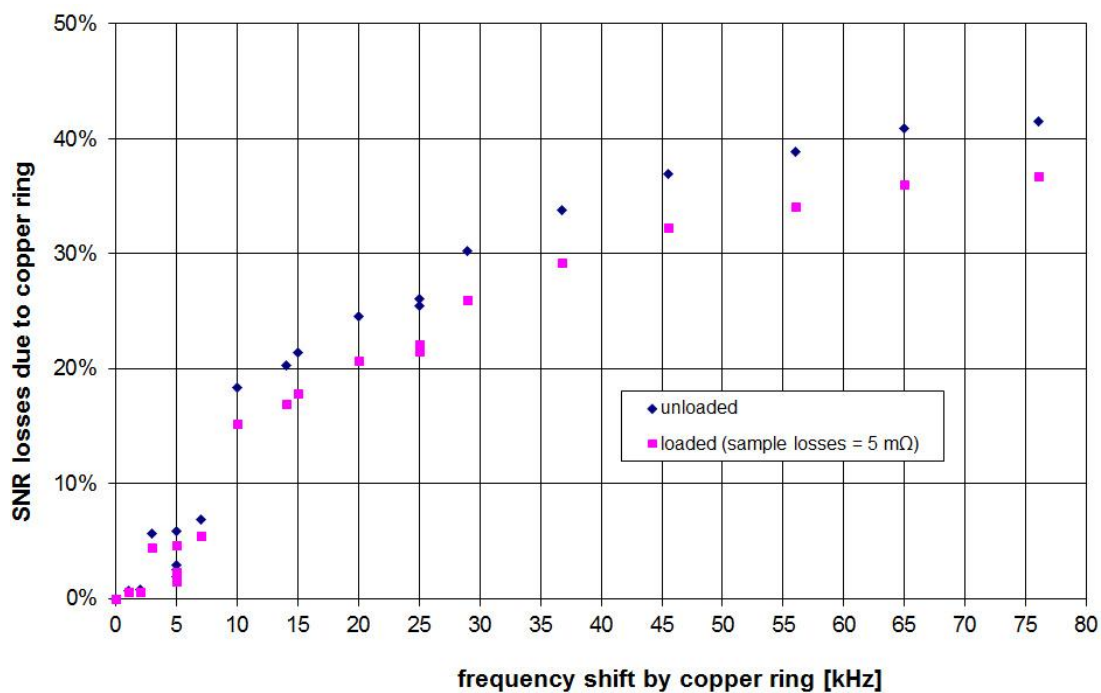


Figure 29: SNR degradation due to the tuning copper ring
SNR loss due to the copper ring. For frequency shifts $< \sim 10 \text{ kHz}$, the added losses are negligible, especially in the case of stronger load by the sample.

3.2 STUDY II: 15 MM SURFACE COIL AT 3 TESLA

3.2.1 Purpose

This study aimed at obtaining high SNR images of the human cutaneous vasculature in vivo. The required high spatial resolution can only be achieved by optimization of the measurement sensitivity. Here, the signal strength of a 3 T scanner and the sensitivity of a normal conducting 15 mm surface coil, together with a 3D gradient echo sequence and dedicated post-processing have been combined to reach this goal.

3.2.2 Materials and Methods

3.2.2.1 MR scanner

A Bruker MedSpec S300 whole-body scanner (Bruker Biospin, Ettlingen, Germany) is located at the MR Center of Excellence, Medical University of Vienna, Austria. The superconducting magnet from Magnex Inc., Oxford, U.K. has a main magnetic field strength B_0 of 3 T and a bore diameter of 80 cm.

The static magnetic field is produced by a current of 214 A circulating in the super-conducting coil. This coil is cooled in a 1140 l liquid Helium tank and is surrounded by 22 tons of iron in order to shield most of the leakage field. Various shim coils are used to make the main magnetic field B_0 as homogeneous as possible. Three types of shimming techniques are in use:

- Superconducting shim coils are placed within the cryo-tank. These are adjusted once at time of installation and are kept unchanged during normal operation.
- Passive shimming consists of small metal plates positioned on the inner side of the cryo-tank and are not changed during operation either.

- Linear shimming is performed by the gradient system and for higher order shimming, a set of non-super-conducting shim coils are mounted between magnet and gradient system.

The scanner is equipped with an actively shielded water-cooled whole-body gradient system BG-A55 leaving 55 cm net bore diameter for patients. Together with the gradient amplifier Copley 274 (Copley Controls Corp., Westwood, U.S.A.) the maximum gradient strength reaches 44.5 mT/m at a current of 600 A and a voltage of 350 V.

3.2.2.2 Network analyzer

An HP 3577A network analyzer (Hewlett-Packard Company, Palo Alto, CA, U.S.A.) is available at the MR Center of Excellence in Vienna. It was used for measurement of the quality factor of the RF coil.

3.2.2.3 RF coil

The RF coil used in this study consisted of a spiral encapsulated in plastic and attached to a box containing the tuning and matching electronics (see Figure 31). It was manufactured by Rapid Biomedical (Würzburg, Germany) and can be manually tuned and matched to optimize performance for different loading. The coil measures 15 mm in diameter and is used as a transceiver, i.e. as both a transmitter during excitation and as a receiver.

3.2.2.3.1 Coil characterization

The unloaded and loaded quality factors of the coil were measured with the abovementioned vector network analyzer by assessing

$$[\text{Eq. 53}] \quad Q = \frac{f_0}{\Delta f}$$

where f_0 is the Larmor frequency and Δf is the full width at half maximum of the reflection curve.



Figure 30: 3 Tesla Bruker MedSpec S300 whole-body scanner
The scanner is located at the MR Center of Excellence in Vienna

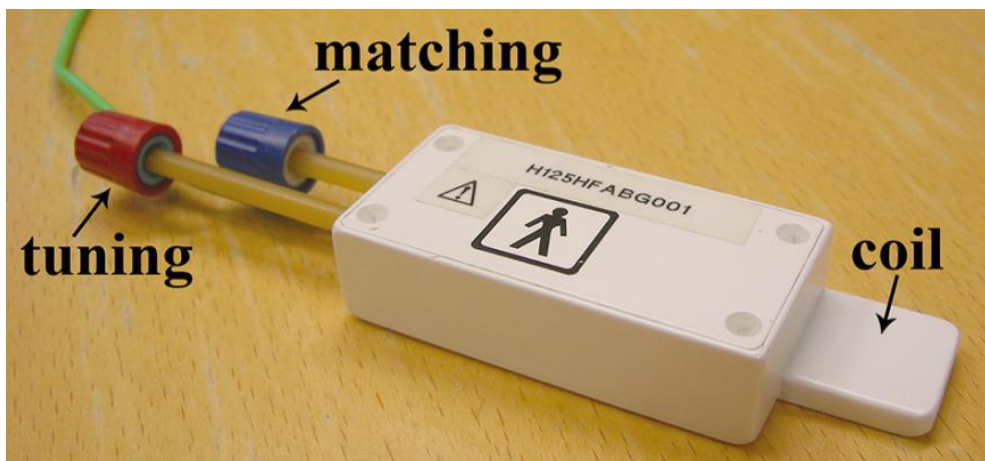


Figure 31: The 15 mm surface coil
Photograph of the 15 mm diameter transceive surface coil used for imaging of the skin vasculature in vivo at 3 Tesla. The coil can be tuned and matched on the individual subject. The actual coil winding is located in the region denoted in the image. The rest of the box contains tuning and matching capacitors.

With

$$[\text{Eq. 54}] \quad Q_0 = \frac{L\omega}{R_C} \quad \text{and} \quad Q_L = \frac{L\omega}{R_C + R_S}$$

where R_C are resistive losses in the coil and R_S representing losses in the sample, the ratio between coil losses and sample losses was derived.

3.2.2.4 Resolution phantom

In order to verify the actual spatial resolution of the sequence chosen for in vivo investigations, a resolution phantom with different structure sizes was used and the modulation transfer function was evaluated.

The resolution phantom (Figure 32) that was used [100, 101] is a silicon wafer, which has been structured by micro-lithographic etching methods. It comprises structures with spatial periods between 2048 μm and 64 μm , i.e. structure widths of 1024 μm to 32 μm in powers of two. The height of the structures is approximately 150 μm .

Image of the resolution phantom were acquired with the same sequence and post-processing steps as the in vivo skin measurements, i.e. k-space zero-filling to an isotropic voxel size of 75 μm and averaging of 3 scans after realignment.

3.2.2.4.1 Modulation transfer function

The modulation transfer function (MTF) describes the ability of an imaging system to detect signal variations at different spatial frequencies. It can be used to determine the spatial resolution limit of a certain method.

The modulation m is calculated from the maximum and minimum signal amplitudes A_{max} and A_{min} according to [Eq. 55] for each structure width.

$$[\text{Eq. 55}] \quad m = \frac{A_{max} - A_{min}}{A_{max} + A_{min}}$$

Finally modulation can be plotted over structure width and the resolution limit can be estimated by assessing the structure size where the MTF shows 50% of the full modulation [102, 103].

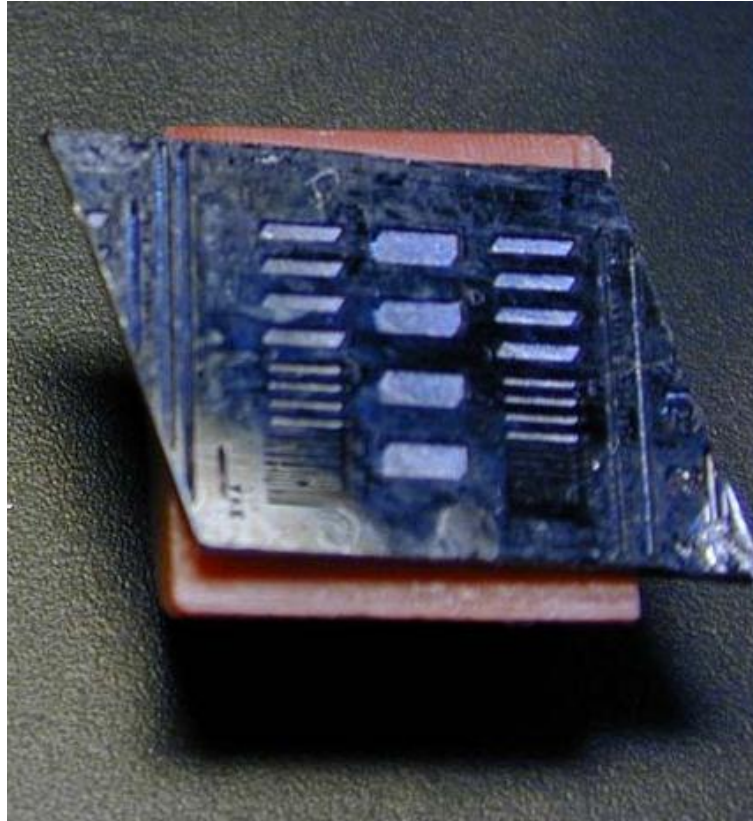


Figure 32: Resolution phantom (photograph)

The phantom contains structures with widths between 32 μm and 1024 μm in powers of two and is made from an etched silicon wafer. Image reproduced by courtesy of Andreas Berg [100, 101].

3.2.2.5 Subjects

In vivo data was acquired from nine healthy volunteers (3f/6m, age = 29 ± 5 years), after giving written informed consent, in agreement with local ethics regulation and according to the Declaration of Helsinki.

3.2.2.6 MR sequences

The acquisition consisted of a 3D gradient echo sequence with the sequence parameters summarized in Table 5. Read-out and slice selection directions were chosen parallel to the skin's surface; fold-over artefacts in the third dimension should not be visible due to the coil's sensitivity profile (according to Figure 21).

Parameter	Value
Repetition time TR	32.5 ms
Echo time TE	10 ms
Matrix size	170 x 170 x 110
Read-out bandwidth per pixel	47 Hz/px
Flip angle	Ernst angle (dermis)
Scan time	10 min 7 s

Table 5: Sequence parameters for the 3 T measurements

The flip angle was adjusted to the Ernst angle for the dermal/hypodermal interface by performing a series of low resolution scans with the same sequence, varying transmit power and searching for the power value corresponding to maximum SNR in the target region. Due to the chemical shift between water and fat and the low read-out bandwidth, a shift of ≈ 9 pixels between water and fat in read-out direction is expected.

Target regions were located on the thigh (anterior part, 10 cm above the right knee, 6 subjects, 2f/4m), on the back (5 cm left of the spine, 1 female subject), the calf (1 male subject), and the finger (last joint of the small finger of the right hand, 1 male subject).

Except for the finger measurement, subjects were placed feet first in supine position in the magnet, the coil was attached on the target region using adhesive tape. Care was taken to avoid mechanical pressure of the coil onto the skin, because this could occlude the small vessels to be detected. In thigh

and calf measurements, both legs were fixed on the patient table with straps to limit involuntary motion. The subject for the finger measurement was placed in prone (“Superman”) position, with his right arm outstretched.

Due to the spatially restricted signal acquired with the small surface coil, localisation of the FOV was done using a large FOV localiser sequence, where a bright spot was visible near the coil. Another localiser with smaller FOV was run on that spot. The actual skin imaging sequence was adjusted on the latter.

Three identical scans were performed on the target region for testing reproducibility and increase SNR by averaging. It is beneficial to run separate scans and average later because scans with excessive motion artefacts can be discarded without losing the information of the other acquisitions, and motion between scans can be corrected for by image realignment.

The significant drop in SNR anticipated due to the small voxels was compensated for by using a smaller coil, lower bandwidth and longer scan time.

3.2.2.7 Post-processing

All data sets were interpolated to 75 μm isotropic voxels by k-space zero-filling to facilitate realignment and segmentation (see section 4.1.1)

Before averaging the three data sets, image volumes were realigned using SPM8b [104] to correct for rigid-body motion occurring between acquisitions, i.e., for three directions of translation and rotation, respectively (see section 4.1.2).

The pixel-wise correlation coefficient between the first and the second and third volume was calculated to evaluate the registration performance quantitatively. The realigned data sets were averaged to improve the SNR by a theoretical factor of $\sqrt{3}$.

In all data sets epidermis, dermis, hypodermis and vessels were segmented from the averaged images. Additionally, a region of interest (ROI) outside the sample was defined for evaluation of background noise. Segmentation was performed manually using MRICro [105].

SNR was calculated as the ratio of mean signal of the segmented anatomical structures and noise standard deviation. The analysis was performed on the original single data sets and on the averaged data.

Skin layer thickness was computed from the segmented regions. For every position in the plane parallel to the skin surface, the thickness of the ROI in the third dimension was calculated and averaged over the FOV.

3.2.3 Results

The findings of this study have been published recently [106] and presented at scientific conferences [107, 108].

3.2.3.1 RF coil properties

The coil could be successfully tuned to the Larmor frequency and matched to 50Ω for the resolution phantom and all subjects.

The unloaded quality factor of the coil $Q_0 = 255$ decreased to $Q_L = 130$ when loaded by the thigh, therefore, according to calculations in section 3.2.2.3.1, sample losses were comparable to coil losses. This confirms that we are working with the smallest possible coil diameter of this type without being limited by internal coil noise.

3.2.3.2 Resolution phantom

In Figure 33, the resulting MR image of the resolution phantom is displayed in a sagittal and an axial view. The structures of the phantom are well observed and good agreement with the photograph (Figure 32) is achieved.

The blue boxes define the regions of interest on which the modulation was extracted (cf. Figure 34). Susceptibility artifacts at the edges of the phantom structures due to the susceptibility differences between the silicon wafer and the surrounding liquid are present (red arrows). Susceptibility artifacts (blue arrows) are observed, most probably due to small air bubbles and/or dust particles on the phantom.

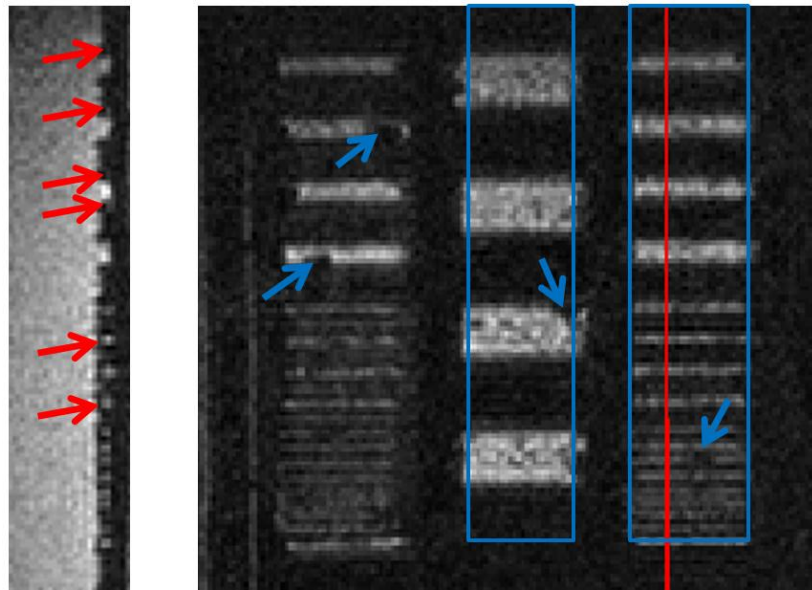


Figure 33: MR image of the resolution phantom

Left: Axial image slice through the phantom structures, the position is indicated by the red line in the right image. Susceptibility artifacts from the differences between silicon wafer and surrounding liquid are marked with red arrows.

Right: The displayed slice lies in the plane of the resolution phantom's structures. Susceptibility artifacts from air bubbles are marked with blue arrows.

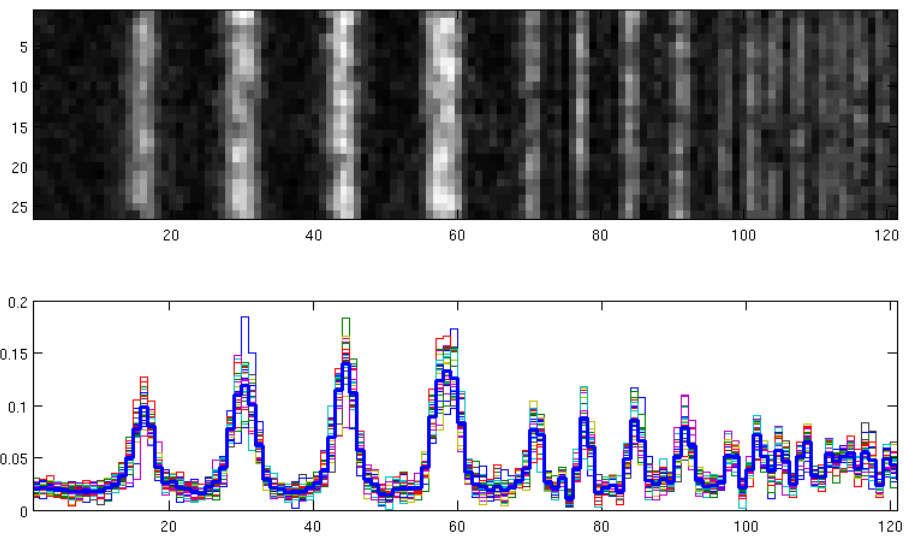


Figure 34: Modulation of the MR signal on the resolution phantom

Top: The ROI from Figure 33, where modulation was extracted.

Bottom: Signal intensity plots from each line in the ROI. The mean signal is plotted in bold blue. Modulation values were derived from each line. The scale on the abscissa is in pixels (1 px=75 μ m), the ordinate shows signal intensity in a.u.

From Figure 34, the modulation transfer function for the imaging experiment was derived (Figure 35). The resulting effective spatial resolution obtained when using the 50% modulation criterion is $\approx 150 \pm 50 \mu\text{m}$. It must be noted, however, that an experienced observer is able to distinguish structures with lower modulation as well.

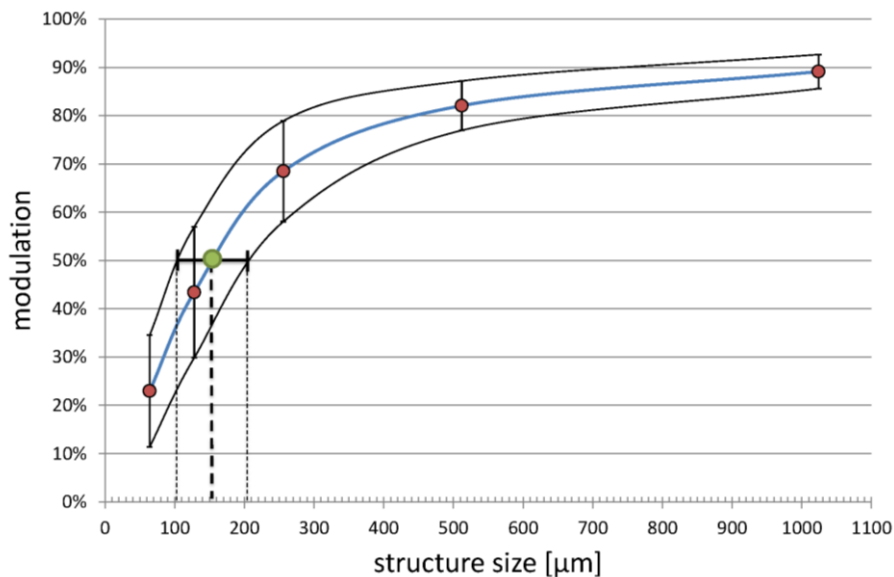


Figure 35: The modulation transfer function

The MTF is derived from measurements on the resolution phantom (Figure 32) with structure sizes of 64, 128, 256, 512 and 1024 μm , plotted over structure size. Structures with sizes down to $\approx 150 \pm 50 \mu\text{m}$ can be resolved, i.e. show a modulation of 50% or higher.

3.2.3.3 Anatomical features

3.2.3.3.1 Skin layers and dermal structures

Three main skin layers were manually segmented from the 3D data sets. The volume of the different ROIs was $73 \pm 7 \mu\text{l}$ for the epidermis, $263 \pm 31 \mu\text{l}$ for the dermis, $949 \pm 54 \mu\text{l}$ for the hypodermis and $8 \pm 2 \mu\text{l}$ for the vessels. Noise standard deviation was derived from a region with a volume of $63 \pm 11 \mu\text{l}$.

Skin layer thickness was extracted automatically from the segmented ROIs. A summary of the different anatomical regions investigated is given in Table 6.

For the thigh measurements, thickness is given as the mean value and standard deviation over subjects. For the other locations, standard deviation refers to the variation across the measurement points within the individual subject.

	thigh (n=6)	calf (n=1)	finger (n=1)	back (n=1)
epidermis	307±18 µm	252±85 µm	224±71 µm	235±65 µm
dermis	1136±129 µm	1488±274 µm	609±25 µm	2281±406 µm

Table 6: Skin layer thickness for different anatomical regions

Standard deviation for the skin layers of the thigh is based on the variance across subjects, while for the other areas the variance across the measurement points within the dataset was assessed.

Figure 36 shows slices from an exemplary thigh skin data set. As expected (cf. Figure 12 and Figure 11), a layer of vessels parallel to the skin surface at the dermal/hypodermal interface, the deep vascular plexus (Figure 36C), was observed consistently across subjects. Vessel diameters in this region, as obtained from the images, vary between 100 µm and 250 µm. Even smaller vessels in the superficial vascular plexus could be visualised in some data sets (Figure 36B), although with weaker contrast due to partial volume effects. For the same reason, vessel diameters in this region cannot be extracted reliably.

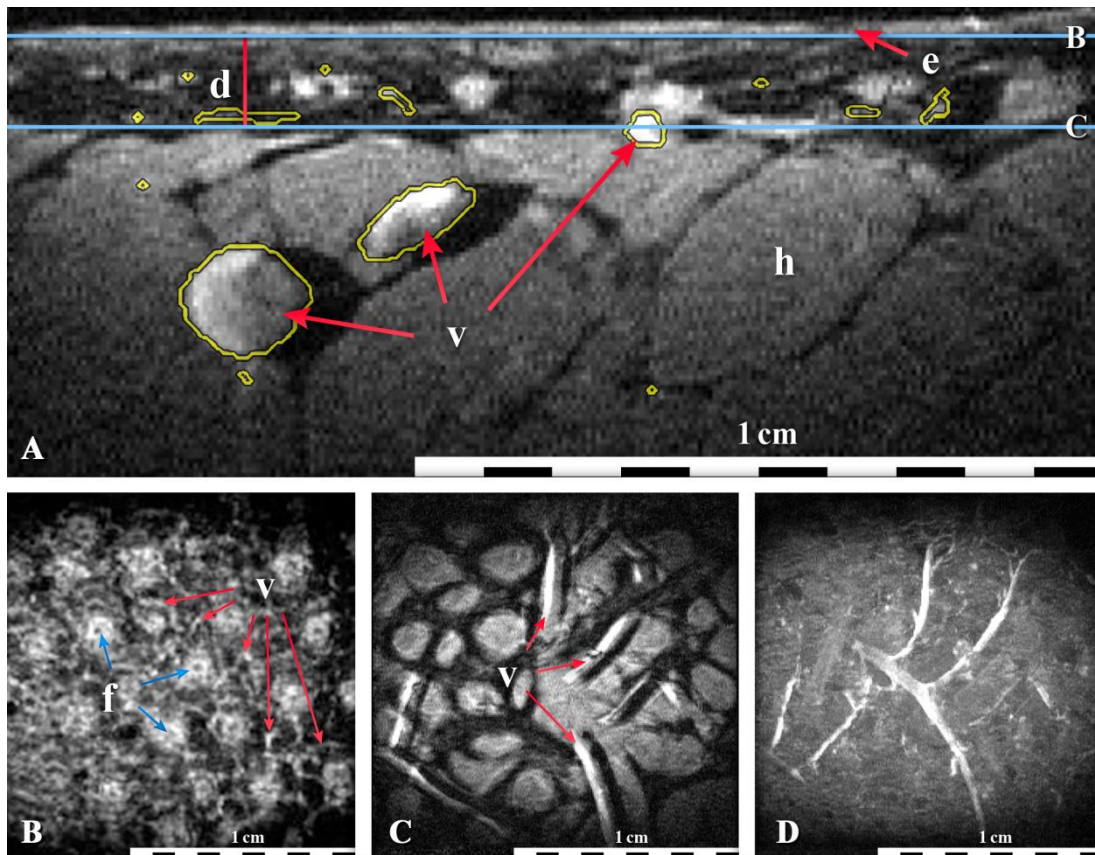


Figure 36: Human thigh skin in vivo with isotropic resolution of 100 μm
 Images show a typical data set acquired on the thigh, 10 cm above the right knee, obtained at 3 T using a 15 mm copper loop coil. Image A represents a slice perpendicular to the skin surface, while images B–D show parallel sections.
 A: Slice perpendicular to the skin surface. Skin layers epidermis (e), dermis (d) and hypodermis (h) are clearly distinguished. Vessels (v) with diameters from $\sim 100 \mu\text{m}$ to 1.4 mm are observed. The position of the slices in B and C are indicated by blue lines, contours of segmented vessels are drawn in yellow.
 B: Slice parallel to the skin surface, at the border of epidermis and dermis. The vascular network in the superficial vascular plexus is seen (v, red arrows). Since the vessels in this area are smaller than the voxel size of the MR acquisition, their diameters are likely to be over-estimated. The hexagonally positioned hyper-intense patches (p, blue arrows) represent cross-sections of pilosebaceous units; the hair itself is seen as a black dot in the middle of each unit.
 C: Slice parallel to the skin surface at the interface of dermis and hypodermis. The “shadow-like” appearance of the vessels is due to the high chemical shift between water and fat. Vessels (v) and hypodermal fat lobules are well distinguished.
 D: Corresponding maximum intensity projection to C. The vasculature, in particular the vessels of the deep plexus (image C) are visible with high contrast.

Finger and back images are shown in Figure 37, where epidermis, dermis, and vessels are visible. Additionally, the cartilage layer of the finger joint and fingerprints are observed; in the skin of the back, pilosebaceous units are identified.

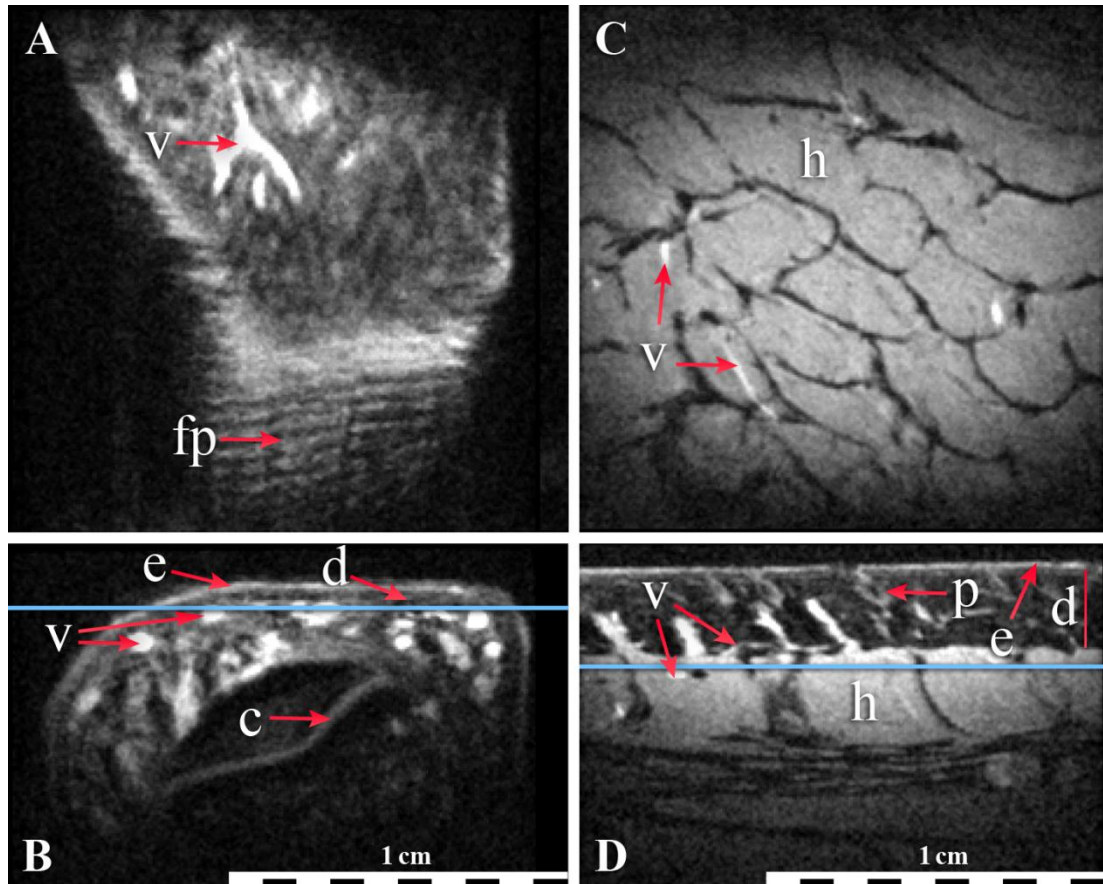


Figure 37: Images of the finger and the skin of the back

The top row shows coronal sections, the bottom row transverse sections of the finger (A, B) and the skin of the back (C, D).

A: A vascular bifurcation (v) and fingerprints (fp).

B: Vessels (v), epidermis (e), dermis (d) and joint cartilage (c). The dermis in the finger is approximately 600 μm thick.

C: Vessels in the deep vascular plexus, hypodermal fat.

D: Skin layers epidermis (e), dermis (d) and hypodermis (h) are visible with good contrast. The dermis on the back is thicker than on the thigh or on the finger, it measures approximately 2.3 mm. Dermal structures such as pilosebaceous units (p) and vessels (v) are observed.

3.2.3.3.2 Vessels

3.2.3.3.2.1 Chemical shift filtered maximum intensity projections

To enhance the visibility of the vascular system a chemical shift filtering technique as described in section 4.1.3 was applied. Figure 38 shows maximum intensity projections of the data set displayed in Figure 36 and Figure 39 before and after chemical shift filtering.

As seen in the bottom row of the figure, the contrast of the vascular system can be drastically improved. For examination by clinicians, a rotating animation of the maximum intensity projection was produced, providing a good three dimensional impression of the vessel tree, even before the time-consuming segmentation process.



Figure 38: MIPs before and after chemical shift filtering

Top: Maximum intensity projection of a 100 μm isotropic data set before filtering
 Bottom: MIP of the same data set after chemical shift filtering (see section 4.1.3).

The enhanced contrast of water-containing structures,
 i.e. mainly vessels is obvious.

3.2.3.3.2.2 Three-dimensional reconstructions of vascular trees

The cutaneous vasculature was segmented from the 3D data sets as described in section 4.2. For visualization of the results, a shaded 3D rendering of the resulting vascular tree was performed using either the Viewer3D package [109] in MATLAB 7.8 (see section 4.4.1) or in MeVisLab (see section 4.4.2).

Figure 39 and Figure 40 show some exemplary vessel trees. Figure 39 shows a good example of a larger hypodermal vessel of about 1.4 mm in diameter connected to the deep vascular plexus by a smaller vessel with mean diameter of 0.9 mm decreasing in diameter towards the more superficially located deep plexus at the border to the dermis. Several branches spread from this connecting vessel, each one splitting into multiple branches within the plexus.

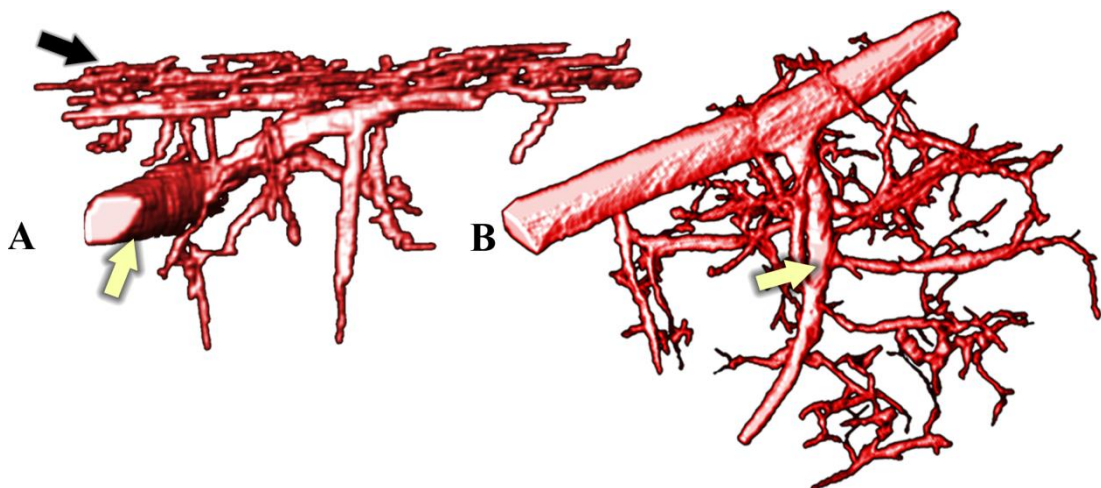


Figure 39: 3D reconstruction of a segmented vessel tree

A 3D rendering of the segmented vessel tree corresponding to the data set shown in Figure 36 from two different viewing angles created using Viewer3D in MATLAB.

A: The large vessel (bright arrow) has a diameter of 1.4 mm and lies in the hypodermis. The network of smaller vessels corresponds to the deep vascular plexus (dark arrow) at the interface of dermis and hypodermis.

B: The deep vascular plexus is connected to the larger vessel by a medium-sized vessel (arrow) with a mean diameter of 0.9 mm.

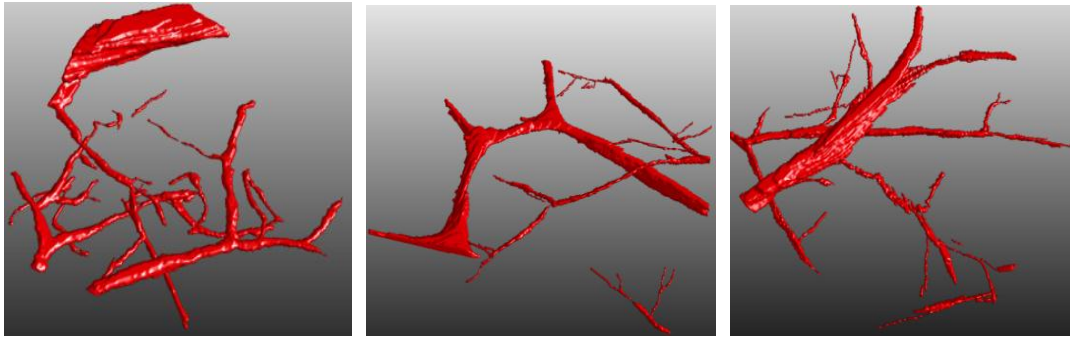


Figure 40: Examples of other segmented vessel trees

The vessels were manually segmented and then 3D rendered using MeVisLab. In all data sets the characteristic network of the deep vascular plexus was observed.

3.2.3.3.2.3 Vascular parameters

The calculation of relative blood volume as the percentage of vessel voxels from the whole segmented skin volume resulted in $6.2 \pm 1.7 \mu\text{l}/\text{cm}^3$ or $0.62 \pm 0.17 \text{ vol}\%$, over the study population. It must be noted, however, that the true blood volume might deviate from these values, since on the one hand capillaries are much smaller than the spatial resolution of the experiment. Therefore, they are not considered in the calculation and, on the other hand, visible vessels might be overestimated in size due to partial volume effects.

Only a few reference values could be found in literature. Välisuo et al. [110] calculated values between 0.16 and 0.45 vol%, whereas Reuss [111] reported 1.5 to 5 vol%, both studies using optical reflectance methods and assumptions on the blood oxygenation level to obtain their results. The value found here is, therefore, in reasonable agreement with these data, given the high variability with respect to subject and anatomical location.

Table 7 summarizes vascular parameters obtained by applying the algorithm described in detail in section 4.3. The values in the upper part of the table are given as percentages of total vessel length. The results show that the vast majority (2/3) of the vessels observed in the microscopic MR data sets are vessels with a diameter smaller than $200 \mu\text{m}$. Vessels found in the deep

dermal plexus mostly fall into this range, explaining the high percentage. Thicker vessels are infrequent, which seems quite reasonable.

The bottom part of Table 7 shows the distribution of branch lengths, meaning the distance along a vessel from an end point to a junction or the distance between two junctions. Two thirds of the branches found are 4 – 6 mm long, short branches below 2 mm in length form the second largest group representing 15% of the total number of branches. Other lengths are only seen in 10% of the branches. These results were submitted to a conference [108].

Vessel diameter	< 200 μm	200 – 400 μm	400 – 1200 μm	> 1.2 mm
% of total vessel length	73 \pm 8 %	20 \pm 6 %	6 \pm 2 %	1 \pm 2 %
Branch length	0 – 2 mm	2 – 4 mm	4 – 6 mm	6 – 8 mm
Relative frequency	15 \pm 4 %	6 \pm 2 %	75 \pm 6 %	4 \pm 4 %

Table 7: Quantitative vascular parameters from 3 T MR microimaging

3.2.3.4 Image quality

3.2.3.4.1 Realignment

Rigid body co-registration of data of the second and third scans to the first scan revealed that subjects had moved by 3.8 ± 1.4 voxels (= $285 \pm 105 \mu\text{m}$) between scans, the maximum was 7.2 voxels ($540 \mu\text{m}$). Before realignment, the mean voxel-wise correlation coefficient between second and third scans versus the first scan was 0.69 ± 0.06 . After realignment, the correlation coefficient was consistently improved in all data sets to a mean value of 0.80 ± 0.07 .

3.2.3.4.2 SNR and CNR

All skin layers and the vascular tree could be observed with sufficient SNR for segmentation and measurement of skin layer thickness. Even in the hypo-intense dermis SNR of ≈ 5 in single acquisitions and ≈ 8.5 after averaging was

obtained. Since the surface coil's sensitivity is non-uniform and decreasing with distance to the coil, signal intensity was strongly varying, especially in the hypodermis. Therefore, it must be understood that SNR in the upper part of hypodermis was considerably higher than the mean value given here. The same argument holds for vessels within the hypodermis. Epidermis and dermis are both located much closer to the coil and are thinner; therefore signal variations due to the coil sensitivity profile were negligible. Table 8 summarises the SNR values found in the study population. After averaging, an SNR increase of 1.71 was obtained, as expected.

The contrast-to-noise ratio (CNR) of vessels with respect to dermis and hypodermis were calculated as the difference in SNR between these structures. CNR of vessels to the dermis was 10.8 ± 2.9 for the dermis and 6.1 ± 3.2 for the hypodermis.

	Epidermis	Dermis	Hypodermis	Vessels
mean \pm SD before averaging	6.3 ± 0.2	5.0 ± 0.3	7.9 ± 0.6	11.2 ± 1.2
mean \pm SD deviation after averaging	10.8 ± 0.2	8.5 ± 0.6	13.5 ± 1.0	19.3 ± 2.2
SNR increase by averaging	1.71 ± 0.09	1.70 ± 0.22	1.71 ± 0.26	1.72 ± 0.38

Table 8: SNR in different dermal structures

Signal-to-noise ratios of different anatomical structures across all subjects. The average improvement in SNR of 1.71 ± 0.24 is in excellent agreement with the theoretical prediction of $\sqrt{3}$.

3.3 STUDY III: 6 MM SURFACE COIL AT 7 TESLA

3.3.1 Purpose

Improvement of detection sensitivity in MRI can be used to increase both spatial and temporal resolution, providing faster and more accurate measurement of clinically relevant data in vivo.

In this feasibility study, the sensitivity increase by the use of higher field strength and small, flexible surface coils providing good geometrical matching to the sample yielding high SNR have been combined.

Auto-resonant monolithic coil design enables the fabrication of RF coils without lumped elements, avoiding additional losses and decrease of B_1 -homogeneity caused by such elements.

3.3.2 Materials and Methods

3.3.2.1 MR scanner

The experiment was performed on a whole-body 7 T scanner (Siemens Magnetom). For the scanner a new research building was constructed at the MR Center of Excellence, and officially inaugurated in October 2008.

The scanner weighs 32 t and the magnetic field is passively shielded by 270 t of steel. The magnet is 3.4 m long and has a bore with 90 cm diameter, the free bore diameter is 60 cm. The magnet has passive shimming and active shimming coils for 1st and 2nd order shim.

The scanner is equipped with gradient coils with a maximum strength of 45 mT/m in z-direction parallel to the static magnetic field and 40 mT/m in x and y direction. The maximum slew rate is 200 T/m/s, the rise time is 200 μ s.



Figure 41: Siemens Magnetom 7 T

This scanner has been installed at the MR Center of Excellence in Vienna in 2008.

3.3.2.2 Network analyzer

An Agilent E5061A network analyzer (Agilent Technologies, Palo Alto, CA, U.S.A.) served for evaluation of the fine-tuning of the 6 mm surface coil.

3.3.2.3 RF coil

The coil with 6 mm outer diameter was fabricated at MinaSys, Department of Physics and Process Technologies of the IEF laboratory at the Université Paris-Sud XI in Orsay, France. The calculation of its geometry was performed using the MATLAB toolbox developed in this thesis (annex 6.2).

In order to electrically isolate the coil from the sample it was placed in a fitting pouch made of polyvinylchloride (PVC).



Figure 42: Photograph of the 6 mm coil for 7 T

Left: One face of the 6 turn coil used in this study. Each winding has a thickness of 100 μm and is made of copper deposited on both sides of a flexible Kapton® substrate [112, 113].

Right: The coil in original size, compared to a 1 cent coin.

3.3.2.4 Measurement setup

The skin measurements were performed in collaboration with Luc Darrasse, Jean-Christophe Ginefri, Marie Poirier-Quinot, and Rose-Marie Dubuisson within our international collaboration with IR4M in Orsay, France.

3.3.2.4.1 Inductive coupling to the receiver chain

The RF coil was inductively coupled to the 1H channel of a commercially available 9 cm double tuned ($^1\text{H}/^{31}\text{P}$) surface coil (Rapid Biomedical, Würzburg, Germany), since this was the smallest available coil with connection to the scanner. Direct wiring of the small coil was not feasible with reasonable technical complexity. One reason is the small size of the coil which would render soldering and wiring difficult. Capacitive coupling would contradict the idea of using of an auto-resonant circuit without lumped elements, whereas inductive coupling allows for intrinsic electrical balancing of the probe and therefore minimizes losses in the sample. Also, no additional

matching circuit, nor coil plug and coil file were necessary for the connection to the scanner.

Since the difference in size between the 9 cm coupling loop and the 6 mm coil is relatively large, a copper disk with an outer diameter of 90 mm and an inner diameter of 24 mm was placed on the larger coil. The idea is to concentrate the larger coil's field to the inner opening of the copper disk ensuring sufficient coupling between the 6 mm and the 9 cm coil. The copper disk was slit at one position to prevent currents from circulating around the inner opening of the disk.

The 6 mm coil and the copper disk were centered on the 9 cm loop as can be seen in Figure 43, which shows the final arrangement of the coils on the subject's calf.

3.3.2.4.2 Fine tuning of the RF coil

The resonance frequency of the auto-resonant RF coil was fine tuned to the correct frequency of 297.2 MHz with dielectric material. A layer of adhesive tape was used for this purpose, placed over half of the PVC pouch containing the coil. By repositioning the coil within the pouch a variable percentage of the coil's surface was covered by the adhesive tape resulting in a shift of the resonance frequency. The more surface was covered, the lower the resonance frequency.

Fine-tuning was performed with the coils in their final position on the subject and the resonance frequency was determined using a small coupling loop and the network analyzer.

3.3.2.5 Sequence

A 3D gradient echo sequence with nominal 100 μm isotropic resolution with the parameters given in Table 9 was used. The read-out bandwidth was kept small in order to shorten the echo time and gain SNR. The read-out direction was chosen parallel to the skin surface to avoid overlapping of hypodermal fat signal into other skin areas due to the chemical shift displacement of 9 voxels.

Parameter	Value
Repetition time TR	50 ms
Echo time TE	10 ms
Matrix size	70 x 70 x 64
FOV	7 x 7 x 6.4 mm ³
Read-out bandwidth per pixel	110 Hz/px
Flip angle	Ernst angle (dermis)
Scan time	3 min 44 s

Table 9: Sequence parameters for the 7 T measurements

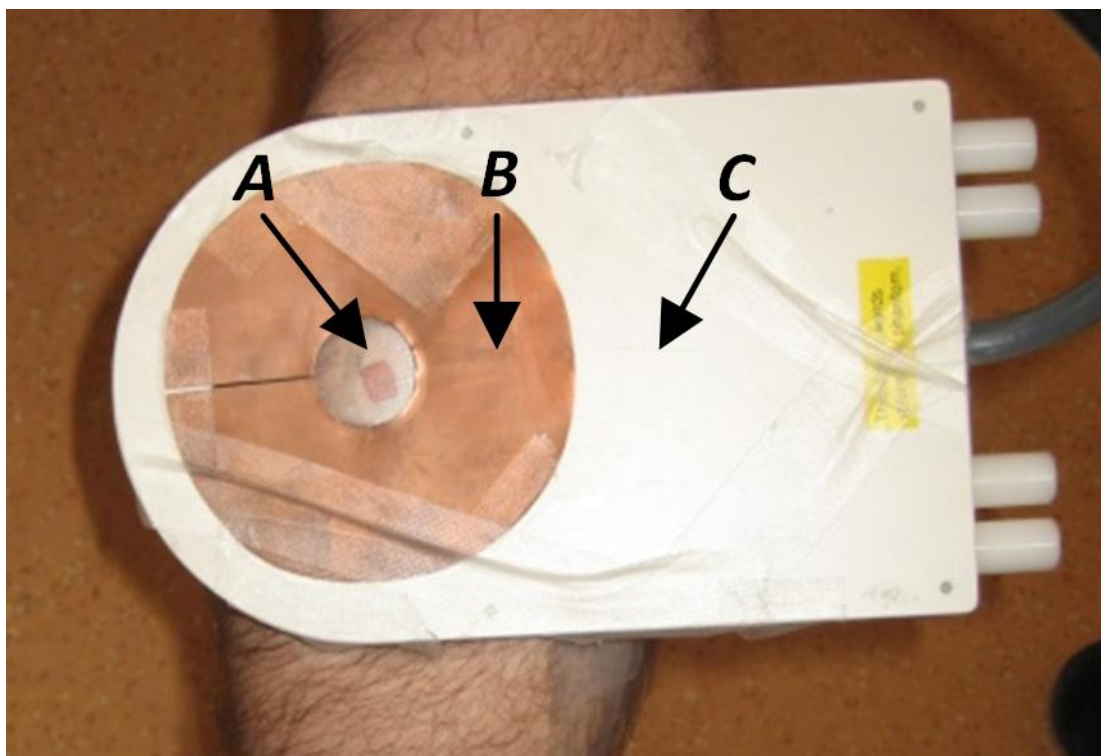


Figure 43: Experimental setup for 7 T skin imaging
The 6 mm coil (A) is centered on a slit copper sheet (B) acting as a field concentrator on a commercial 9 cm surface coil (C).

3.3.2.6 Subjects

The measurements were performed on the calf of a healthy subject (male, 35 years old) after informed written consent, according to the regulations of the local ethics committee, and the Declaration of Helsinki.

3.3.3 Results

This study has been presented in [114].

3.3.3.1 RF coil

The calculation of the coil geometry resulted in a structure with 6 turns on both sides of a Kapton® substrate with 125 μm thickness and a dielectric constant of $\epsilon = 3.25$. The outer diameter of the coil is 6 mm. The conductor width and the spacing between conductor turns was 100 μm . The used coil is seen in Figure 42.

3.3.3.2 Images

The following figures display images obtained with the 6 mm auto-resonant coil at 7 T. Figure 44 shows three orthogonal slices of the superficial layer of a tomato. The half-spherical sensitivity pattern of the coil is well observed and signal is seen to a depth of approximately 3 mm. The dark circular structures in the images are air bubbles of 500 μm in diameter enclosed in the tomato.

Figure 45 displays a transversal slice of the human calf skin *in vivo*. The skin layers epidermis, dermis and hypodermis can be clearly identified. Since the read-out direction was chose horizontally with respect to this image, epidermis and dermis are shifted to the left by 9 voxels with respect to the hypodermis.

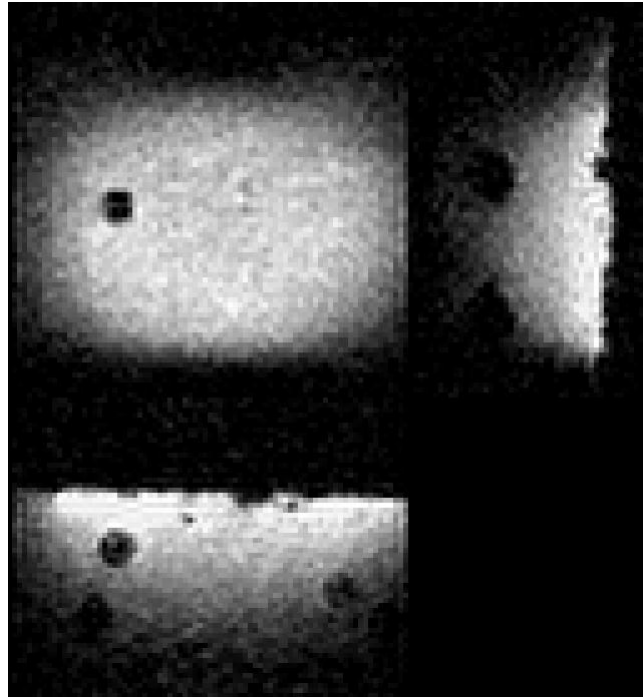


Figure 44: 7T tomato images with 6 mm coil, 100 μm isotropic resolution
The image shows slices in all 3 directions from the 3D data set. The black spots are air bubbles of $\approx 500 \mu\text{m}$ in diameter in the tomato.
The image is acquired from 4 averages in a total time of 15 min.
The total width of the figure corresponds to 13.4 mm

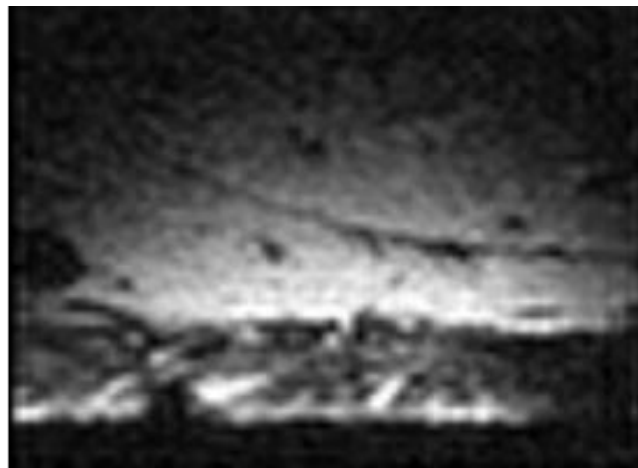


Figure 45: 7T skin image with 6 mm coil, 100 μm isotropic resolution
Characteristic features of the skin such as the skin layers epidermis, dermis, and hypodermis, as well as pilosebaceous glands (hair follicles, hyper-intense structures in the dermis) are visible. The width of the image corresponds to 7 mm.

4 IMAGE PROCESSING

The purpose of image processing in medical imaging is improvement of the diagnostic value of the acquired data, i.e. providing means to the observer, that help to identify lesions or pathologies more easily. This can either be achieved by controlled manipulation of the images themselves or by extraction of quantitative parameters from the data. “Controlled manipulation”, in this context, can e.g. include various forms of filtering, such as denoising, intensity correction or others. However, image processing algorithms must not alter or invalidate the diagnostic outcome in a sense that the diagnosis of the processed image would be contradictory to the diagnosis of the original image, therefore, image manipulations have to be performed with special vigilance.

4.1 IMAGE ENHANCEMENT

4.1.1 Zero-filling

The digital resolution of images can be changed by interpolation via zero-filling of k-space data before Fourier transform. This means that data points with value of “0” are added at the edges of the k-space data. In the 1D case, this corresponds to adding zeroes after a line of data. This is routinely performed in MR spectroscopy in order to improve spectral resolution and separation of peaks.

In this work, zero-filling was performed on 3D k-space data, adding zeros at all sides of the k-space cube. A too high zero-filling factor combined with a sharp edge between real data points and zeros has to be avoided, because images will suffer from Gibb’s ringing, i.e. truncation artifacts. A value of 4/3 for the zero-filling factor has been used in most imaging experiments in this thesis, i.e. the digital resolution of 100 μm isotropic data was increased to $100 \mu\text{m}/(4/3) = 75 \mu\text{m}$.

Of course, adding zeroes to the data cannot improve the real spatial resolution, which is determined by the acquisition parameters and hardware, but it can improve the appearance to the eye. It also facilitates the segmentation process, because curves can be better approximated by the segmentation with higher digital resolution, and partial volume effects can be better considered in manual segmentation.

4.1.2 Averaging after realignment

Signal averaging is a well-known technique in most experimental science. By averaging N samples, the signal-to-noise ratio is improved by a factor of \sqrt{N} . In most MR sequences, the number of averages can be set directly on the console.

A real advantage from averaging can only be taken if the signals to be averaged only differ by noise and the “true” signal is kept constant. This only holds for acquisitions where the extent of subject motion is clearly below

voxel size. With the very small voxels used in the context of micro-imaging, motion quickly surpasses this threshold and a correction for motion has to be applied before averaging.

In this work, the realignment algorithm of the SPM8 [104] toolbox was used to correct for the motion occurring in between scans. This technique uses a least squares approach and a 6 parameter rigid body spatial transformation [115]. The six parameters include three degrees of freedom for translation, i.e. in the three spatial directions and three degrees of freedom for rotation, i.e. roll, pitch, and yaw. Images were realigned to the first data set and averaged afterwards. Figure 46 shows a typical result of the realignment procedure.

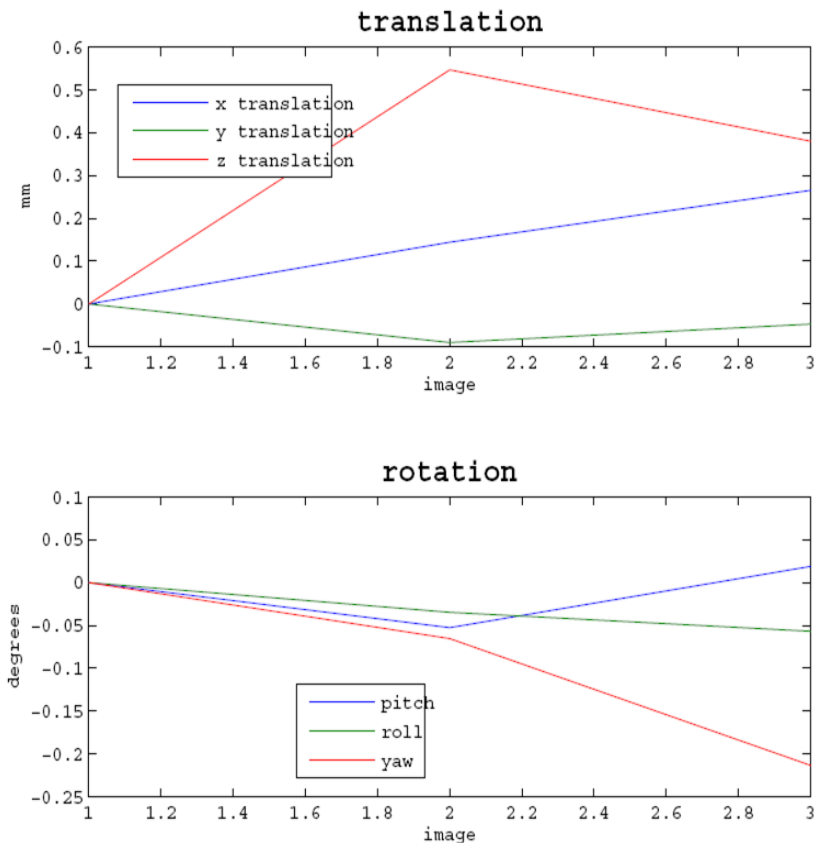


Figure 46: Typical result of image realignment

Top: Parameters for translation of the 3D data with respect to the first scan.

Bottom: Rotation parameters with respect to the first scan.

4.1.3 Chemical shift filter

Image artifacts are usually not improving the clarity of an image, but sometimes it can be helpful to exploit exactly these artifacts in order to get even more specific information from the image.

Let us consider the artifact arising from the chemical shift between water and fat due to the use of a low read-out bandwidth for the MR acquisitions. We could model the appearance of vessels within adipose tissue by assuming

- the vessel signal is equal to the homogenous background signal of the adipose tissue in the hypodermis (signal intensity = 1, w.l.o.g.)
- the vessel signal is shifted to the right by the value of the chemical shift artifact d and superimposed on the background

If we now imagine the cross section through an ideal cylindrical vessel. the two assumptions above result in a circular black hole (signal intensity = 0) and a white circular spot (signal intensity = 2) with their centers at a distance d from each other, as shown in Figure 47.

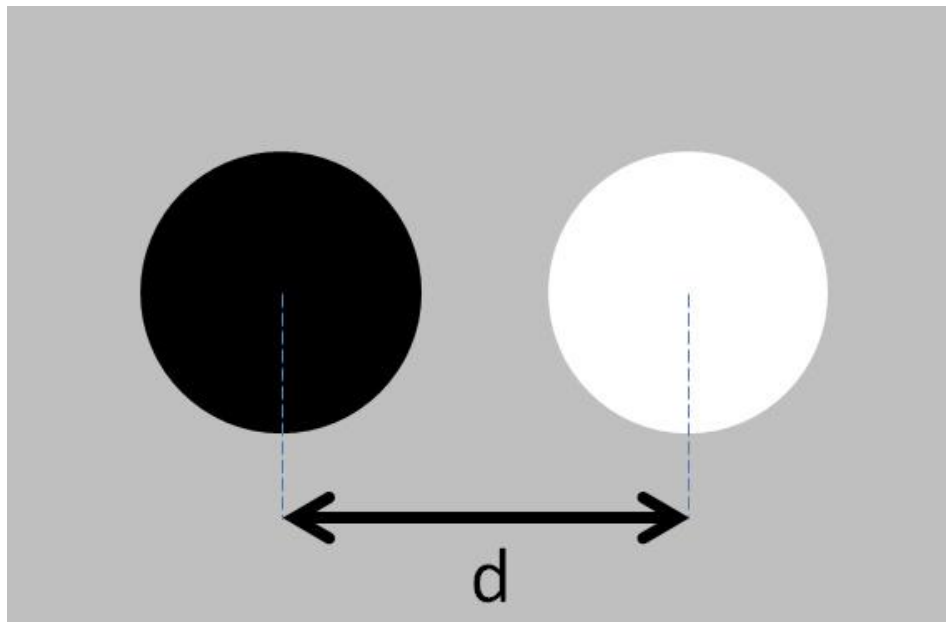


Figure 47: Model of a vessel affected by the chemical shift artifact
The vessel signal is shifted to the right and overlaid onto the homogenous background signal. A black and a white circle result.

We can take advantage of that behavior, because the chemical shift displacement is well-known for a given field strength and read-out bandwidth.

A filter kernel, i.e. a function to be convolved with the image, that creates strong positive response for such dark and bright structures separated by a defined distance is represented in Figure 48.

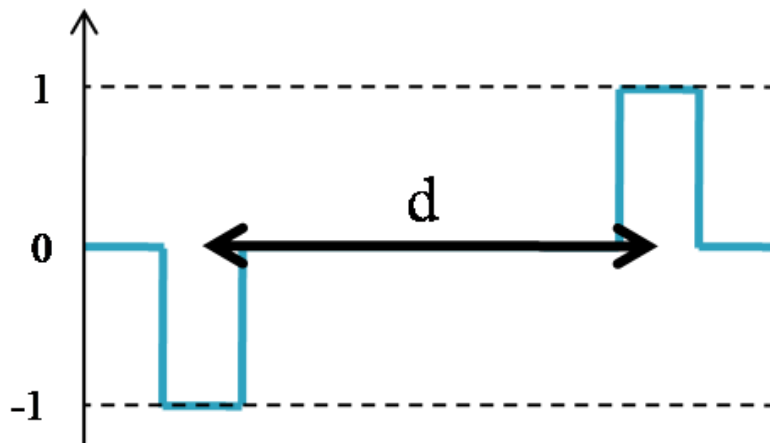


Figure 48: The chemical shift filter kernel

The filter kernel assumes a hypointense structure displaced by a distance d from a hyper-intense structure.

Let us assume a vessel of just one pixel in diameter and a chemical shift of 2 pixels. The signal intensities of an image line containing the vessel (2) and the black hole (0) it leaves in the background (1) can be written as $[1, 1, 0, 1, 2, 1, 1]$. Convolution with the corresponding filter kernel $[-1, 0, 1]$ gives $[0, -1, 0, 2, 0, -1, 0]$. The strongest positive response is obtained at the center position between the black and the white structure ($x=0$). Negative side lobes appear at $x = -d$ and $x = +d$. In order to get a single white spot at the position of the original hyper-intense vessel signal, all negative values are replaced by "0" and the filtered image is shifted by $d/2$ in positive direction, this results in $[0, 0, 0, 0, 2, 0, 0]$. For two dimensions, the procedure is illustrated in Figure 49.

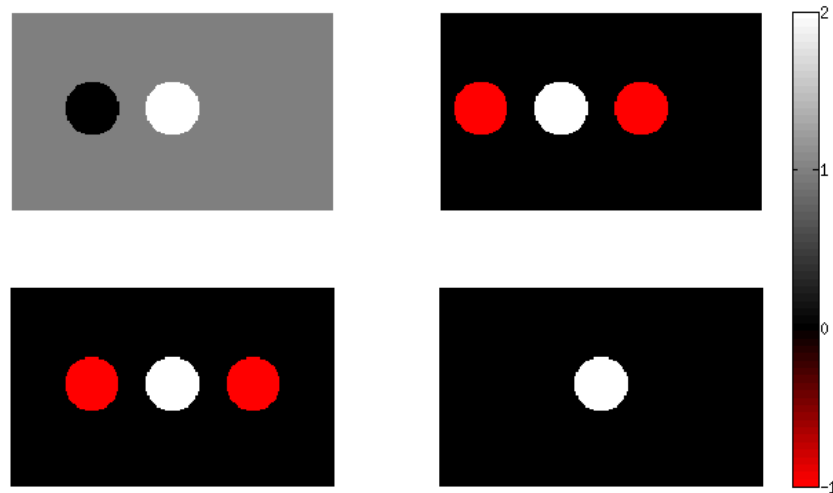


Figure 49: Processing steps of the chemical shift filtering technique

Top left: The original model of a shifted vessel on a homogenous background as in Figure 47.

Top right: The chemical shift filter kernel is applied. A positive filter response is obtained at the center between the original black and white circles, two negative side lobes appear.

Bottom left: The whole image is shifted to the right by $d/2$ to overlap the positive filter response with the position of the white circle in the original image.

Bottom right: Negative values are replaced by zeroes and only the bright vessel structure remains.

For vessels smaller than the chemical shift, the hypo-intense and hyper-intense structures are separated. For larger vessels, however, there is an overlap resulting in some artifacts:

For vessels with diameters between 1 and 1.5 times the chemical shift, the shape of the overlap is visible with lower signal intensity on both sides of the white circle in the filtered images. This artifact was observed in some data sets containing large vessels (see Figure 50 and Figure 51).

For vessels larger than 1.5 times the chemical shift, a lens-shaped black hole is appearing in the filtered image where the overlap structures overlap again. Strongest contrast enhancement is found on the left and on the right side of the original circle, in the direction perpendicular to the chemical shift. Such large vessels were not present in any of the data sets of this work.

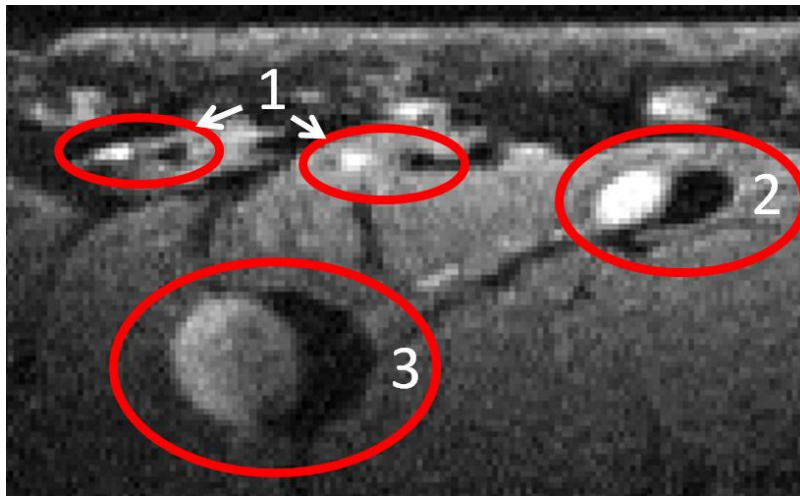


Figure 50: Different ratios of vessel diameter vs. chemical shift in vivo

The chemical shift is $\approx 900 \mu\text{m}$ in this image. Vessels marked with "1" are significantly smaller than the chemical shift, vessel "2" is the same size as the chemical shift, vessel "3" is approximately 1.5 times larger.

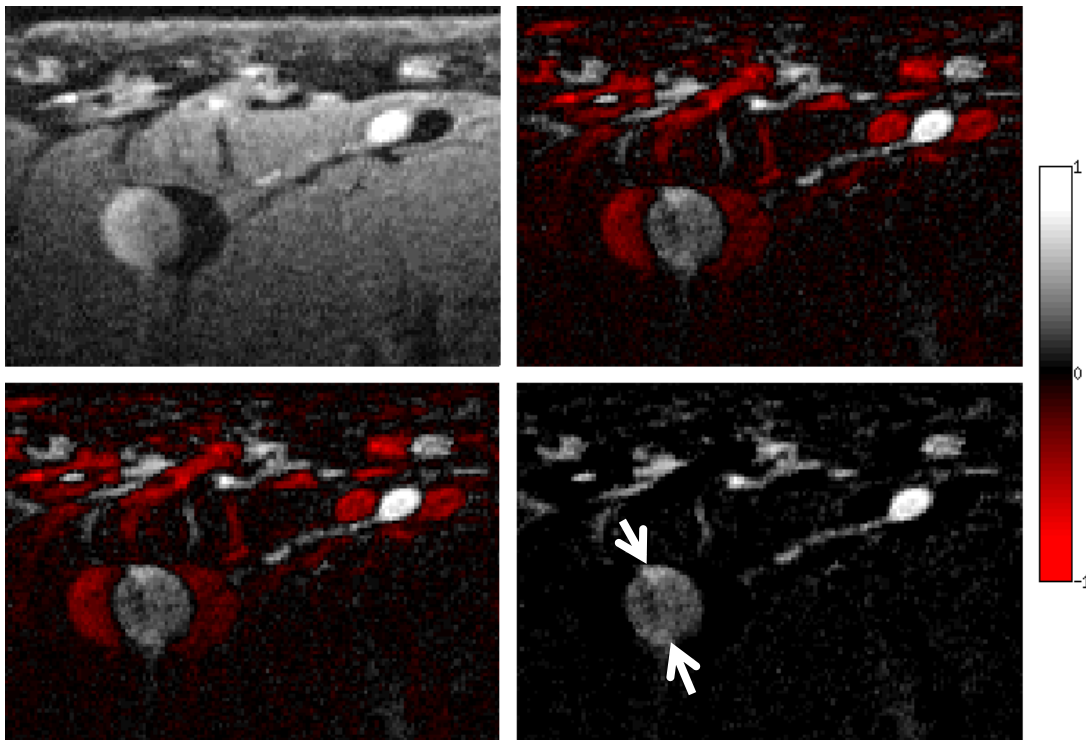


Figure 51: Chemical shift filter procedure applied on in vivo data

The same steps as described in Figure 49 are applied. The contrast enhancement of water structures and the two negative lobes (red) can be seen. The artifact for vessels larger than the chemical shift is observed (white arrows).

A simulation of the filtering result for vessel diameter/chemical shift ratios from 0 to 3 is shown in Figure 52. It can be seen, that the technique works flawlessly for vessels smaller or equal the chemical shift. Artifacts as described above occur with larger vessels.

From this simulated data, the SNR and CNR of the filtered vessels was compared to the unfiltered version. The results are plotted in Figure 53 and Figure 54.

SNR is increased for vessels smaller than 1.5 times the chemical shift. The gain for high SNR scenarios is around 22%, for a realistic value of SNR = 10, the gain is still between 15 and 20%.

CNR is increased by 100% for noise-free images, with an SNR of 10, the mean gain in contrast-to-noise ratio is between 80 and 90%. The further increase in CNR for vessels with diameter larger than twice the chemical shift is due to the fact, that in the original images, the vessel signal is only seen as a hyper-intense crescent moon. The rest of the circle has the same signal intensity as the background, i.e. the original contrast of the vessel is very low, explaining the even higher gain in contrast after filtering.

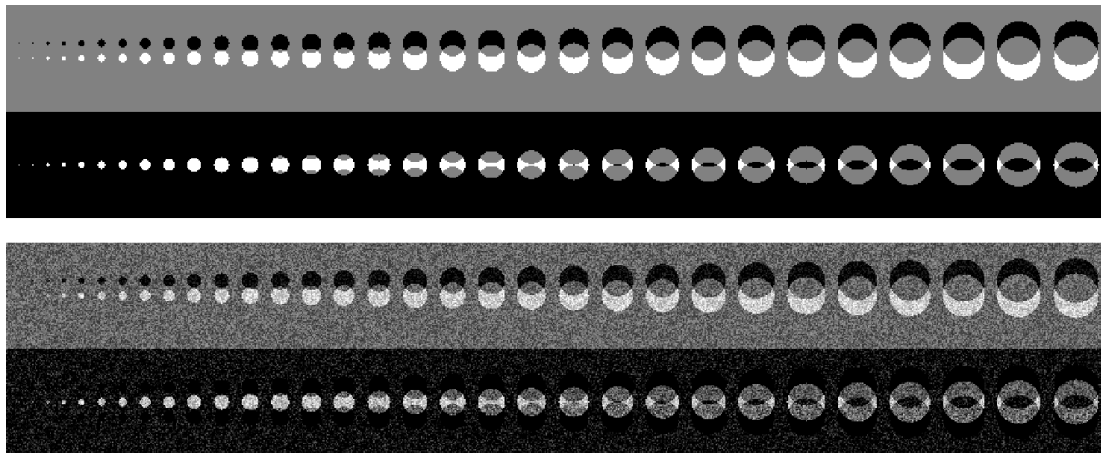


Figure 52: Simulated vessel data for evaluation of chemical shift filter
Vessels with diameters of 1 pixel to 3 times the chemical shift width were used for simulation. For vessels larger than the chemical shift, artifacts occur (see text for description). The top image is noise free, the bottom image shows a data set with a realistic SNR value of 10.

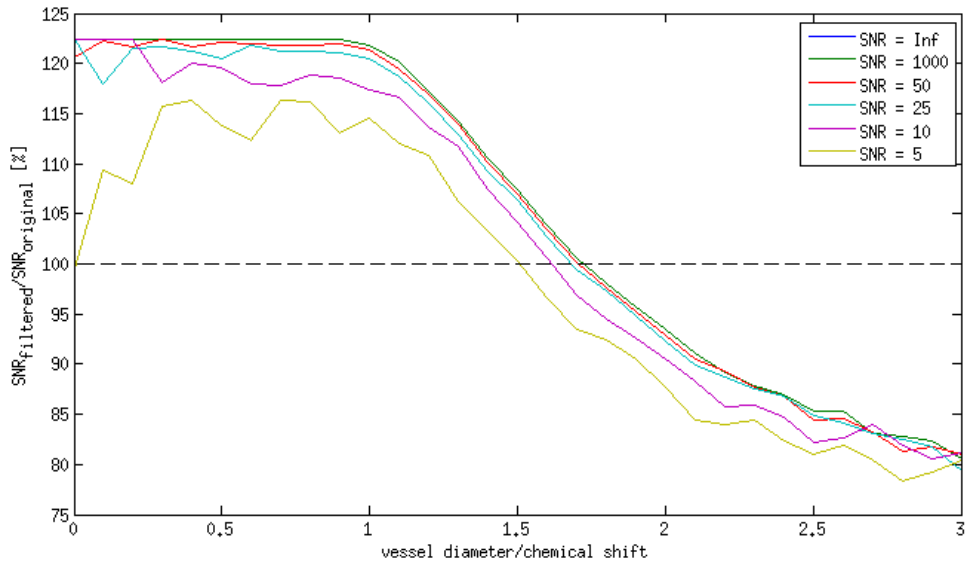


Figure 53: Impact of chemical shift filter on vessel SNR

SNR of the vessels increases by filtering, as long as the vessel diameter is smaller than ≈ 1.5 times the chemical shift between water and fat. The gain is slightly higher for low noise conditions, for realistic SNR values around 10, as achieved in the studies within this thesis, almost the full gain can be obtained.

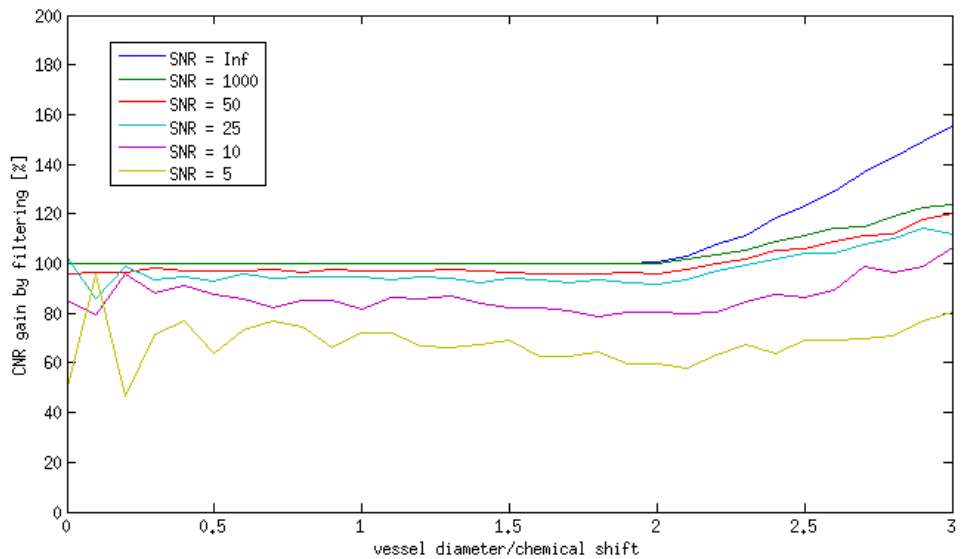


Figure 54: Impact of chemical shift filter on vessel CNR

For vessel diameters up to twice the chemical shift, constant CNR gain for a given noise level in the original image is obtained.

The gain decreases with increasing noise level.

For realistic SNR values of around 10, the gain in the simulated data is $\approx 85\%$.

4.2 VESSEL SEGMENTATION

4.2.1 Manual segmentation

Vessels were segmented using MRicro [105], a tool for visualizing 3D data in analyze format (.hdr+.img files). The program provides a tool for drawing of ROIs and several helpful features such as automatic selection of 3D ROIs with lower and upper thresholds and morphological operations such as opening and closing. Vessels were segmented based upon the original images with transparent overlay of the chemical shift filtered images. ROIs were drawn on the hyper-intense vessel signals on each slice, usually first on slices parallel to the skin surface. Then, ROIs were refined in the transversal slices. The refinement was repeated for the third direction to ensure continuous 3D vessel geometry. The procedure was iterated until a satisfactory result was obtained. For the experienced user, one data set took about 2-3 hours.

4.2.2 Calculation of vessel diameter

The vessel diameters were calculated using the distance transform of the segmented vessel tree. The distance transform maps the distance of any given voxel to the nearest non-vessel voxel.

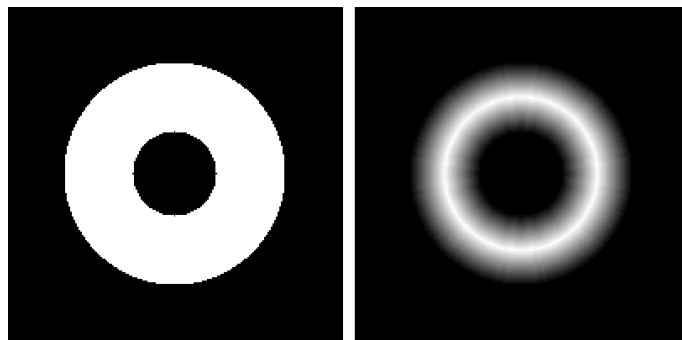


Figure 55: Demonstration of the distance transform

The object on the left is a white ring on a black background. The distance transform gives the distance of each voxel to the closest background voxel. The distance transform value at the center of the structure (i.e. at the position of the skeleton (see section 4.3.2) can be interpreted as half the width of the ring. For vessels this would correspond to the radius.

4.3 EXTRACTION OF QUANTITATIVE VESSEL PARAMETERS

In order to calculate quantitative parameters from the segmented vessel tree, it is beneficial to represent the vessel tree as a graph (see Figure 56). This way, the geometrical structure of the vessel tree and its properties can be represented by nodes (junctions of vessels) and edges (vessels). Characteristic branching behavior can then be statistically assessed.

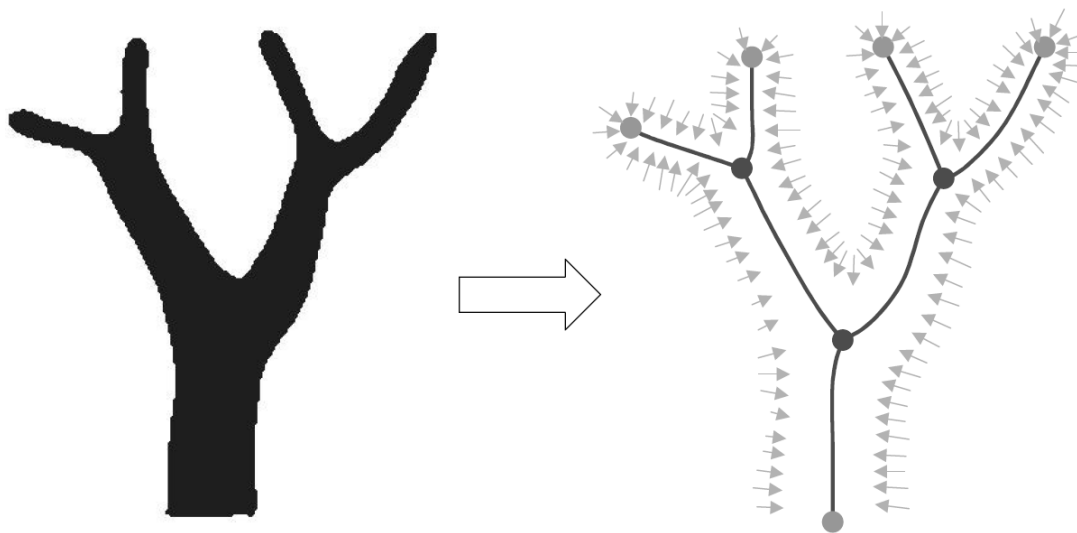


Figure 56: Representation of a vessel tree as a graph

The segmented model of the vessel tree is thinned and transformed into a graph represented by nodes and edges (from [116]).

4.3.1 Graph theory

A graph is a mathematical entity describing the pairwise relations between a set of points. In graph theory, points are called 'vertices' or 'nodes', their connections are called 'edges'. Graphs are usually described by their adjacency matrix, i.e. a matrix that contains a non-zero entry at position (i,j) if vertices i and j are connected. The most common way to display a graph is drawing a dot for each vertex and a line for each edge connecting two vertices. The way how

dots and lines are drawn is considered irrelevant, only the information of which pairs of vertices are connected is important. A simple example of a graph and its corresponding adjacency matrix is given in Figure 57.

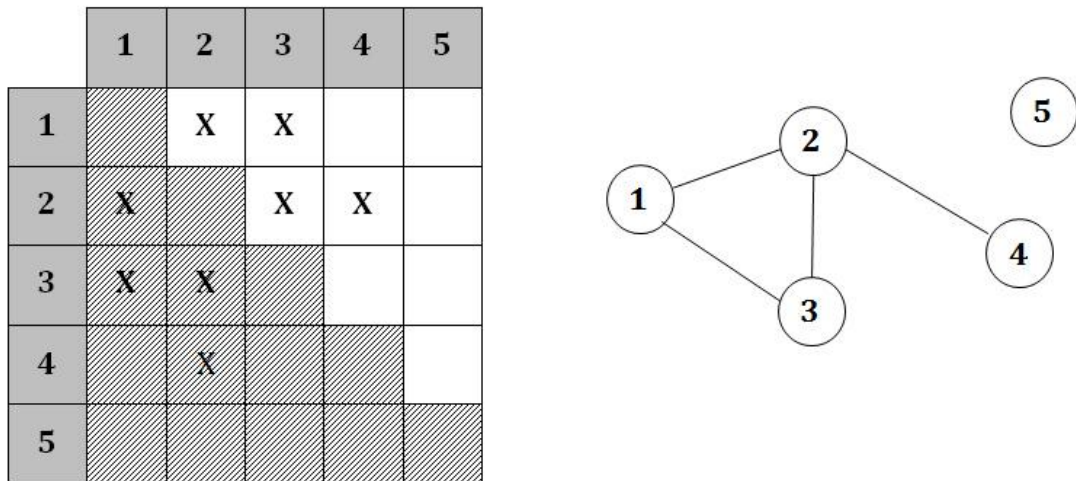


Figure 57: Example of an adjacency matrix and its corresponding graph
 An 'X' in the adjacency matrix table means that there is a connection between the elements designated by row and column number.

In the following, a summary of basic nomenclature and definitions relevant in graph theory is given [116, 117].

- A graph G is a pair $G = (V,E)$ from a finite non-empty set V and a set E of two-element subsets of V . The elements of V are called nodes (or points or vertices), the elements of E are called edges. For an edge $e = \{a,b\} = \{b,a\}$, a and b are end-nodes of e .
- An edge e is incident to nodes a and b , if edge $e = \{a,b\}$ or $e = \{b,a\}$ exists.
- Two edges are called adjacent if both edges are incident to the same node.
- Two nodes are called adjacent if there is an edge connecting them.
- An edge sequence is a sequence of edges $e_i = \{v_{i-1},v_i\} \in E, i = 1, \dots, n$ with nodes $v_j \in V, j = 0, \dots, n$. If v_i are pairwise different, the sequence is called a path. Nodes v_0 and v_n are called start point and end point.

- Two nodes a and b are called connectable if there is an edge sequence with start point a and end point b .
- If all nodes of a graph are pairwise connectable, G is called connected.
- A tree is a graph G , which is connected and acyclic.
- A node which has only one edge is called a leaf.
- A weighted graph is a graph whose edges are assigned one or more measure numbers.

4.3.2 Skeletonization

The first step towards graph representation of the vessels is the extraction of the vessel tree's skeleton, i.e. the "middle line" of the vessels. "Skeletonization" or "thinning" refers to an algorithm which is applied to a binary data volume eroding the object layer by layer until only a skeleton is left. This binary data volume is the 3D segmented vessel tree represented as 1's on a background of 0's. The remaining skeleton should preserve the connectivity and topology of the original object.

4.3.2.1 Preservation of connectivity

Preservation of connectivity means that the skeleton should not contain more separated (non-connected) objects than the original dataset, this is mathematically well-defined. Connectivity is defined as the 26-neighborhood in our case (cf. Figure 58).

Two points p and q are called 26-connected if the following condition for the distance d between p and q holds:

$$[\text{Eq. 56}] \quad d = \sqrt{(p_x - q_x)^2 + (p_y - q_y)^2 + (p_z - q_z)^2} \leq \sqrt{3}$$

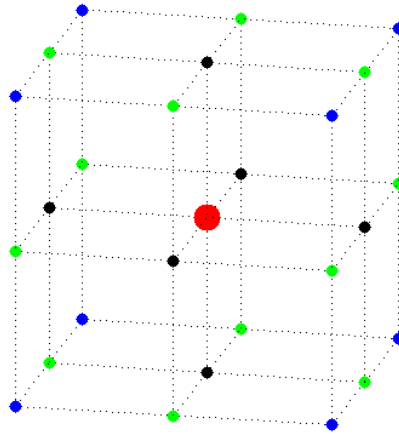


Figure 58: The 26-neighborhood of a point p
 p (red) is 6-connected to black points ($d = 1$), p is 18-connected to black and green points ($d \leq \sqrt{2}$), p is 26-connected to all shown points ($d \leq \sqrt{3}$).

4.3.2.2 Preservation of topology

Preservation of topology states that “d”-shaped objects should not be reduced to “o”-shaped skeletons for instance. Mathematically topology or geometry preservation is less accurately defined, different approaches were proposed [118, 119]. Usually topology preservation is achieved by preservation conditions for certain points, such as endpoints of a unit-width arc.

Conservation of both geometry and connectivity is especially non-trivial in 3D datasets. The thinning algorithm used in this work is based on a fully parallel 3D thinning algorithm originally published by [118] and improved by [120]. The approach is template-based and provides a set of so-called “deleting templates” of size $3 \times 3 \times 3$. These templates are compared to $3 \times 3 \times 3$ subvolumes around a subset of object points in the dataset and define whether or not the object point in the center of the subvolume can be deleted from the dataset without losing the object’s connectivity. The subset of object points to be checked is defined by identifying all voxels that have at least one 26-adjacent background point, i.e. the voxel should be at the object surface. Secondly, the

voxels must not be a so-called tail point. Tail points are either voxels that have only one 26-adjacent object point, i.e. they are endpoints of a line, or they have exactly two 26-adjacent neighbors that fulfill some additional criteria (for details refer to the original article [120]).

Figure 59 shows an example subset of the 66 deleting templates. If the data subvolume matches the pattern of any of the deleting templates, the central point p will be deleted.

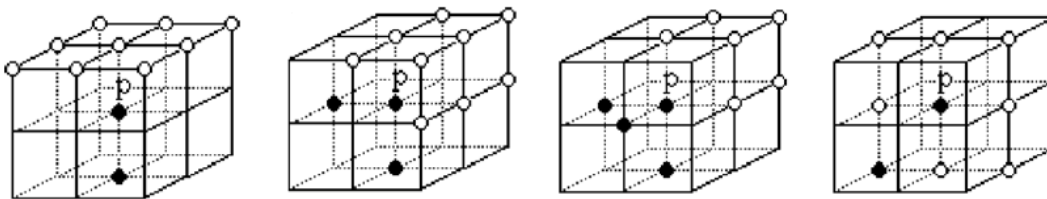


Figure 59: Example subset of the 66 deleting templates

Black points represent object points, white points represent background points, no point means that the image point at that position can be either an object point or a background point. If the data subvolume matches this pattern, the center point p is deleted. (from [120])

The algorithm can be described by the following pseudo-code:

Repeat

Mark every object point which is 26-adjacent to a background point

Determine tail points

Repeat

Simultaneously delete every marked, but non-tail point which matches at least one of the deleting templates

Until no point can be deleted

Release all marked but not deleted points

Until no marked point can be deleted

The algorithm was implemented in MATLAB 7.4. Figure 60 shows a screenshot of the graphical output of the program during execution. On the right hand side of the image, the vessel tree to be skeletonized is displayed. Points to be deleted are marked in green, all other points are black. On the left, the number of deletable, marked, line end and near line end points over the number of iterations is displayed.

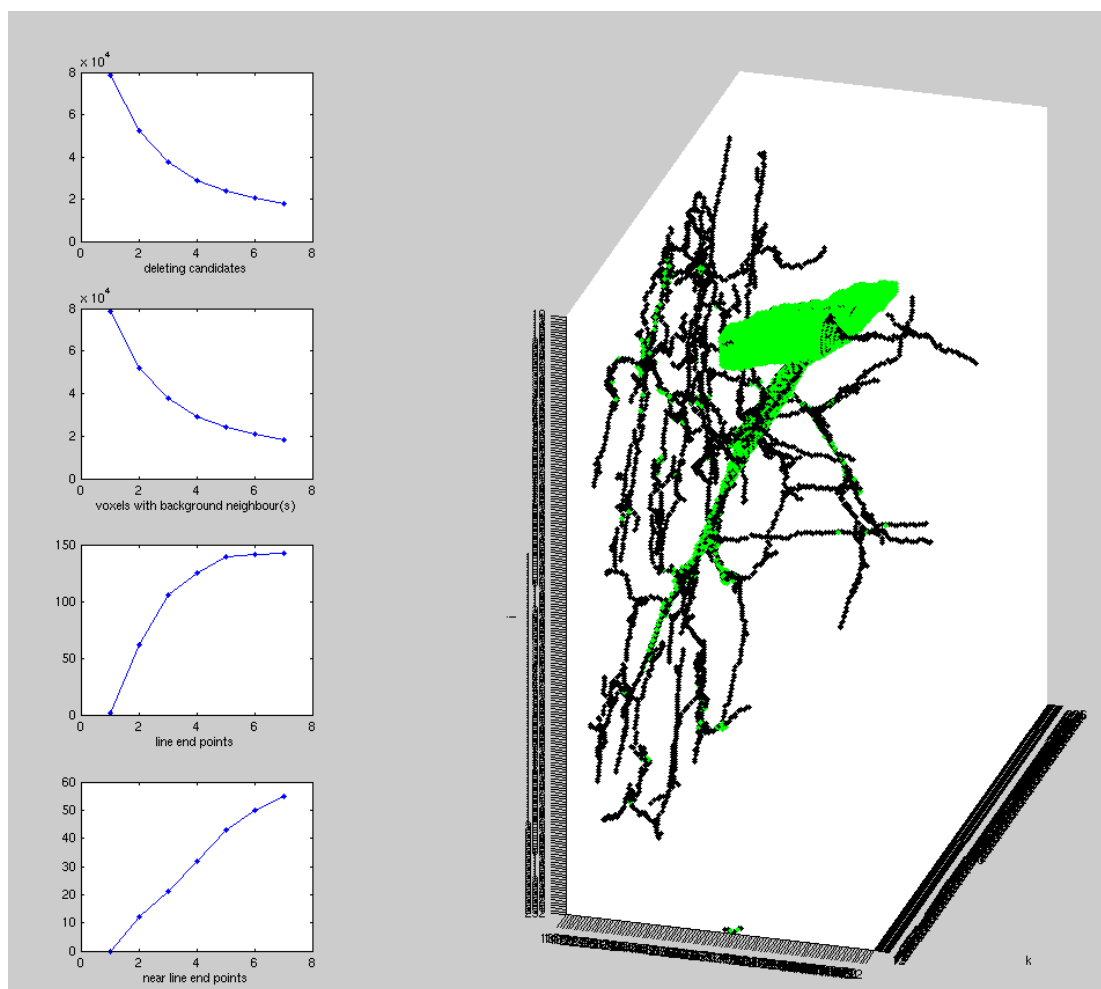


Figure 60: Screenshot of the MATLAB program performing skeletonization Deleted voxels are displayed in green, all others are black. The plots on the left side give information about the number of deletable, marked, line end and near line end points.




4.3.3 Graph from skeleton

Graphs are a well-suited mathematical means to represent vascular structures. For a theoretical overview on graphs please refer to section 4.3.1 and the pertinent literature (e.g. [117]). End nodes of the graph stand for roots and ends of a vessel tree, all other nodes and edges describe the branching structure of the vascular system. The transformation into a graph relies on the vessel system's skeleton described in section 4.3.1. The algorithm performing this transformation must include the following steps:

- Classification of skeleton voxels (see section 4.3.3.1). This procedure identifies each skeleton voxel being an end node, junction or edge. Redundant graph edges are subsequently removed and only relevant edges are kept, maintaining the vessel system's topological structure.
- Identification of neighboring edges (graph reduction, see section 4.3.3.2). Neighboring edges are combined, i.e. the number of nodes is reduced until only end nodes and junctions are left.

4.3.3.1 Node classification schemes

A graph can be derived from the vessel skeleton by interpreting each skeleton voxel as a node and 26-connectivity between two skeleton voxels as an edge between those two voxels. Each node is assigned its x , y and z coordinates from the original image for better identification. Graph based representation of skeletons has been discussed in [116, 121-124]. The four first methods use the following simple classification scheme for the graph's nodes. The symbols at the end of each line are used to identify the corresponding type of node throughout this work.

- Nodes with only one neighbor are labeled as *end voxels* 
- Nodes with exactly two neighbors are labeled as *edge voxels* 
- Nodes with more than two neighbors are labeled as *junctions* 

This classification scheme only works for very simple cases of skeletons. In virtually every skeleton derived from image data, it fails, because they deliver

non-unique classification at junctions. This results in too many edges leading to circles, as can be observed in Figure 61A. Circles in the graph are topologically equivalent to holes in the object and thus the topology of the original vessel tree is altered.

The abovementioned graph representation algorithms have different approaches in handling these ambiguities, which will be briefly described:

Lee et al. [122] search for voxels having three neighbors are labeled as “T”-junctions, all voxels with 4 neighbors are “X”-junctions. In order to avoid neighboring junctions, they suppress the classification as junction voxel for all 26-adjacent neighbors of “T”- or “X”-junction nodes. The drawback is, that one junction might be misinterpreted as two separate junctions (cf. Figure 62a).

Soler [123] classifies all voxels according to the rules above and replaces all adjacent junction nodes by one junction node positioned at the geometric center of all previous junctions positions. All edges leading to one of the replaced nodes will be connected to the center node. This technique fails to represent multiple junctions that are close to each other, but not the same (cf. Figure 62b).

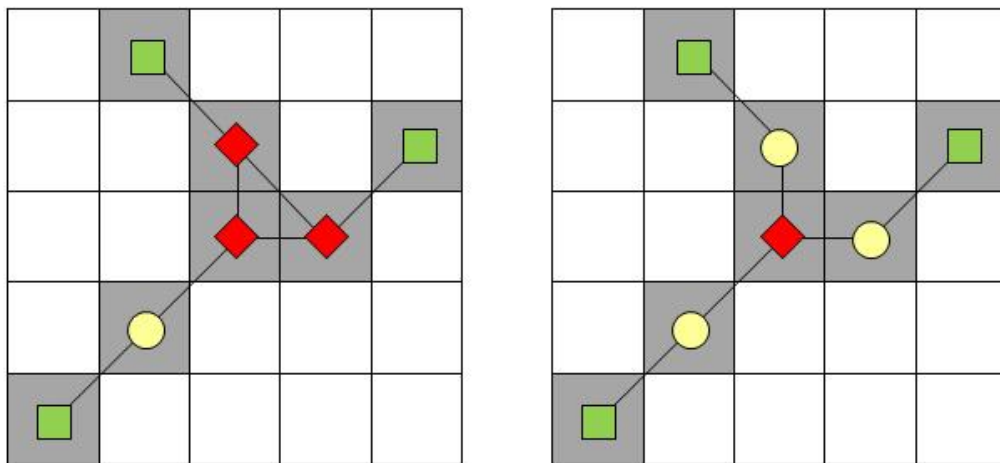


Figure 61: Example of a junction where standard node classification fails

Grey boxes represent skeleton voxels.

Left: multiple nodes are classified as junction nodes resulting in a circle in the graph due to the presence of redundant edges.

Right: one possible solution.

Gerig et al. [121] use a raster-to-vector transformation eliminating redundant edges in the neighborhood of a single given voxel. Redundant edges are identified using the adjacency information of that voxel. The problem is that some configurations cannot be resolved, as can be seen in Figure 62c.

Selle [124] describes an algorithm engaging optimization measures such as the sum of distances to neighboring redundant edges to identify which redundant edges should be removed. It turns out that this technique fails to remove circles in certain configurations as well (Figure 62d).

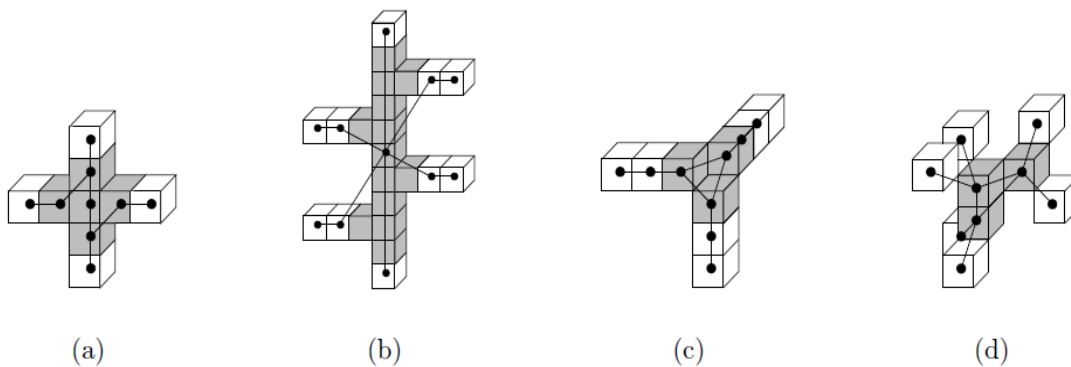


Figure 62: Existing schemes to represent a skeleton as a graph

Four schemes that all have fundamental issues in correctly transforming a skeleton into a graph.

(a) Lee et al. [122], one junction becomes two, (b) Soler [123], multiple junctions are joined into one, (c) Gerig et al. [121] and (d) Selle [124], some arrangements cannot be solved, redundant edges remain. (from [116])

To circumvent the problems associated with the methods describe before, Schöbinger [116] presented another algorithm to solve the graph representation issue, which was implemented in this work. It is characterized by the following steps:

- Node classification
- Determination of a starting point
- Traversing of the skeleton
- Labelling (of coordinates and diameters)

The algorithm also classifies the voxels according to the categories described at the beginning of this section, but introduces a fourth category called *transition voxels*. All voxels that are not junctions, but are 26-connected to a junction are classified into that category, i.e. these are the voxels immediately leading to a junction.

The starting point is chosen as the end point with the largest diameter, as derived from the distance transform described in section 4.2.2. This point should correspond to the root of the vessel tree. Traversing of the graph means that the algorithm follows the connections from the starting point according to neighborhood relations. The path of the vessel is followed, until a transition voxel is found. Now the ambiguity of the junction will be solved.

To this end, the set of junction or transition voxels that are connected to the first found transition voxel by either a junction or a transition voxel is stored. This set is considered as an undirected sub-graph with the elements of the set representing the nodes of the graph. The edges are obtained from the neighborhood relationship between these nodes and are labeled according to the type of neighborhood (face-neighbor $d=1$, edge-neighbor $d=\sqrt{2}$, or corner-neighbor $d=\sqrt{3}$).

For the reduction of redundant edges, corner connections will be deleted if a redundant edge connection exists, and edge connections will be deleted if redundant face connections exist. This is achieved by assigning weighting factors to the edges according to their type and checking for redundancy in this priority order.

An edge is redundant, if it can be deleted without separating the connected graph into two sub-graphs. This criterion can be easily checked by a graph depth search and counting of the elements. When all voxels of the set have been checked for redundancy, the junction is solved and the traversing continues at the adjacent branches of the junction until the next transition voxel is identified. The procedure is continued until all voxels are traversed.

Finally, each node is assigned its coordinates in voxel space and its diameter as derived from the distance transform demonstrated in 4.2.2. The distribution of vessel diameters is calculated in this basis.

4.3.3.2 Graph reduction

In the last step, the simplified graph (as in Figure 63C) is reduced by eliminating chains of normal line nodes and replacing them by an edge directly connecting only end points and junctions. These edges are assigned the sum of distances between all normal line nodes that have been deleted for this branch, i.e. giving the total length of the branch. From this information, the distribution of branch lengths within a vessel tree can be obtained.

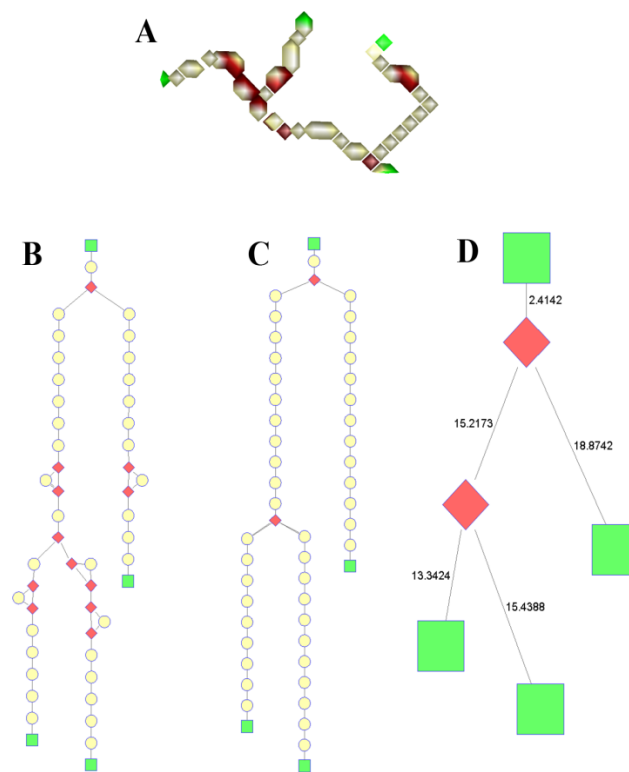


Figure 63: Steps from the skeleton to the reduced graph

A subvolume of a real vessel data set

■ endpoints, ● normal line points and ◆ junctions. A: Colored 3D rendering of skeleton, B: 'raw' graph, C: 'refined' graph. D: 'reduced' graph, the accumulated length of the branches is given in voxel dimensions. The structure of the original skeleton can easily be recognized in its representation as a graph.

4.4 SOFTWARE

4.4.1 MATLAB

Most of the algorithms in this work have been implemented in MATLAB due to its versatility and the big number of openly available code. MATLAB version 7.4 was used throughout the thesis. MATLAB is a product of The MathWorks, Inc., Natick, MA, U.S.A.

4.4.2 MeVisLab

MeVisLab Version 2.0 is a cooperative project of MeVis Medical Solutions AG (Bremen, Germany) and Fraunhofer MEVIS – Institute for Medical Image Computing (Bremen, Germany). This GUI¹-based software allows to graphically assemble image processing pipelines using compiled C++ modules from the ITK and VTK toolkits (see next section). MeVisLab provides elaborate methods for 3D visualization of data.

4.4.3 ITK/VTK

ITK and VTK stand for Insight Toolkit [125] and Visualization Toolkit [126], respectively. These toolkits are a collection of open source and cross-platform C++ code dedicated to image segmentation, registration and visualization.

4.4.4 MRicro

MRicro [105] is a free tool for displaying Analyze format (.hdr+.img) datasets. The program was used in this thesis to manually segment the vascular trees.

¹ Graphical User Interface

5 **DISCUSSION AND CONCLUSIONS**

5.1 DISCUSSION

5.1.1 Study I: 12 mm HTS surface coil at 1.5 T

The geometry for an auto-resonant multi-turn transmission line resonator made of high temperature superconducting material has been calculated using a semi-analytic approach and a MATLAB toolbox developed during this thesis.

The high quality factor of the resulting superconducting coil, together with the low-noise receiver chain, allows very high SNR and thus high spatial resolution at short measurement times using a clinical 1.5 T MR scanner. The sample's contribution to total noise is 5-6 times greater than the coil's, meaning that coil size could be reduced even further if the FOV allows.

Transmission of the excitation pulse by inductive coupling of the HTS coil to the body coil is advantageous, because the quality factor of the HTS coil decreases with the rising number of normal conducting flux vortices at higher current densities. This leads to a reduction of coupling to the body coil at high power levels and automatically avoids destruction of the coil. This could allow for ultra-short pulses for, e.g., magnetization transfer or multi-quanta measurements.

Images with isotropic resolution of 100 μm and 80 μm , respectively, as well as images with 20x60 μm^2 in plane resolution have been acquired with SNR values of 10-15 for the highest resolution scans, i.e. 0.5 nL voxel volume, and 20-40 for voxel volumes of 1 nL.

The complex handling of the cryogenic device prevents the technique from being used in clinical routine; therefore a cooling system based on a pulsed tube refrigerator is under investigation at IR4M in Orsay, France.

5.1.2 Study II: 15 mm surface coil at 3 T

It has been shown that imaging of human skin in vivo with isotropic resolution of 100 μm is feasible at reasonable scan times with a small normal conducting copper surface coil at 3 T.

Provided high isotropic resolution, cutaneous vasculature can be extracted. Small vessels with diameters down to 100 μm are well delineated. SNR of skin layers and vessels, and CNR of the vascular system with regard to surrounding tissue, have been shown sufficient for manual segmentation of the vascular tree, even without contrast agent.

The strong chemical shift artefact is not a limitation for vessel detection; it rather helps improving visibility of the vascular system. This is due to the fact that most of the vessels are embedded in adipose tissue. The shifted vessel signal is added onto a homogenous background and, therefore, appears even brighter, opening the possibility to use elaborate post-processing such as chemical shift filtering. Hence, fat suppression is not required in this case.

At such high spatial resolution, subject motion during and between acquisitions is one of the limiting factors for good image quality. We did not observe any obvious blurring due to motion during scans. We therefore conclude that using good subject fixation efficiently limits motion during acquisition and no additional correction scheme is necessary, as reported previously [68]. However, between scans, shifts in the subjects' position of several voxels were observed. We attribute this to unconscious relaxation of the subjects after the scanner noise stopped. We have shown that such motion can be reliably corrected for by image realignment.

5.1.3 Study III: 6 mm surface coil at 7 T

The geometry for a prototype of a 6 mm surface coil for ^1H imaging at 7 T has been calculated. The structure was produced by our cooperation partners in Orsay by deposition of copper on a flexible Kapton® substrate.

In a pilot study, imaging experiments of the human skin *in vivo* were performed at 7 T by inductively coupling the small coil to a larger surface coil. Images with an isotropic resolution of 100 μm were obtained in less than 4 minutes and resulting skin structures are well delineated.

A dedicated small pick-up coil replacing the 9 cm coil should be implemented for improvement of signal reception. Furthermore, the receive

coil should be passively decoupled during transmission with crossed diodes to allow for more homogeneous excitation with a separate coil, e.g. a volume coil or another larger surface coil.

5.1.4 Image processing

Dedicated post-processing techniques were developed for better interpretation of the micro-imaging results obtained throughout this work.

Image SNR could be further increased by averaging multiple scans after realignment, which successfully corrected for motion occurring between two consecutive scans.

To facilitate manual vessel segmentation, a chemical shift filtering technique has been proposed that relies on the displacement of water with respect to fat signal at low read-out bandwidths, as used for high resolution imaging experiments. The contrast of the vessel system, as compared to the tissue background, could be significantly improved.

Graph theory and techniques of digital topology were employed to extract quantitative parameters from the segmented vascular trees including skeletonization and creation of graphs. Applying this technique to the data of the 3 T study, within a group of nine healthy volunteers, consistent results were observed for diameter and branch length distributions, potentially useful for diagnosis of small vessel diseases of the skin.

5.2 CONCLUSIONS AND PERSPECTIVES

The trend in MR research goes towards higher field strengths and more and more channels for signal reception to enable the use of coil arrays with an ever increasing number of (smaller) elements. Currently, the number of elements typically ranges between 8 and 32, although up to 128 elements have been used in prototypes [127]. Correspondingly, element size/diameter varies between > 10 cm down to a few cm. At this end, MRI is comparable to current EEG (64 channels) and MEG (128 channels) systems. This effort for more and more channels is driven by the need to increase sensitivity and/or enable parallel imaging to reduce measurement times.

Up to now only a few sites worldwide have installed a 7 T whole-body scanner, among which the scanner at the MRCE in Vienna is the only such system in a clinical environment. Due to its novelty, adequate hardware solutions and RF pulse sequences adapted to the high field strength are among the most discussed and researched issues in the international high field MR community.

Since the greatest limitation of the techniques presented is the limited FOV and penetration depth, a coil array consisting of very small individual elements would be of substantial benefit, providing both its single elements' sensitivity and the larger FOV accessible with standard coils and, in addition full flexibility to design geometrically adapted arrays. Imaging at higher field strengths, e.g. 7 T, will further increase sensitivity allowing for even higher spatial resolution or shorter acquisition time. An application for an international grant on this matter has been submitted during the course of the thesis in collaboration with IR4M in Orsay, France.

Specificity and sensitivity for detection of venous vessels could be enhanced by applying susceptibility-weighted imaging techniques [128, 129] to benefit from the additional phase contrast.

With a larger cohort of subjects, the quantitative parameters for healthy vasculature could be confirmed and a distinction from pathological skin vessel trees could be realized. Also, the comparison of vascular parameters at the same anatomical location in the course of treatment might be monitored individually and non-invasively.

Observation of the cutaneous vessel tree with high resolution MRI can help in various dermatological diseases demanding information about dermal vasculature. In inflammatory diseases of skin vessels such as vasculitis, characterisation of affected vessels would help identify such disorders at an early stage and, potentially, improve staging. Due to the non-invasiveness of the method, therapeutic effectiveness could be demonstrated in longitudinal studies.

Another application could be pre-therapeutic assessment of vascular malformations (birthmarks). Despite highly sophisticated therapeutic devices, results often remain unsatisfying. The relation of vascular architecture to therapeutic outcome is uncertain due to a lack of non-invasive, pre-therapeutic assessment methods.

In cutaneous tumours (cutaneous melanoma, squamous cell carcinoma), neo-angiogenesis facilitates tumour cell proliferation via vasculature. Monitoring the vascular system in the evolving tumour's vicinity could shed new light on the biology of malignant cutaneous tumours and offer the opportunity for new treatment modalities. The efficiency of drugs targeted directly at tumour vascularisation could be evaluated without interference with the treated region.

Also, MR microimaging could provide a tool for prior evaluation of the most suitable location for biopsy, and help identify the position of the most interesting slices for histology within a biopsy. Currently, the image quality and contrast achieved in small samples in vivo and, even more ex vivo, might open a window towards 3D "MR histology".

6 ANNEXES

6.1 SEMI-ANALYTICAL MODEL FOR SIMULATION OF MTLRS

The resonance condition for split-conductor transmission line resonators on a substrate with dielectric constant ϵ and the speed of light c is given by [130]

$$[\text{Eq. 57}] \quad \frac{\Lambda\omega}{4Z_0} \tan\left(\frac{\omega Z_0 \sqrt{\epsilon} l}{4c}\right) = 1$$

The results based on the following equations are substituted into the resonance condition; its solution provides the resonance frequency ω of multi-turn transmission line resonators [54].

The equivalent inductance Λ of the resonator is calculated as the sum of inductances of the individual circular components L_i (the contribution of the small connecting lines between the circles is neglected) plus twice the mutual inductances between coplanar loops M_{pp} and parallel-plate loops M_{pq} .

$$[\text{Eq. 58}] \quad \Lambda = \sum_{i=1}^N L_i + 2 \sum_{p=1}^N \sum_{q=p}^N M_{pq}$$

The inductance of the i^{th} circular loop is

$$[\text{Eq. 59}] \quad L_i = \frac{\mu_0 d_i}{2} \cdot \left[\ln\left(\frac{4d_i}{w}\right) - 0.5 + \frac{1}{24} \left(\frac{w}{d_i}\right)^2 \cdot \left(\ln\left(\frac{4d_i}{w}\right) + \frac{43}{12} \right) \right]$$

and the mutual inductance between loops p and q is

$$[\text{Eq. 60}] \quad M_{pq} = \begin{cases} \frac{\mu_0}{2} \frac{r_1 r_2}{w d^2} \int_0^{2\pi} [\varphi(h) - \varphi(w+h)] \cos\theta \cdot d\theta & \text{for } p=q \\ \mu_0 \sqrt{g_p g_q} \left[\left(\frac{2}{k} - k\right) F(k) - 2E(k) \right] & \text{for } p \neq q \end{cases}$$

$F(k)$ and $E(k)$ are the elliptic Legendre integrals of the first and second kind, respectively, and

$$\begin{aligned}
 r_1 &= \frac{d+h}{2}, \quad r_2 = \frac{d-h}{2} \\
 \varphi(x) &= x \ln \left(\frac{x}{\delta} + \sqrt{1 + \left(\frac{x}{\delta}\right)^2} - \sqrt{x^2 + \delta^2} \right) \\
 \delta^2 &= r_1^2 + r_2^2 - 2r_1r_2 \cos \theta \\
 g_i &= \left(d_i + \frac{w}{2} \right) \cdot \frac{d_i + \frac{w}{2} - 2wd}{d_i + \frac{w}{2} - wd}
 \end{aligned}$$

[Eq. 61]

The characteristic impedance Z_0 of parallel-plate transmission lines is [131, 132]

$$Z_0 = \begin{cases} \frac{120\pi}{\sqrt{\varepsilon} \left\{ \frac{w}{h} + 0.44127 + \frac{\varepsilon+1}{2\pi\varepsilon} \cdot \left[\ln \left(\frac{w}{h} + 0.94 \right) + 1.45158 \right] + \frac{\varepsilon-1}{0.08226\varepsilon^2} \right\}} & \text{for } w > h \\ 120 \cdot \frac{\ln \left(\frac{4h}{w} \right) + \frac{1}{8} \left(\frac{w}{h} \right)^2 - \frac{1}{2} \cdot \frac{\varepsilon-1}{\varepsilon+1} \cdot \left(0.451 + \frac{0.2415}{\varepsilon} \right)}{\sqrt{\frac{\varepsilon+1}{2}}} & \text{for } w < h \end{cases}$$

[Eq. 62]

The length l of the conductor is calculated by

$$\text{[Eq. 63]} \quad l = \underbrace{\frac{(2\pi - \alpha)}{2\pi} \pi \cdot \sum_{i=1}^N d_i}_{\text{circular parts}} + \underbrace{\sum_{i=1}^{N-1} \sqrt{d_i^2 + d_{i+1}^2 - 2d_i d_{i+1} \cos \alpha}}_{\text{connecting lines between circles}}$$

where α is the opening angle of the gap in radians and d_i the diameter of the i^{th} circle.

6.2 MATLAB TOOLBOX FOR CALCULATION OF MTLR GEOMETRIES

6.2.1 Frequency calculation

6.2.1.1 Calc_freq.m

6.2.1.1.1 Purpose

Calculates the resonance frequency using the analytic equation given in annex 6.1.

6.2.1.1.2 Usage

```
calc_freq([data | 0], [dpmax, epsilon, h, N, w, esp, [start_value]])
```

6.2.1.1.3 Input parameters

- Option 1

data... struct containing all resonator properties:

```
data.dpmax  
data.epsilon  
data.h  
data.N  
data.w  
data.esp
```

- Option 2

data=0, but all other parameters specified:

dpmax in mm ... the diameter of the center of the outermost circle of the MTLR

epsilon... substrate dielectric constant ϵ

h, w, esp in μm ... substrate thickness, conductor track width and spacing between conductor tracks, respectively

N... number of turns

start_value in MHz ... this parameter tells the algorithm to start to search for a solution closest to this starting value (this value is optional, default is 150 MHz)

6.2.1.1.4 Result

The output is the resonance frequency of the resonator with the given material and geometry parameters in Hz.

6.2.1.1.5 Examples

- Option 1

With predefined struct `data` and all its properties, this is usually used by

```
calc_freq_esp_w.m
data.N=6
data.epsilon=10.0556
data.w=250
data.esp=200
data.h=330
calc_freq(data)
```

- Option 2

For calculation of a single resonance frequency

```
calc_freq(0,14.6,10.0556,330,6,250,200,150)
```

6.2.1.2 Calc_freq_esp_w.m

6.2.1.2.1 Purpose

Calculates all resonance frequencies with a given set of `dpmax`, `epsilon`, `h` and `N`.

For `esp` and `w` all values between 1 and 500 are used, step size is given by `step`.

Results are stored in a file in the current directory.

6.2.1.2.2 Usage

```
calc_freq_esp_w(dpmax, epsilon, h, N, step)
```

options for `calc_freq_all` must be set in the source code

6.2.1.2.3 Input parameters

`dpmax` in mm ... the diameter of the center of the outermost circle of the MTLR

`epsilon`... substrate dielectric constant ϵ

`h` in μm ... substrate thickness

`N`... number of turns

step ... step size used for w and esp . E.g.: for $\text{step}=10$ the frequencies will only be calculated for multiples of $10\mu\text{m}$ for w and esp ($w=10, 20, 30, \dots$)

6.2.1.2.4 Result

All resonance frequencies calculated for a given set dpmax , epsilon , h and N with step size step for esp and w are stored in a file named $\text{res}<\text{step}>\text{um.mat}$ (e.g. res1um.mat for a step size of $\text{step}=1$)

6.2.1.2.5 Examples

```
calc_freq_esp_w(14.6, 10.0556, 330, 6, 10)
```

6.2.1.3 Calc_freq_all.m

6.2.1.3.1 Purpose

Calculates all resonance frequencies with a given set of dpmax , epsilon , h and N . This program calls the program calc_freq_esp_w.m in a loop for all requested dpmax , epsilon , h and N . The directory where the file will be saved is set in during the loop.

6.2.1.3.2 Usage

```
calc_freq_all
```

options for calc_freq_all must be set in the source code

6.2.1.3.3 Input parameters

None. Options are set in the source code directly (on top, in the commented section)

6.2.1.3.4 Result

Resulting files from calc_freq_esp_w.m are stored in a directory named

```
<home>\<dpmax>mm\eps<epsilon>\h<h>\N<N>\  
e.g.'X:\thesis\calculations\Matlab\analytic_simulation\7.3mm\eps10.0  
556\h330\N6'
```

6.2.2 Data collection

6.2.2.1 Collect_all_data.m

6.2.2.1.1 Purpose

Run through all directories created by `calc_freq_all.m`, load the `.mat` files there and store everything in a variable called `dat`.

6.2.2.1.2 Usage

`collect_all_data`

options for `collect_all_data` must be set in the source code.

6.2.2.1.3 Input parameters

None. Options are set in the source code directly (on top, in the commented section).

6.2.2.1.4 Result

after execution of this program, the values are available in a variable named `dat`

```
dat(index_dpmax, index_epsilon, index_h, N, index_esp, index_w)
```

where:

`N`... between 2 and `N_max`

`index_esp`... between 1 and `floor(500/step)`

`index_w`... between 1 and `floor(500/step)`

`index_dpmax`, `index_epsilon` and `index_h` depend on the vector/matrix size of `dpmax`, `epsilon` and `h`.

The variable `dat` is used by `search_freq.m`

6.2.3 Data analysis

6.2.3.1 Search_freq.m

6.2.3.1.1 Purpose

Search all geometries matching certain criteria such as resonance frequency, w/h, (w+esp)/h, w/esp with their respective tolerances and display the result in an ordered list.

6.2.3.1.2 Usage

search_freq

options for search_freq must be set in the source code.

6.2.3.1.3 Input parameters

In the top section of the source code the following variables can be set:

enter the frequency you are interested in (MHz):

```
freq_of_interest=68.3;
```

enter the tolerance in MHz

```
tol_freq=.1;
```

enter the ratio of w/h you want

```
w_over_h_required=.75;
```

enter its tolerance (use a high number if you don't want to use the w/h-criterion

```
tol_w_over_h=.1;
```

enter the ratio (w+esp)/h you want

```
w_plus_esp_over_h_required=1.5;
```

enter its tolerance (use a high number if you don't want to use the w/h-criterion

```
tol_w_plus_esp_over_h_required=100;
```

enter the ratio of w/esp you want

```
w_over_esp_required=1.;
```

enter its tolerance (use a high number if you don't want to use the w/esp-criterion

```
tol_w_over_esp=100;
```

enter the maximum number of turns you want to have

```
N_max=15;
```

enter the name of the base directory where all.mat is located

```
home='X:\thesis\calculations\Matlab\analytic_simulation\';
```

enter the outer coil diameters contained in dat (the matrix obtained with

```
collect_all_data.m)
```

```
d=[3.45 7.3 14.6];
```

enter the dielectric constants of the substrate materials contained in dat (the

```
matrix obtained with collect_all_data.m)
```

```
eps=[3.45 10.0556 23.6];
```

enter the substrate thicknesses contained in dat (the matrix obtained with

```
collect_all_data.m)
```

```
h=[[25 50 125];[250 330 430];[250 330 500]];
```

6.2.3.1.4 Result

A list of all resonator geometries found in dat that match the desired criteria.

The table is sorted by dpmax, epsilon, h, N, w, esp (in this order of priority).

6.2.3.1.5 Examples

The parameters used above in section 6.2.3.1.3 result in the following table:

```
searching parameter sets close to frequency of interest
found 512 parameter sets matching the frequency criterion
found 49 parameter sets matching your criteria
sorting results...
```

dpmax	epsilon	h	N	w	esp	w/h	w/esp	(w+esp)/h	f0
7.3	23.6000	250	8	180	20	0.72	9.00	0.8	68.3
7.3	23.6000	250	9	180	60	0.72	3.00	1.0	68.3
7.3	23.6000	250	9	200	50	0.80	4.00	1.0	68.4
14.6	3.4500	25	6	20	20	0.80	1.00	1.6	68.3
14.6	3.4500	25	11	20	470	0.80	0.04	19.6	68.3
14.6	3.4500	25	12	20	490	0.80	0.04	20.4	68.4
14.6	3.4500	50	7	40	120	0.80	0.33	3.2	68.3
14.6	3.4500	50	8	40	250	0.80	0.16	5.8	68.3
14.6	3.4500	50	11	40	440	0.80	0.09	9.6	68.4
14.6	3.4500	50	12	40	460	0.80	0.09	10.0	68.3
14.6	3.4500	125	8	90	160	0.72	0.56	2.0	68.4
14.6	3.4500	125	8	100	170	0.80	0.59	2.2	68.2
14.6	3.4500	125	10	90	320	0.72	0.28	3.3	68.3
14.6	3.4500	125	11	90	360	0.72	0.25	3.6	68.3
14.6	10.0556	250	6	170	230	0.68	0.74	1.6	68.3
14.6	10.0556	250	6	200	250	0.80	0.80	1.8	68.4
14.6	10.0556	250	7	170	390	0.68	0.44	2.2	68.2
14.6	10.0556	250	7	190	400	0.76	0.47	2.4	68.4
14.6	10.0556	330	6	220	160	0.67	1.38	1.2	68.4
14.6	10.0556	330	6	260	170	0.79	1.53	1.3	68.4
14.6	10.0556	330	6	270	170	0.82	1.59	1.3	68.3
14.6	10.0556	330	6	280	170	0.85	1.65	1.4	68.2
14.6	10.0556	330	8	230	410	0.70	0.56	1.9	68.3
14.6	10.0556	330	8	240	410	0.73	0.59	2.0	68.4
14.6	10.0556	330	8	280	400	0.85	0.70	2.1	68.3
14.6	10.0556	330	10	220	470	0.67	0.47	2.1	68.2

14.6	10.0556	330	10	270	450	0.82	0.60	2.2	68.4
14.6	10.0556	330	11	230	470	0.70	0.49	2.1	68.4
14.6	10.0556	330	11	250	460	0.76	0.54	2.2	68.3
14.6	10.0556	330	11	270	450	0.82	0.60	2.2	68.3
14.6	10.0556	430	6	350	70	0.81	5.00	1.0	68.2
14.6	10.0556	430	6	360	70	0.84	5.14	1.0	68.3
14.6	10.0556	430	7	300	240	0.70	1.25	1.3	68.2
14.6	10.0556	430	7	310	240	0.72	1.29	1.3	68.3
14.6	10.0556	430	7	350	230	0.81	1.52	1.3	68.3
14.6	10.0556	430	8	300	330	0.70	0.91	1.5	68.3
14.6	10.0556	430	8	350	310	0.81	1.13	1.5	68.3
14.6	10.0556	430	9	280	380	0.65	0.74	1.5	68.2
14.6	10.0556	430	10	350	360	0.81	0.97	1.7	68.3
14.6	10.0556	430	11	320	380	0.74	0.84	1.6	68.3
14.6	23.6000	250	4	190	180	0.76	1.06	1.5	68.2
14.6	23.6000	250	4	210	210	0.84	1.00	1.7	68.4
14.6	23.6000	330	4	250	90	0.76	2.78	1.0	68.2
14.6	23.6000	330	4	260	100	0.79	2.60	1.1	68.3
14.6	23.6000	330	5	240	490	0.73	0.49	2.2	68.3
14.6	23.6000	330	5	260	500	0.79	0.52	2.3	68.3
14.6	23.6000	500	5	370	330	0.74	1.12	1.4	68.4
14.6	23.6000	500	5	380	330	0.76	1.15	1.4	68.4
14.6	23.6000	500	6	400	500	0.80	0.80	1.8	68.2

6.2.3.2 F_esp_w.m

6.2.3.2.1 Purpose

Display the resonance frequency as a function of esp and w in a color-coded map. Also display the Gradient of this map, i.e. how strong is the variation of F if esp or w are slightly changed.

6.2.3.2.2 Usage

F_esp_w([freq_of_interest])

A window opens in which you can choose the file you want to display. Please choose one of the result files from calc_freq_esp_w.m (the files are called res<step>um.mat)

6.2.3.2.3 Input parameters

freq_of_interest (optional) in MHz.

The resonance frequency you are interested in.

6.2.3.2.4 Result

A contour line at the niveau of freq_of_interest will be shown in the graph. Additionally contour lines for 63.9 MHz, 123 MHz, 200 MHz and 298 MHz, corresponding to 1H-frequency at 1.5, 3, 4.7 and 7 T are displayed.

6.2.3.2.5 Examples

The jump from narrow track to wide track domain is clearly visible in the gradient map below, on the right (vertical line at $w=300\mu\text{m}$).

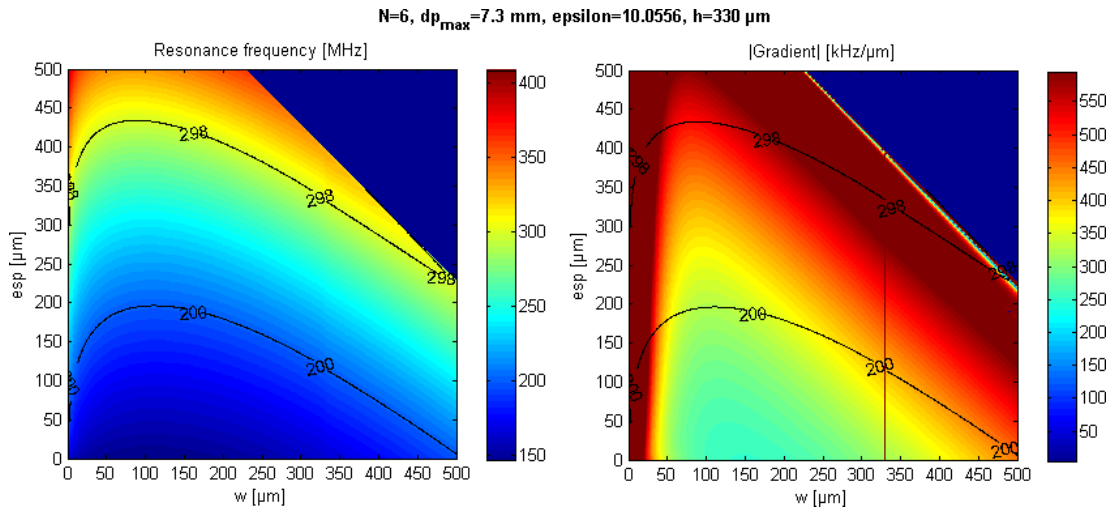


Figure 64: Example of frequency calculations

The example shows the results for an MTLR coil with 6 turns and an outer diameter of 7.3 mm built on a 330 μm thick sapphire substrate.

Left: The resonance frequency in dependence of conductor width w and spacing esp .

Right: The gradient of the frequency ΔF for the same range of w and esp . Lower ΔF values (color coded as indicated in the bars to the right) suggest a lower sensitivity to small production inaccuracies.

7 BIBLIOGRAPHY

- [1] BLOCH, F., HANSEN, W.W., and PACKARD, M.R., Nuclear Induction. *Physical Review*, **70**:460, 1946
- [2] CARSON, J.R., A generalization of the reciprocity theorem. *Bell System Technical Journal*, **3**:393–399, 1924
- [3] SOMMERFELD, A., Das Reziprozitäts-Theorem in der drahtlosen Telegraphie. *Jahrbuch der drahtlosen Telegraphie und Telephonie*, **26**:93, 1925
- [4] SVESHNIKOVA, M.P., The reciprocity theorem in electrodynamics and radiotelegraphy. *Journal of the Russian Physico-Chemical Association*, p. 453, 1927
- [5] CARSON, J.R., Reciprocal theorems in radio communication. *Proceedings of the IRE*, **17**:952–957, 1929
- [6] BALLANTINE, S., Reciprocity in electromagnetic, mechanical, acoustical, and interconnected systems. *Proceedings of the IRE*, **17**:929–952, 1929
- [7] MONTGOMERY, C.G., DICKE, R.H., and PURCELL, E.M., *Principles of Microwave Circuits*. McGraw-Hill, New York, 1948

- [8] HOULT, D.I. and RICHARDS, R.E., The signal-to-noise ratio of the nuclear magnetic resonance experiment. *Journal of Magnetic Resonance*, **24**:71–85, 1976
- [9] VESSELLE, H. and COLLIN, R.E., The signal-to-noise ratio of nuclear magnetic resonance surface coils and application to a lossy dielectric cylinder model. I. Theory. *IEEE Transactions on Biomedical Engineering*, **42**(5):497–506, 1995
- [10] HOULT, D.I. and GINSBERG, N.S., The quantum origins of the free induction decay signal and spin noise. *Journal of Magnetic Resonance*, **148**:182–199, 2001
- [11] INSKO, E.K., ELLIOTT, M.A., SCHOTLAND, J.C., and LEIGH, J.S., Generalized reciprocity. *Journal of Magnetic Resonance*, **131**(1):111–117, 1998
- [12] VAN DER KLINK, J.J., The NMR reciprocity theorem for arbitrary probe geometry. *Journal of Magnetic Resonance*, **148**(1):147–154, 2001
- [13] IBRAHIM, T.S., Analytical approach to the MR signal. *Magnetic resonance in medicine*, **54**(3):677–682, 2005
- [14] KREIS, R., SLOTBOOM, J., PIETZ, J., JUNG, B., and BOESCH, C., Quantitation of localized ³¹P magnetic resonance spectra based on the reciprocity principle. *Journal of Magnetic Resonance*, **149**(2):245–250, 2001
- [15] MISPELTER, J., LUPU, M., and BRIGUET, A., *NMR probeheads for biophysical and biomedical experiments: theoretical principles & practical guidelines*. Imperial College Press, London, 2006
- [16] PIMMEL, P., *Les Antennes en Résonance Magnétique Nucleaire : Fonctionnement et Réalisation - Résonateurs pour l'imagerie et pour la spectroscopie in vivo*. Phd thesis, Lyon, 1990

- [17] HAACKE, E.M., BROWN, R., THOMPSON, M., and VENKATESAN, R., *Magnetic Resonance Imaging: Physical Principles and Sequence Design*. Wiley-Liss, 1st ed., 1999
- [18] ABRAGAM, A., *The Principles of Nuclear Magnetism*. *International Series of Monographs on Physics*, **32**, 1961
- [19] HELSTROM, C.W., *Probability and Stochastic processes for Engineers*. Maxwell, Macmillan, 2nd ed., 1991
- [20] NYQUIST, H., Thermal Agitation of Electric Charge in Conductors. *Physical Review*, **32**(1):110–113, 1928
- [21] HOULT, D.I. and LAUTERBUR, P.C., The sensitivity of the zeugmatographic experiment involving human samples. *Journal of Magnetic Resonance*, **34**:425–433, 1979
- [22] DECORPS, M., BLONDET, P., REUTENAUER, H., ALBRAND, J.P., and REMY, C., An inductively coupled, series-tuned NMR probe. *Journal of Magnetic Resonance*, **65**:100–109, 1985
- [23] GUÉRON, M. and LEROY, J.L., NMR of water protons. The detection of their nuclear-spin noise, and a simple determination of absolute probe sensitivity based on radiation damping. *Journal of Magnetic Resonance*, **85**:209–215, 1989
- [24] TERMAN, F.E., *Radioengineer's Handbook*. McGraw-Hill, 1943
- [25] BEDNORZ, J.G. and MUELLER, K.A., Possible High T_c Superconductivity in the Ba-La-Cu-O System. *Zeitschrift für Physik B: Condensed Matter*, **64**:189–193, 1986
- [26] DUZER, T.V. and TURNER, C.W., *Principle of Superconducting Devices and Circuits*. Elsevier, 1981

- [27] SHEN, Z.Y., *High-temperature Superconducting Microwave Circuits*. Artech House, 1994
- [28] POIRIER-QUINOT, M., *Microscopie locale par résonance magnétique chez l'homme et le petit animal à l'aide d'antennes miniatures en cuivre ou en céramique supraconductrice*. Phd thesis, Université Paris-Sud XI, 2004
- [29] BARRAL, J.K., *In vivo high-resolution magnetic resonance imaging*. Phd thesis, Stanford University, 2010
- [30] VESTER, M., STEINMEYER, F., ROAS, B., THUMMES, G., and KLUNDT, K., High temperature superconducting surface coils with liquid nitrogen or pulse tube refrigeration. *In: Proceedings of the ISMRM*, p. 1528, Vancouver, Canada, 1997
- [31] ODOJ, F., ROMMEL, E., VON KIENLIN, M., and HAASE, A., A superconducting probehead applicable for nuclear magnetic resonance microscopy at 7 T. *Review of Scientific Instruments*, **69**:2708–2712, 1998
- [32] GINEFRI, J.C., DARRASSE, L., and CROZAT, P., Comparison of radio-frequency and microwave superconducting properties of YBaCuO dedicated to magnetic resonance imaging. *IEEE Transactions on Applied Superconductivity*, **9**:4695–4701, 1999
- [33] GINEFRI, J.C., CROZAT, P., and DARRASSE, L., Influence of static magnetic field on a YBCO surface coil dedicated to nuclear magnetic resonance imaging. vol. 3, pp. 449–456, 2002
- [34] DARRASSE, L. and GINEFRI, J.C., Perspectives with cryogenic RF probes in biomedical MRI. *Biochimie*, **85**(9):915–937, 2003
- [35] WALD, L.L., FISCHL, B., and ROSEN, B.R., *High-Resolution and Microscopic Imaging at High Field in: Ultra High Field Magnetic Resonance Imaging*, vol. 26, chap. 11, pp. 343–371. Springer, Berlin, 2006

- [36] BRASCH, R.C., WEINMANN, H.J., and WESBEY, G.E., Contrast-enhanced NMR imaging - animal studies using gadolinium-DTPA complex. *American Journal of Roentgenology*, **142**:625–630, 1984
- [37] EDELSTEIN, W.A., FOSTER, T.H., and SCHENCK, J.F., The relative sensitivity of surface coils to deep lying tissues. *In: Proceedings of the SMRM*, p. 964, London, U.K., 1985
- [38] SERFATY, S., DARRASSE, L., and KAN, S., The pinpoint NMR coil. *In: Proceedings of the SMR*, San Francisco, U.S.A., 1994
- [39] ROEMER, P.B., EDELSTEIN, W.A., HAYES, C.E., SOUZA, S.P., and MUELLER, O.M., The NMR phased array. *Magnetic Resonance in Medicine*, **16**(2):192–225, 1990
- [40] DOTY, F.D., ENTZMINGER, G., KULKARNI, J., PAMARTHY, K., and STAAB, J.P., Radio frequency coil technology for small-animal MRI. *NMR in Biomedicine*, **20**:304–325, 2007
- [41] VAUGHAN, J.T., *Ultra High Field MRI: High-Frequency Coils in: Ultra High Field Magnetic Resonance Imaging*, vol. 26, chap. 6, pp. 127–161. Springer, Berlin, 2006
- [42] WITHERS, R.S., LIANG, G.C., COLE, B.F., and JOHANSSON, M., Thin film HTC probe coil for magnetic resonance imaging. *IEEE Transactions on Applied Superconductivity*, **3**(1):2450–2453, 1993
- [43] SAINT-JALMES, H., COEUR-JOLY, O., GUILLOUX-VIRY, M., PERRIN, A., THIVET, C., PADIOU, J., DOUSSELIN, G., and PELLAN, Y., Low field nuclear magnetic resonance imaging using HTS YBCO thin film receiver coil operating at 77 K. *Journal of Magnetic Resonance Analysis*, **2**:53–56, 1996
- [44] MILLER, J.R., ZHANG, K., MA, Q.Y., MUN, I.K., JUNG, K.J., KATZ, J., ACE, D.W., and KOUNTZ, D.J., Superconducting receiver coils for sodium magnetic

- resonance imaging. *IEEE Transactions on Biomedical Engineering*, **43**:1197–1199, 1996
- [45] MANN, L.D., DUERK, J.L., WENDT, M., HANSEN, K.L., and BREY, W.W., A Small Superconductive Surface Coil with Enhanced Bandwidth and Active Decoupling. *In: Proceedings of the ISMRM*, p. 435, Sydney, Australia, 1998
- [46] GINEFRI, J.C., DARRASSE, L., CROZAT, P., and SERFATY, S., High-temperature superconducting receiver coil for NMR skin imaging. *Journal de Physique IV*, **8**, 1998
- [47] HURLSTON, S.E., BREY, W.W., SUDDARTH, S.A., JOHNSON, G.A., and FITZSIMONS, E.G., A high-temperature superconducting Helmholtz probe for microscopy at 9.4 T. *Magnetic Resonance in Medicine*, **41**:1032–1038, 1999
- [48] HILL, H.D.W., Improved sensitivity of NMR spectroscopy probes by use of high-temperature superconductive detection coils. *IEEE Transactions on Applied Superconductivity*, **7**:3750–3755, 1997
- [49] BLACK, R.D., EARLY, T.A., ROEMER, P.B., MUELLER, K.A., CAMPERO, M.A., TURNER, L.G., and JOHNSON, G.A., A high-temperature superconducting receiver for nuclear magnetic resonance microscopy. *Science*, **259**:793–795, 1993
- [50] MCFARLAND, E.W. and MORTARA, A., Three-dimensional NMR microscopy: improving SNR with temperature and microcoils. *Magnetic Resonance Imaging*, **10**:279–288, 1992
- [51] HOHMANN, R., LIENERT, C., ZHANG, Y., BOUSACK, H., THUMMES, G., and HEIDEN, C., Cooling performance of a Joule Thomson cooler and Pulse tube cooler using a HT SQUID. *IEEE Transactions on Applied Superconductivity*, **9**:3688–3691, 1999

- [52] WRIGHT, A.C., SONG, H.K., ELLIOTT, D.M., and WEHRLI, F.W., Use of a Joule-Thomson micro-refrigerator to cool a radio-frequency coil for magnetic resonance microscopy. *Review of Scientific Instruments*, **76**(1):14301–14307, 2005
- [53] MILLER, J.R., HURLSTON, S.E., MA, Q.Y., FACE, D.W., KOUNTZ, D.J., MACFALL, J.R., HEDLUND, L.W., and JOHNSON, G.A., Performance of a high-temperature superconducting probe for in-vivo microscopy at 2.0 T. *Magnetic Resonance in Medicine*, **41**(1):72–79, 1999
- [54] SERFATY, S., HAZIZA, N., DARRASSE, L., and KAN, S., Multi-Turn Split-Conductor Transmission-Line Resonators. *Magnetic Resonance in Medicine*, **38**:687–689, 1997
- [55] GONORD, P., KAN, S., and LEROY-WILLIG, A., Parallel-plate split-conductor surface coil: Analysis and design. *Magnetic Resonance in Medicine*, **6**(3):353–358, 1988
- [56] EBLING, F.J.G., EADY, R.A.J., and LEIGH, I.M., *Textbook of Dermatology*. Blackwell Scientific, 5th ed., 1992
- [57] CIOBANU, L., 3D micron-scale MRI of single biological cells. *Solid State Nuclear Magnetic Resonance*, **25**(1-3):138–141, 2004
- [58] TYSZKA, J., FRASER, S., and JACOBS, R., Magnetic resonance microscopy: recent advances and applications. *Current Opinion in Biotechnology*, **16**(1):93–99, 2005
- [59] WEIGER, M., SCHMIDIG, D., DENOTH, S., MASSIN, C., VINCENT, F., SCHENKEL, M., and FEY, M., NMR microscopy with isotropic resolution of 3.0 μm using dedicated hardware and optimized methods. *Concepts in Magnetic Resonance Part B: Magnetic Resonance Engineering*, **33B**(2):84–93, 2008

- [60] FLINT, J.J., LEE, C.H., HANSEN, B., FEY, M., SCHMIDIG, D., BUI, J.D., KING, M.A., POULSEN, P.V., and BLACKBAND, S.J., Magnetic resonance microscopy of mammalian neurons. *NeuroImage*, **46**(4):1037–1040, 2009
- [61] LEE, S.C., KIM, K., KIM, J., YI, J.H., LEE, S., and CHEONG, C., MR microscopy of micron scale structures. *Magnetic Resonance Imaging*, **27**(6):828–833, 2009
- [62] GINEFRI, J.C., DARRASSE, L., and CROZAT, P., High-Temperature Superconducting Surface Coil for In Vivo Microimaging of the Human Skin. *Magnetic Resonance in Medicine*, **45**:376–382, 2001
- [63] POIRIER-QUINOT, M., GINEFRI, J.C., GIRARD, O., ROBERT, P., and DARRASSE, L., Performance of a miniature high-temperature superconducting (HTS) surface coil for in vivo microimaging of the mouse in a standard 1.5T clinical whole-body scanner. *Magnetic Resonance in Medicine*, **60**(4):917–927, 2008
- [64] LAISTLER, E., POIRIER-QUINOT, M., GINEFRI, J.C., LAMBERT, S., DUBUISSON, R.M., BORIASSE, E., MOSER, E., and DARRASSE, L., Sub-nanoliter microscopic MR imaging of the human skin in vivo using a 12 mm superconducting surface coil at 1.5 Tesla. *In: Proceedings of the ISMRM*, p. 822, Honolulu, U.S.A., 2009
- [65] BITTOUN, J., SAINT-JALMES, H., QUERLEUX, B.G., DARRASSE, L., JOLIVET, O., PERETTI, I.I., WARTSKI, M., RICHARD, S.B., and LEVEQUE, J.L., In vivo high-resolution MR imaging of the skin in a whole-body system at 1.5 T. *Radiology*, **176**(2):457–460, 1990
- [66] BITTOUN, J., QUERLEUX, B.G., JOLIVET, O., and RICHARD, S.B., Microscopic imaging of the skin in-vivo by using a high gradient intensity and a narrow bandwidth, 1995

- [67] SONG, H.K., WEHRLI, F.W., and MA, J., In vivo MR microscopy of the human skin. *Magnetic Resonance in Medicine*, **37**(2):185–91, 1997
- [68] BARRAL, J.K., BANGERTER, N.K., HU, B.S., and NISHIMURA, D.G., In vivo high-resolution magnetic resonance skin imaging at 1.5 T and 3 T. *Magnetic Resonance in Medicine*, **63**(3):790–796, 2010
- [69] RICHARD, S.B., QUERLEUX, B.G., BITTOUN, J., and IDY-PERETTI, I., In vivo proton relaxation times analysis of the skin layers by magnetic resonance imaging. *Journal of Investigative Dermatology*, **97**(1):120–125, 1991
- [70] QUERLEUX, B.G., RICHARD, S.B., BITTOUN, J., JOLIVET, O., PERETTI, I.I., BAZIN, R., and LEVEQUE, J.L., In vivo hydration profile in skin layers by high-resolution magnetic resonance imaging. *Skin Pharmacology*, **7**(4):210–216, 1994
- [71] RICHARD, S.B., QUERLEUX, B.G., BITTOUN, J., JOLIVET, O., PERETTI, I.I., LACHARRIERE, O.D., and LEVEQUE, J.L., Characterization of the Skin In Vivo by High Resolution Magnetic Resonance Imaging: Water Behavior and Age-Related Effects. *Journal of Investigative Dermatology*, **100**(5):705–709, 1993
- [72] WRIGHT, A.C., BOHNING, D.E., PECHENY, A.P., and SPICER, K.M., Magnetic resonance chemical shift microimaging of aging human skin in vivo: initial findings. *Skin Research and Technology*, **4**:55–62, 1998
- [73] MAURER, J., KNOLLMANN, F.D., SCHLUMS, D., GARBE, C., VOGL, T.J., BIER, J., and FELIX, R., Role of high-resolution magnetic resonance imaging for differentiating melanin-containing skin tumors. *Investigative Radiology*, **30**(11):638–43, 1995
- [74] WEIS, J.R., ERICSSON, A., ASTROM, G., SZOMOLANYI, P., and HEMMINGSSON, A., High-resolution spectroscopic imaging of the human skin. *Magnetic Resonance Imaging*, **19**(2):275–8, 2001

- [75] The skin's blood vessel system,
http://www.scf-online.com/english/40_e/bloodvessel40_e.htm
- [76] ACKERMAN, A.B., CHONCHITNANT, N., SANCHEZ, J., and GUO, Y., *Histologic Diagnosis of Inflammatory Skin Disease: An Algorithmic Method Based on Pattern Analysis*. Williams & Wilkins, Baltimore, 2nd ed., 1997
- [77] LIFFERS, A., VOGT, M., and ERMERT, H., In vivo biomicroscopy of the skin with high-resolution magnetic resonance imaging and high frequency ultrasound. *Biomedizinische Technik, Berlin*, **48**(5):130–134, 2003
- [78] KLARHÖFER, M., CSAPÓ, B., BALÁSSY, C., SZÉLES, J.C., and MOSER, E., High-resolution blood flow velocity measurements in the human finger. *Magnetic Resonance in Medicine*, **45**(4):716–719, 2001
- [79] SZÉLES, J.C., CSAPÓ, B., KLARHÖFER, M., BALÁSSY, C., HODA, R., BERG, A., RODEN, M., POLTERAUER, P., WALDHÄUSL, W., and MOSER, E., In vivo magnetic resonance micro-imaging of the human toe at 3 Tesla. *Magnetic Resonance Imaging*, **19**(9):1235–1238, 2001
- [80] MENZIES, S.M., CROTTY, K., INGVAR, C., and MCCARTHY, W., *Dermoscopy. An Atlas*. McGraw-Hill, New York, 3 ed., 2009
- [81] DILL-MÜLLER, D. and MASCHKE, J., Ultrasonography in dermatology. *Journal of the German Society of Dermatology*, **5**(8):689–707, 2007
- [82] ASPRES, N., EGERTON, I.B., LIM, A.C., and SHUMACK, S.P., Imaging the skin. *Australasian Journal of Dermatology*, **44**:19–27, 2003
- [83] EL GAMMAL, S., EL GAMMAL, C., KASPAR, K., PIECK, C., ALTMAYER, P., VOGT, M., and ERMERT, H., Sonography of the skin at 100 MHz enables in vivo visualization of stratum corneum and viable epidermis in palmar skin and psoriatic plaques. *Journal of Investigative Dermatology*, **113**(5):821–819, 1999

- [84] DREXLER, W. and FUJIMOTO, J.G., eds., *Optical Coherence Tomography: Technology and Applications*. Springer, Berlin, 2008
- [85] MOGENSEN, M., THRANE, L., JØRGENSEN, T.M., ANDERSEN, P.E., and JEMEC, G.B.E., OCT imaging of skin cancer and other dermatological diseases. *Journal of Biophotonics*, **2**(6-7):442–451, 2009
- [86] MOGENSEN, M., NÜRNBERG, B.M., FORMAN, J.L., THOMSEN, J.B., THRANE, L., and JEMEC, G.B.E., In vivo thickness measurement of basal cell carcinoma and actinic keratosis with optical coherence tomography and 20-MHz ultrasound. *British Journal of Dermatology*, **160**(5):1026–33, 2009
- [87] SALVINI, C., MASSI, D., CAPPETTI, A., STANTE, M., CAPPUGI, P., and FABBRI, P.C., Application of optical coherence tomography in non-invasive characterization of skin vascular lesions. *Skin Research and Technology*, **14**(1):89–92, 2008
- [88] BRANZAN, A.L., LANDTHALER, M., and SZEIMIES, R.M., In vivo confocal scanning laser microscopy in dermatology. *Lasers in Medical Science*, **22**:73–82, 2007
- [89] MASTERS, B.R., GONNORD, G., and CORCUFF, P., Three-dimensional microscopic biopsy of in vivo human skin: a new technique based on a flexible confocal microscope. *Journal of Microscopy*, **185**(3):329–338, 1997
- [90] CSERNOK, E. and GROSS, W.L., Primary vasculitides and vasculitis confined to skin: clinical features and new pathogenic aspects. *Archives of Dermatological Research*, **292**:427–436, 2000
- [91] STEIN, S.L., MILLER, L.C., and KONNIKOV, N., Wegener's granulomatosis: case report and literature review. *Pediatric Dermatology*, **15**:352–356, 1998

- [92] ZELGER, B., SEPP, N., and STOCKHAMMER, G., Sneddon's syndrome. A long-term follow-up of 21 patients. *Archives of Dermatology*, **129**:437–447, 1993
- [93] WOHLRAB, J., FISCHER, M., WOLTER, M., and MARSCH, W.C., Diagnostic impact and sensitivity of skin biopsies in Sneddon's syndrome. A report of 15 cases. *British Journal of Dermatology*, **145**:285–288, 2001
- [94] GINEFRI, J.C., DURAND, E., and DARRASSE, L., Quick measurement of nuclear magnetic resonance coil sensitivity with a single-loop probe. *Review of Scientific Instruments*, **70**(12):4730–4731, 1999
- [95] GIRARD, O., GINEFRI, J.C., and DARRASSE, L., Method to extract the non-linear characteristics of high temperature superconducting (HTS) RF coils. *In: Proceedings of the ISMRM, Seattle, U.S.A., 2006*
- [96] GIRARD, O., GINEFRI, J.C., POIRIER-QUINOT, M., and DARRASSE, L., Method for nonlinear characterization of radio frequency coils made of high temperature superconducting material in view of magnetic resonance imaging applications. *Review of Scientific Instruments*, **78**(12), 2007
- [97] RAAD, A. and DARRASSE, L., Optimization of NMR receiver bandwidth by inductive coupling. *Magnetic Resonance Imaging*, **10**(1):55–65, 1992
- [98] LAISTLER, E., GIRARD, O., GINEFRI, J.C., DUBUISSON, R.M., BITTOUN, J., MOSER, E., and DARRASSE, L., Advances in human skin in-vivo MRI with a miniature HTS surface coil and a new-generation 1.5 T body scanner. *In: Proceedings of the ISMRM, Berlin, Germany, 2007*
- [99] POIRIER-QUINOT, M., GIRARD, O., LAISTLER, E., DUBUISSON, R.M., GINEFRI, J.C., and DARRASSE, L., Ultimate spatial resolution accessible with a miniature HTS coil and a new-generation 1.5 T body scanner. *In: Proceedings of the ISMRM, Berlin, Germany, 2007*

- [100] BERG, A., WANZENBOECK, H., HESJEDAL, T., and MOSER, E., MR-microscopy at 35 μm on a whole body MR-system: quality control by modulation transfer function and applications. *Proceedings of the ISMRM*, 9:925, 2001
- [101] BERG, A., Testphantom zur Kontrolle der Abbildungsqualität in der hochauflösenden NMR-Bildgebung, Patent DE19904635A1, Deutsches Patent- und Markenamt, 1999
- [102] EVANS, A.L., *The evaluation of medical images*. Medical physics handbooks, Adam Hilger Ltd., in collaboration with the Hospital Physicists Association, 1981
- [103] EWEN, K., *Moderne Bildgebung*. Thieme, Stuttgart, 2003
- [104] SPM - Statistical Parametric Mapping
- [105] RORDEN, C. and BRETT, M., Stereotaxic display of brain lesions. *Behavioural Neurology*, 12(4):191–200, 2000
- [106] LAISTLER, E., LOEWE, R., and MOSER, E., Magnetic Resonance Microimaging of Human Skin Vasculature in vivo at 3 Tesla. *Magnetic Resonance in Medicine*, 2010 (in press)
- [107] LAISTLER, E. and MOSER, E., MR microscopy of human skin vasculature in vivo at 3 Tesla using a small copper surface coil. *In: Proceedings of the ISMRM*, p. 828, Honolulu, U.S.A., 2009
- [108] LAISTLER, E. and MOSER, E., Quantitative description of vessel geometry from microscopic MR skin imaging. *In: Proceedings of the ISMRM*, Montreal, Canada, 2011 (submitted)

- [109] KROON, D.J., Viewer3D package for MATLAB,
<http://www.mathworks.com/matlabcentral/fileexchange/21993-viewer3d>
- [110] VÄLISUO, P., KAARTINEN, I., KUOKKANEN, H., and ALANDER, J., The colour of blood in skin: a comparison of Allen's test and photonics simulations. *Skin Research and Technology*, **16**(4):390–396, 2010
- [111] REUSS, J.L., Multilayer modeling of reflectance pulse oximetry. *IEEE Transactions on Biomedical Engineering*, **52**(2):153–159, 2005
- [112] WOYTASIK, M., GINEFRI, J.C., RAYNAUD, J.S., POIRIER-QUINOT, M., DUFOUR-GERGAM, E., GRANDCHAMP, J.P., GIRARD, O., ROBERT, P., GILLES, J.P., MARTINCIC, E., and DARRASSE, L., Characterization of flexible RF microcoils dedicated to local MRI. *Microsystem Technologies*, **13**(11-12):1575–1580, 2007
- [113] WOYTASIK, M., MOULIN, J., MARTINCIC, E., COUTROT, A.L., and DUFOUR-GERGAM, E., Copper planar microcoils applied to magnetic actuation. *Microsystem Technologies*, **14**(7):951–956, 2008
- [114] LAISTLER, E., GINEFRI, J.C., POIRIER-QUINOT, M., DUBUISSON, R.M., RUBIN, A., WOYTASIK, M., DUFOUR-GERGAM, E., DARRASSE, L., and MOSER, E., MR microscopy of the human skin in vivo at 7 Tesla using an inductively coupled 6 mm multi-turn transmission line resonator. *In: Proceedings of the ESMRMB*, Antalya, Turkey, 2009
- [115] FRISTON, K.J., FRITH, C.D., FRACKOWIAK, R.S.J., and TURNER, R., Characterizing dynamic brain responses with fMRI: a multivariate approach. *Neuroimage*, **2**:166–172, 1995
- [116] SCHÖBINGER, M., *Analyse von Gefäßstrukturen und versorgtem Gewebe*. Technical report 131/2002, Deutsches Krebsforschungszentrum Heidelberg, Heidelberg, Germany, 2002

- [117] DIESTEL, R., *Graph Theory*. Springer, 3rd ed., 2005
- [118] MA, C.M. and SONKA, M., A fully parallel 3D thinning algorithm and its applications. *Computer Vision and Image Understanding*, **64**(3):420–433, 1996
- [119] TSAO, Y. and FU, K., A parallel thinning algorithm for 3-D pictures. *Computer Graphics and Image Processing*, **17**(4):315–331, 1981
- [120] WANG, T. and BASU, A., A note on 'A fully parallel 3D thinning algorithm and its applications'. *Pattern Recognition Letters*, **28**(4):501–506, 2007
- [121] GERIG, G., KOLLER, T., SZÉKELY, G., BRECHBÜHLER, C., and KÜBLER, O., Symbolic description of 3-D structures applied to cerebral vessel tree obtained from MR angiography volume data. *Lecture Notes in Computer Science*, **687**(Information Processing in Medical Imaging):94–111, 1993
- [122] LEE, T.C., KASHYAP, R.L., and CHU, C.N., Building Skeleton Models via 3-D Medial Surface Axis Thinning Algorithms. *Graphical Models and Image Processing*, **56**(6):462–478, 1994
- [123] SOLER, L., *Une nouvelle méthode de segmentation des structures anatomiques et pathologiques: application aux angioscanners 3D du foie pour la planification chirurgicale*. Phd thesis, Université de Paris 11, Orsay, 1998
- [124] SELLE, D., *Analyse von Gefäßstrukturen in medizinischen Schichtdatensätzen für die computergestützte Operationsplanung*. Phd thesis, Universität Bremen, 2000
- [125] ITK - Insight Toolkit, www.itk.org
- [126] VTK - Visualization Toolkit, www.vtk.org

- [127] HARDY, C.J., GIAQUINTO, R.O., PIEL, J.E., ROHLING, K.W., MARINELLI, L., BLEZEK, D.J., FIVELAND, E.W., DARROW, R.D., and FOO, T.K.F., 128-channel body MRI with a flexible high-density receiver-coil array. *Journal of Magnetic Resonance Imaging*, **28**(5):1219–1225, 2008
- [128] REICHENBACH, J.R., BARTH, M., HAACKE, E.M., KLARHÖFER, M., KAISER, W.A., and MOSER, E., High-resolution MR Venography at 3.0Tesla. *Journal of Computer Assisted Tomography*, **24**(6):949–957, 2000
- [129] DEISTUNG, A., DITTRICH, E., SEDLACIK, J., RAUSCHER, A., and REICHENBACH, J.R., ToF-SWI: simultaneous time of flight and fully flow compensated susceptibility weighted imaging. *Journal of Magnetic Resonance Imaging*, **29**(6):1478–1484, 2009
- [130] GONORD, P., KAN, S., LEROY-WILLIG, A., and WARY, C., Multigap parallel-plate bracelet resonator frequency determination and applications. *Review of Scientific Instruments*, **65**(11):3363–3366, 1994
- [131] WHEELER, H.A., Transmission-line properties of parallel wide strips by a conformal-mapping approximation. *IEEE Transactions on Microwave Theory*, **12**:280–289, 1964
- [132] WHEELER, H.A., Transmission-line properties of a strip on a dielectric sheet on a plane. *IEEE Transactions on Microwave Theory*, **25**:631–647, 1977

8 LIST OF FIGURES

Figure 1: Spin excess in direction of \vec{B}_0	7
Figure 2: Relaxation mechanisms	9
Figure 3: Noise regimes	18
Figure 4: Alternative representation of noise regimes	19
Figure 5: Influence of coil size on sensitivity	25
Figure 6: Optimization of size and position for a lossless circular coil	26
Figure 7: Coil with localized elements (spiral)	34
Figure 8: Coil with localized elements (interdigitated capacities)	35
Figure 9: Split-Conductor Transmission-Line (STR)	35
Figure 10: Multi-turn Split-Conductor Transmission-Line Resonator (MTLR)	36
Figure 11: Schematic of skin vasculature	41
Figure 12: Organization of skin layers.....	41
Figure 13: Clinical appearance of cutaneous vasculitis	49
Figure 14: Philips Achieva 1.5 T Scanner	53
Figure 15: Parameters in the semi-empirical analytical calculation.....	55
Figure 16: Measurement setup using a directional coupler	56
Figure 17: Typical curves for compensated T/R over frequency	59
Figure 18: HTS coil mounting in the cryostat	61
Figure 19: The cryostat for the HTS coil	61
Figure 20: Experimental setup with superconducting surface coil at 1.5 T	63
Figure 21: Positioning of the coil and read/phase directions	65
Figure 22: Skin image with HTS coil, 20 x 60 μm in-plane resolution.....	69

Figure 23: Skin images with HTS coil, 100 μm isotropic resolution	71
Figure 24: MIPs before and after chemical shift filtering	72
Figure 25: Skin images with HTS coil, 80 μm isotropic resolution	73
Figure 26: Segmented vessel trees from HTS coil data.....	74
Figure 27: SNR profile for 80 μm isotropic resolution skin images	75
Figure 28: Noise contribution of the tuning copper ring	76
Figure 29: SNR degradation due to the tuning copper ring	77
Figure 30: 3 Tesla Bruker MedSpec S300 whole-body scanner	80
Figure 31: The 15 mm surface coil	80
Figure 32: Resolution phantom (photograph).....	82
Figure 33: MR image of the resolution phantom	86
Figure 34: Modulation of the MR signal on the resolution phantom	86
Figure 35: The modulation transfer function.....	87
Figure 36: Human thigh skin in vivo with isotropic resolution of 100 μm	89
Figure 37: Images of the finger and the skin of the back	90
Figure 38: MIPs before and after chemical shift filtering	91
Figure 39: 3D reconstruction of a segmented vessel tree	92
Figure 40: Examples of other segmented vessel trees	93
Figure 41: Siemens Magnetom 7 T.....	97
Figure 42: Photograph of the 6 mm coil for 7 T	98
Figure 43: Experimental setup for 7 T skin imaging	100
Figure 44: 7T tomato images with 6 mm coil, 100 μm isotropic resolution ..	102
Figure 45: 7T skin image with 6 mm coil, 100 μm isotropic resolution	102
Figure 46: Typical result of image realignment	105
Figure 47: Model of a vessel affected by the chemical shift artifact.....	106
Figure 48: The chemical shift filter kernel	107
Figure 49: Processing steps of the chemical shift filtering technique	108
Figure 50: Different ratios of vessel diameter vs. chemical shift in vivo	109
Figure 51: Chemical shift filter procedure applied on in vivo data	109
Figure 52: Simulated vessel data for evaluation of chemical shift filter	110

Figure 53: Impact of chemical shift filter on vessel SNR 111

Figure 54: Impact of chemical shift filter on vessel CNR..... 111

Figure 55: Demonstration of the distance transform 112

Figure 56: Representation of a vessel tree as a graph 113

Figure 57: Example of an adjacency matrix and its corresponding graph 114

Figure 58: The 26-neighborhood of a point p 116

Figure 59: Example subset of the 66 deleting templates 117

Figure 60: Screenshot of the MATLAB program performing skeletonization 118

Figure 61: Example of a junction where standard node classification fails.... 120

Figure 62: Existing schemes to represent a skeleton as a graph 121

Figure 63: Steps from the skeleton to the reduced graph..... 123

Figure 64: Example of frequency calculations XI

9 LIST OF TABLES

Table 1: Scaling rules for Q, coil sensitivity and SNR	23
Table 2: Sequence parameters for the 1.5 T experiments	66
Table 3: Quality factor of the HTS coil under different conditions	68
Table 4: SNR values for different skin structures in the 1.5 T measurements .	75
Table 5: Sequence parameters for the 3 T measurements	83
Table 6: Skin layer thickness for different anatomical regions.....	88
Table 7: Quantitative vascular parameters from 3 T MR microimaging.....	94
Table 8: SNR in different dermal structures.....	95
Table 9: Sequence parameters for the 7 T measurements	100

10 PUBLICATIONS AND PRESENTATIONS

The following list contains the author's publication on study II (chapter 3.2) and scientific conference abstracts for the annual meetings of the International Society for Magnetic Resonance in Medicine (ISMRM) and the European Society for Magnetic Resonance in Medicine and Biology (ESMRMB) based on the findings of this thesis. A second publication in collaboration with Luc Darrasse's group in Orsay on study I (chapter 3.1) is currently in preparation.

LAISTLER, E., LOEWE, R., and MOSER, E., Magnetic Resonance Microimaging of Human Skin Vasculature in vivo at 3 Tesla. *Magnetic Resonance in Medicine*, 2010 (in press)

LAISTLER, E., GIRARD, O., GINEFRI, J.C., DUBUISSON, R.M., BITTOUN, J., MOSER, E., and DARRASSE, L., Advances in human skin in-vivo MRI with a miniature HTS surface coil and a new-generation 1.5 T body scanner. *In: Proceedings of the ISMRM*, Berlin, Germany, 2007 (oral presentation)

POIRIER-QUINOT, M., GIRARD, O., LAISTLER, E., DUBUISSON, R.M., GINEFRI, J.C., and DARRASSE, L., Ultimate spatial resolution accessible with a miniature HTS coil and a new-generation 1.5 T body scanner. *In: Proceedings of the ISMRM*, Berlin, Germany, 2007 (poster)

LAISTLER, E. and **MOSER, E.**, MR microscopy of human skin vasculature in vivo at 3 Tesla using a small copper surface coil. *In: Proceedings of the ISMRM*, p. 828, Honolulu, U.S.A., 2009 (oral presentation)

LAISTLER, E., **POIRIER-QUINOT, M.**, **GINEFRI, J.C.**, **LAMBERT, S.**, **DUBUISSON, R.M.**, **BORIASSE, E.**, **MOSER, E.**, and **DARRASSE, L.**, Sub-nanoliter microscopic MR imaging of the human skin in vivo using a 12 mm superconducting surface coil at 1.5 Tesla. *In: Proceedings of the ISMRM*, p. 822, Honolulu, U.S.A., 2009 (oral presentation)

LAISTLER, E., **GINEFRI, J.C.**, **POIRIER-QUINOT, M.**, **DUBUISSON, R.M.**, **RUBIN, A.**, **WOYTASIK, M.**, **DUFOUR-GERGAM, E.**, **DARRASSE, L.**, and **MOSER, E.**, MR microscopy of the human skin in vivo at 7 Tesla using an inductively coupled 6 mm multi-turn transmission line resonator. *In: Proceedings of the ESMRMB*, Antalya, Turkey, 2009 (poster)

LAISTLER, E. and **MOSER, E.**, Quantitative description of vessel geometry from microscopic MR skin imaging. *In: Proceedings of the ISMRM*, Montreal, Canada, 2011 (in review)